Search for heavy charged gauge bosons in the decay channel $\mathrm{W}' \to \mu\nu$ with CMS data

von

Sebastian Thüer

Masterarbeit in Physik

vorgelegt der
Fakultät für Mathematik, Informatik und Naturwissenschaften
der Rheinisch-Westfälischen Technischen Hochschule Aachen

im April 2012

angefertigt im

III. Physikalischen Institut A
Prof. Dr. Thomas Hebbeker

Zweitgutachter

Prof. Dr. Christopher Wiebusch

Zusammenfassung

Viele Erweiterungen des Standardmodells der Teilchenphysik beinhalten die Existenz neuer schwerer geladener Eichbosonen W′. Daher bietet die Suche nach diesen neuen Bosonen die Möglichkeit, verschiedene Theorien neuer Physik zu überprüfen.
In dieser Arbeit wird die Suche nach dem W′ im Zerfallskanal $W' \to \mu\nu$ mit Hilfe des gesamten 2011er Datensatzes des CMS Detektors mit einer integrierten Luminosität von $4.7\,\mathrm{fb}^{-1}$ bei einer Schwerpunktsenergie von 7 TeV durchgeführt. Eine gute Übereinstimmung zwischen der Standardmodell-Vorhersage und den aufgenommenen Daten ist beobachtbar, daher kann nur ein neues Ausschlusslimit auf ein potentielles W′ berechnet werden. Für ein W′ mit Kopplungen ähnlich denen des Standardmodells ergibt die Bayes'sche Limitberechnung ein Ausschlusslimit von $\mathrm{m_{W'}} < 2.4\,\mathrm{TeV}$ (95 % CL). Durch Kombination der Analyse mit der analogen Suche nach $W' \to e\nu$ kann die Ausschlussgrenze auf 2.5 TeV erweitert wird. Dies ist das zur Zeit beste Limit einer direkten Suche an einem Beschleunigerexperiment.
Außerdem wurde auch eine mögliche Interferenz zwischen dem Standardmodell W und dem W′ untersucht, dabei wurde sowohl der Fall von konstruktiver als auch von destruktiver Interferenz analysiert. Anschließend wird ein Ausschlusslimit für einen Signalwirkungsquerschnitt berechnet, welches erlaubt verschiedene theoretische Modelle zu überprüfen.

Abstract

Many extensions of the Standard Model of particle physics include the existence of new heavy charged gauge bosons W′. Therefore the search for these new bosons allows to probe several new physics models.
In this thesis the search for a W′ in the decay channel $W' \to \mu\nu$ is performed using the complete 2011 dataset of the CMS detector with an integrated luminosity of $4.7\,\mathrm{fb}^{-1}$ at a center of mass energy of 7 TeV. A good agreement between the expectation of the Standard Model and the data is observed, therefore only a new exclusion limit on a potential W′ can be derived. For a W′ with Standard-Model-like couplings the Bayesian limit calculation yields an exclusion of $\mathrm{m_{W'}} < 2.4\,\mathrm{TeV}$ (95 % CL). The analysis is then combined with the analogous search for $W' \to e\nu$ extending the exclusion range to 2.5 TeV. This is the currently best limit for a direct search at a collider experiment.
Also the effect of interference between the Standard Model W and the W′ is studied with the help of two models including destructive and constructive interference. Afterwards a model independent exclusion limit on a potential W′ signal cross section is produced, which helps to probe various kinds of models.

Contents

1. Standard Model of Particle Physics

In nature there are four known fundamental forces, the electromagnetic, the strong, the weak and the gravitational force. The Standard Model of Particle Physics (SM) is able to describe the particles and their interaction due to the first three out of this four fundamental forces. A combined description of the electromagnetic and the weak force is achieved by the Standard Model of electroweak interaction [1–3] and by also including the strong [4] force the Standard Model of Particle Physics is obtained.

1.1. Particles in the Standard Model

The matter content of the Standard Model is built of the leptons and quarks, which are fermions and therefore carry the spin $\frac{1}{2}$. For each of these particles there is also a corresponding anti-particle. The interaction between them can be described by the exchange of gauge bosons. For the electromagnetic interaction this is the massless photon, for the weak interaction there are the heavy $W^{\pm}$ and Z bosons and for the strong interaction there are eight massless gluons. All this exchange bosons are spin 1 particles and therefore bosons.

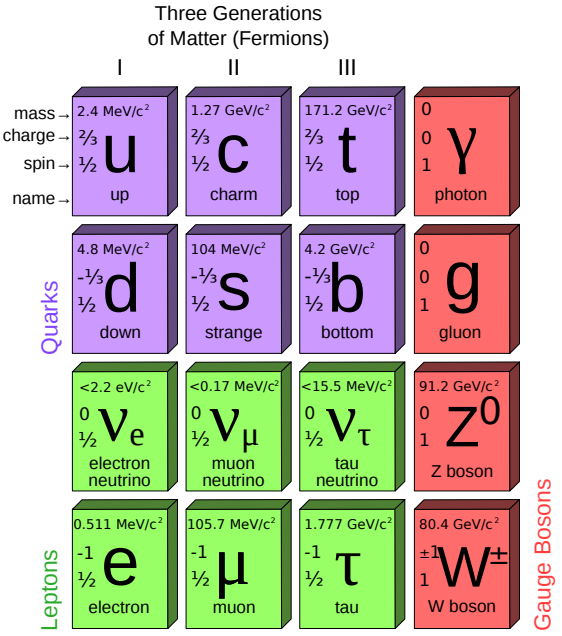

Figure 1.1.: Particle content of the Standard Model. From reference [5].

An overview over all the known particles and some of their properties in the SM can be seen in Figure 1.1. The leptons and quarks are divided into three different generations.

1.2. The Quantum Field Theory Formalism

A mathematical way to describe the Standard Model is achieved by using Quantum Field Theory and the underlying symmetry groups. The short introduction here is based on [6], [7] and [8]. The particles in the Standard Model are represented by fields ϕ_i. The particles and their interactions can be described by a Lagrange density or Lagrangian analogous to classical mechanics Lagrange formalism:

$$\mathscr{L} = \mathscr{L}(\phi_i, \partial_\mu \phi_i). \tag{1.1}$$

This Lagrangian is chosen in such a way that it describes the whole physics of the system by the use of the relativistic Euler-Lagrange equation. The relativistic Euler-Lagrange equation can be derived by maximizing the functional of the Lagrange density and is given by:

$$\frac{\partial \mathscr{L}}{\partial \phi_i} = \partial_\mu \frac{\partial \mathscr{L}}{\partial(\partial_\mu \phi_i)}. \tag{1.2}$$

For the simple case of a free spin $\frac{1}{2}$ particle the following Lagrangian satisfies the Euler-Lagrange equation:

$$\mathscr{L} = \bar{\psi}(i\gamma^\mu \partial_\mu - m)\psi, \tag{1.3}$$

with the spinor field ψ consisting of a spin and particle part, $\bar{\psi} = \psi^\dagger \gamma^0$, where $\psi^\dagger$ is the hermitian conjugate of the spinor ψ and the Dirac Matrices γ^μ. The free Dirac equation

$$(i\gamma^\mu \partial_\mu - m)\psi = 0. \tag{1.4}$$

can be obtained from this Lagrangian as Lagrange function. In the Standard Model interactions are introduced by demanding local gauge invariance. This will be shown for the simple example of Quantum Electrodynamics. The symmetry group needed for this is the U(1).

The Lagrangian has to be invariant under the global gauge transformation

$$\psi' = U\psi = e^{i\,q\,\phi}\psi. \tag{1.5}$$

The transformation U has to be hermitian to conserve the probability density $\bar{\psi}\psi$. ϕ and hence U are independent of the local space-time-coordinates x, therefore it is called a global gauge transformation. The parameter q indicates the coupling strength.

In the next step local gauge invariance is demanded which has to be fulfilled so that the Lagrangian is renormalizable [9]. A local transformation U(x) is achieved by making the ϕ in Equation 1.5 depending on the local space-time coordinates x. The partial derivative picks up an additional term under this transformation:

$$\partial_\mu \psi' = e^{i\,q\,\phi(x)}(\partial_\mu + i\,q\,\partial_\mu\,\phi(x))\psi. \tag{1.6}$$

which then flaws the invariance of the Lagrange density:

$$\mathscr{L}' = \bar{\psi}'(i\gamma^\mu \partial_m u - m)\psi' = \bar{\psi}(i\gamma^\mu \partial_m u - m)\psi + \psi\, i\, q\, \partial_\mu\, \phi(x)\psi \neq \mathscr{L}. \tag{1.7}$$

To restore the local gauge symmetry the partial derivative in the Lagrangian is replaced by the covariant derivate

$$D_\mu = \partial_\mu + iqA_\mu(x) \tag{1.8}$$

with the additional spin 1 vector field $A_\mu(x)$ which transforms as

$$A'_\mu(x) = A_\mu(x) - \frac{1}{q}\partial_\mu\phi(x). \tag{1.9}$$

In addition a kinematic term for the vector field has to be added to the Lagrangian, which is now invariant under local gauge transformations. It can be written as

$$\mathscr{L} = \bar{\psi}(i\gamma^\mu D_\mu - m)\psi - \frac{1}{4}F_{\mu\nu}(x)F^{\mu\nu}(x). \tag{1.10}$$

One part of this Lagrangian describes the interaction of the field ψ and the newly added vector field A_μ, which represents the photon. This interaction between the particles is introduced by demanding local gauge invariance. In this way the theory of Quantum Electrodynamics is constructed, which describes the electromagnetic interaction between all electrically charged particles.

1.2.1. Electroweak Theory

The electroweak theory unifies the weak and the electromagnetic interaction and was already formulated in the 1960s. The electromagnet force couples to all electric charged particles. The weak force distinguishes between left and right-handed particles and violates parity.
Every particle has a left and right-handed component. In order to get the different components, the left P_L and right P_R projection operators are useful:

$$P_L = \frac{1}{2}(1-\gamma^5) \qquad\qquad P_L = \frac{1}{2}(1+\gamma^5), \tag{1.11}$$

with $\gamma^5 = \gamma^0\gamma^1\gamma^2\gamma^3$.
The charged vector bosons $W^\pm$ only interact with left-handed particles or right-handed anti-particles. A mathematical way to describe this different behavior for left and right-handed particles is the weak isospin I. The symmetry group for the electroweak unification is the $SU(2)_L \times U(1)_Y$, the Y denotes the hypercharge. The left-handed particles form a doublet with isospin $\mathrm{I}_3 = \pm\frac{1}{2}$ under the $SU(2)_L$ while the right-handed particles form singlets. I_3 is the third component of the isospin relative to the quantization axis. The left-handed doublets of the fermionic part of the Standard Model are the following:

$$\begin{pmatrix} u \\ d' \end{pmatrix} \quad \begin{pmatrix} c \\ s' \end{pmatrix} \quad \begin{pmatrix} t \\ b' \end{pmatrix} \quad \begin{pmatrix} \nu_e \\ e \end{pmatrix} \quad \begin{pmatrix} \nu_\mu \\ \mu \end{pmatrix} \quad \begin{pmatrix} \nu_\tau \\ \tau \end{pmatrix}. \tag{1.12}$$

The upper row corresponds to $\mathrm{I}_3 = \frac{1}{2}$, the lower one to $\mathrm{I}_3 = -\frac{1}{2}$. The quarks in the lower row represent the flavor eigenstates and not the mass eigenstates, these states can be transformed into each other by use of the CKM matrix. Besides the quark mixing there is also a mixing of the neutrinos, but this will not be discussed here.
The right-handed singlets with isospin I=0 are:

$$u_R, d_R, c_R, s_R, t_R, b_R, e_R, \mu_R, \tau_R. \tag{1.13}$$

There is no right-handed neutrino singlet, so in case they do exist, they are not interacting by the weak interaction (or by any other interaction in the Standard Model). As

stated before the symmetry group for the unification is $SU(2)_L \times U(1)_Y$. The next step is to introduce the right covariant derivate for this group.

$$D_\mu = \partial_\mu + i\, g\, \vec{T} \cdot \vec{W}^\mu + \frac{g'}{2} Y B^\mu. \tag{1.14}$$

The $\vec{T}$ are the three generators of the $SU(2)_L$, one possible choice are the Pauli matrices, the different coupling strength of the fields $\vec{W}$ and B is described by the couplings g and g'. The $\vec{W}^\mu$ is a three dimensional vector of gauge fields

$$\vec{W}^\mu = \begin{pmatrix} W_1^\mu \\ W_2^\mu \\ W_3^\mu \end{pmatrix}. \tag{1.15}$$

For the $U(1)_Y$ the gauge field B^μ is introduced together with the hypercharge Y. The Gell-Mann-Nishijima relation between the electric charge Q, which is the source of the electromagnetic interaction, the weak isospin and the hypercharge Y is:

$$Q = I_3 + \frac{Y}{2}. \tag{1.16}$$

The gauge fields $\vec{W}^\mu$ are not the physical observable bosons, the observable charged bosons $W^\pm$ can be obtained by a linear combination:

$$W_\pm^\mu = \frac{1}{\sqrt{2}}(W_1^\mu \pm W_2^\mu). \tag{1.17}$$

The neutral bosons Z^μ and A^μ can be derived by a rotation:

$$A^\mu = B^\mu \cos\theta_W + W_3^\mu \sin\theta_W, \tag{1.18}$$

$$Z^\mu = -B^\mu \sin\theta_W + W_3^\mu \cos\theta_W. \tag{1.19}$$

The Weinberg angle θ_W is a free parameter in the Standard Model and can be expressed by the different couplings by:

$$\sin\theta_W = \frac{g'}{\sqrt{g^2 + g'^2}} \qquad \cos\theta_W = \frac{g}{\sqrt{g^2 + g'^2}}. \tag{1.20}$$

Also there there is a relation to the elementary electric charge e

$$e = g' \cos\theta_W = g \sin\theta_W. \tag{1.21}$$

The Lagrangian $\mathscr{L}_C$ for the charged current describing the exchange of the charged vector bosons $W^\pm$ is the following:

$$\mathscr{L}_C = -\frac{g}{2}[\bar{u}_i \gamma_\mu d_j'^L + \nu_i \gamma_\mu e_j^L] W_+^\mu + h.c. \tag{1.22}$$

Only the left-handed parts of the particles take place in the interaction. For the quarks the flavor-eigenstates d' take part in the interaction, they can be calculated with the CKM matrix.
The Lagrangian describing the neutral current $\mathscr{L}_{NC}$ is more complex because of the mixed vector and axial couplings.
There are basically four free parameters in the electroweak unification, one choice are the masses of the bosons m_W and m_Z and the two couplings g and g', but there are other possibilities, e.g. replacing one of the aforementioned parameters by the Weinberg angle. So far the masses of the particles were not discussed, but they will be introduced later by spontaneous symmetry breaking and the introduction of the Higgs boson.

1.2.2. Quantum Chromodynamics - QCD

Quantum Chromodynamics is the theory of the strong interaction of quarks by the exchange of massless gluons. Leptons are not participating in the strong interaction. In the QCD another quantum number is introduced, the color charge. It is independent of the other quantum numbers and only gluons and quarks carry it.
The strong interaction can be described by a SU(3) with 8 generators which represent the 8 different gluons. One choice for the generators are the Gell-Mann matrices λ_i which do not commutate, the SU(3) is a non-abelian group.
Quarks can form colorless baryons and mesons. A meson consists of a colored quark and an anti-quark with the corresponding anti-color of the quark, a baryon consists of three quarks or anti-quarks with different colors.
A consequence of the gluon carrying the color charge itself is that the gluons are self-interacting. The strong coupling constant α_s increases with the distance between two colored particles, leading the quarks to not being able to exist freely, this is called confinement.

1.2.3. Spontaneous Symmetry Breaking

All of the previous considerations are only valid for massless particles, but from experiments it is known that the particles do have masses. Including boson mass terms of the from $mA_\mu A^\mu$ into the Lagrange density is not allowed because they spoil the principle of gauge invariance. Nevertheless there is a way to introduce boson masses by the Higgs mechanism and later on by introducing Yukawa couplings also masses to the fermions.
In the Higgs mechanism the doublet Φ under a SU(2) consisting of two complex fields ϕ^+ and ϕ^0 is introduced:

$$\Phi = \begin{pmatrix} \phi^+ \\ \phi^0 \end{pmatrix} = \frac{1}{\sqrt{2}} \begin{pmatrix} \phi_1 + i\phi_2 \\ \phi_3 + i\phi_4 \end{pmatrix}. \tag{1.23}$$

The corresponding Lagrangian consists of a kinematic part and the Higgs potential $V(\Phi) = -\mu^2\Phi^\dagger\Phi + \lambda(\Phi^\dagger\Phi)^2$:

$$\mathscr{L} = (D_\mu\Phi)^\dagger(D^\mu\Phi) - V(\Phi) = (D_\mu\Phi)^\dagger(D^\mu\Phi) + \mu^2\Phi^\dagger\Phi - \lambda(\Phi^\dagger\Phi)^2. \tag{1.24}$$

For $\mu^2 > 0$ the symmetry is spontaneously broken and the Higgs potential becomes the mexican hat potential as shown in Figure 1.2. For this choice of the parameters the minimum is not located at 0, but at

$$\Phi^\dagger\Phi = -\frac{\mu^2}{\lambda}. \tag{1.25}$$

The vacuum expectation value of one of the components of Φ is now set to 0 while the other is different from zero, e.g

$$< 0|\Phi|0 >= \frac{1}{\sqrt{2}} \begin{pmatrix} 0 \\ v \end{pmatrix}. \tag{1.26}$$

This leads to $v_0 = \sqrt{-\frac{\mu^2}{\lambda}}$. Expanding the field Φ around its vacuum expectation value

$$\Phi = \frac{1}{\sqrt{2}} \begin{pmatrix} 0 \\ v + h(x) \end{pmatrix} \tag{1.27}$$

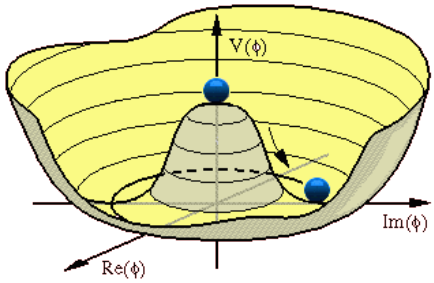

Figure 1.2.: Shape of the Higgs potential for $\mu^2 > 0$, the minimum not being located at 0 leads to a spontaneous broken symmetry. Taken from reference [10].

leads to additional terms in the Lagrangian

$$\Delta\mathscr{L} = \frac{1}{2}(\partial_\mu h)(\partial^\mu h) - \mu^2 h^2. \tag{1.28}$$

The kinematic parts in the Lagrangian in Equation 1.24 produce the mass terms for the different bosons. They are $M_W = \frac{gv_0}{2}$ and $M_Z = \frac{M_W}{\cos\theta_W}$. The last part of the additional terms in Equation 1.28 represents the Higgs boson with its mass $m_h = \sqrt{2}\,\mu$.
Given this Higgs field it is also possible to give the fermions their mass by introducing Yukawa couplings. This mechanism is decoupled to the symmetry breaking before, it could be that both are realized in nature, only one or neither of them. The Yukawa couplings have the form

$$\mathscr{L}_{Yukawa} = G\bar{\psi}\Phi\psi \tag{1.29}$$

with G describing the coupling of each fermion to the Higgs field, it is proportional to the fermion's mass.

1.3. Open Questions of the Standard Model

Besides the Standard Model's outstanding achievement to describe the experimental observables at very high accuracy there are some shortcomings with it, some will be briefly described here.
The Standard Model can be described by three gauge groups each with its unique couplings. These couplings change with the energy at which the interaction takes place, the Grand Unified Theory is a theory which tries to unify the different couplings at a certain scale. In the Standard Model it is not possible to unify these three couplings.
The Standard Model describes the three different forces described before quite accurately, but it cannot describe the forth force, gravitation, at all. Another open question is why gravitation is so much weaker than the electromagnetic interaction, in the hydrogen atom the electromagnetic force is about 10^{37} times stronger than the gravitational force.
Also the masses of the different particles seem to be arbitrary, there are huge mass gaps between the different quarks and leptons. The heaviest known particle, the top quark, has a mass of about 172 GeV [11] and the lighter quarks only have a mass of about a few MeV. This is even more drastic for the leptons, where the tau lepton has a mass of 1.78 GeV and the lightest leptons, the neutrinos, only have masses of the order of eV or even less. The origin of these gaps between the particles' masses is unknown.

There are loop corrections that contribute to the Higgs mass, which add a quadratic divergent term in the large cut-off parameter Λ. The cut-off parameter Λ describes the energy scale up to which the Standard Model is believed to be valid. To keep the Higgs mass small some fine-tuned factors have to be applied to this quadratic terms. This is called the fine-tuning problem.
From neutrino oscillations it is known that neutrinos do have mass. In order to give particles a mass there has to be a connection between the left and right-handed parts by the Yukawa couplings, but there is no right-handed neutrino in the Standard Model, therefore the neutrinos are massless.
The weak interaction only couples to left-handed particles, the nature of this parity violating couplings is not known.
There are a lot of theories dealing with these problems by adding new forces and particles and implying new symmetries. Here the focus will be only on additional heavy charged gauge bosons, the W′s, which are spin 1 particles and carry the electric charge of ± 1.

1.4. Heavy Charged Gauge Bosons

By introducing one possible extension to the Standard Model symmetry groups a left-right symmetry at higher scales is achieved, assuming that this symmetry is broken for lower energies and thus leading to the only left-handed coupling of the weak force [12].
The simplest way to extend the symmetry groups and achieving left-right symmetry is by adding another SU(2) group which only couples to right-handed fermions. Neglecting the color sector of the Standard Model the gauge groups at high energy would be:

$$SU(2)_L \times SU(2)_R \times U(1). \tag{1.30}$$

The Standard Model right-handed singlets under $SU(2)_L$ then become doublets under the $SU(2)_R$ and the doublets under the $SU(2)_L$ become singlets under $SU(2)_R$. At high energies left and right-handed components take part in the weak interaction.
Together with the new gauge group an additional weak isospin is introduced, to distinguish between them they are called $I_{3,L}$ and $I_{3,R}$. The Gell-Mann-Nishima relation can now be modified taking into account the new quantum numbers:

$$Q = I_{3,L} + I_{3,R} + \frac{B-L}{2}, \tag{1.31}$$

where besides the weak isospin also the modified hypercharge $\tilde{Y}$ enters. It is similar to the hypercharge of the U(1) in the Standard Model but is it defined here as the difference of baryon minus lepton number $\tilde{Y} = B - L$. For leptons this hypercharge is $\tilde{Y} = -1$ and for quarks $\tilde{Y} = 1/3$.
The resulting fermionic part of the Lagrangian is again fixed by the principle of gauge invariance. It is symmetric under the exchange of $\mathrm{R} \leftrightarrow \mathrm{L}$ and therefore parity conserving. It can be divided into a left and a right-handed part:

$$\mathscr{L} = i\bar{\psi}_L \gamma_\mu D_L^\mu \psi_L + i\bar{\psi}_R \gamma_\mu D_R^\mu \psi_R. \tag{1.32}$$

The left and right covariant derivatives are defined using the new gauge fields $\vec{W}_R^\mu$, $\vec{W}_L^\mu$ and B^μ:

$$D_L^\mu = i\frac{g_L}{2}\vec{W}_L^\mu \cdot \vec{T}_L + ig'\frac{B-L}{2}B^\mu \tag{1.33}$$

$$D_R^\mu = i\frac{g_R}{2}\vec{W}_R^\mu \cdot \vec{T}_R + ig'\frac{B-L}{2}B^\mu. \tag{1.34}$$

In order to break the symmetry to get back to the left-right symmetry breaking electroweak force a Higgs mechanism is needed in a modified form.
The Higgs mechanism needs to break the new gauge group down to the observable electroweak unification and give the particles their mass as it is done in the Standard Model. There are several ways to do this, here only the minimal-LR case will be discussed with three scalar multiplets Δ_L, Δ_R and Φ [13].
This multiplets can be written in a matrix form:

$$\Delta_{L/R} = \begin{pmatrix} \Delta_{L/R}^{11} & \Delta_{L/R}^{12} \\ \Delta_{L/R}^{21} & \Delta_{L/R}^{22} \end{pmatrix} \qquad \Phi = \begin{pmatrix} \phi_{11} & \phi_{12} \\ \phi_{21} & \phi_{22} \end{pmatrix}. \tag{1.35}$$

As a next step the vacuum expectation values for the three field are defined as:

$$\Delta_{L/R,0} = \begin{pmatrix} 0 & 0 \\ v_{L/R} & 0 \end{pmatrix} \qquad \Phi = \begin{pmatrix} v & 0 \\ 0 & w \end{pmatrix}. \tag{1.36}$$

This results in additional Higgs particles, some electrically charged and one even doubly charged. In this way the symmetry group is broken in two ways

$$SU(2)_L \times SU(2)_R \times U(1) \to SU(2)_L \times U(1) \to U(1)_{em}. \tag{1.37}$$

For the first step the vacuum expectation value v_R of the Δ_R boson is the important parameter, the second step is done by the Φ multiplet. In order to match the observable masses v_R has to be large because a left-right symmetry has not been observed at the energies reached so far. Also v_L has to be small in order to keep the small mass difference between the Standard Model gauge bosons. Therefore the relation:

$$|v_R|^2 \gg |v|^2 + |w|^2 \gg |v_L|^2 \tag{1.38}$$

is needed. Analogous to the Standard Model these W_L and W_R are not the observable bosons. The corresponding charged bosons would be the already know Standard Model W and a potential new W$'$ which are linear combinations of the W_L and W_R. For equal couplings g of the left and right part the resulting masses for the observable bosons are

$$m_W = \frac{g^2}{2}(v^2 + w^2 + 2v_L^2) \tag{1.39}$$

$$m_{W'} = \frac{g^2}{2}(v^2 + w^2 + 2v_R^2). \tag{1.40}$$

Since the second of this charged bosons has not been observed, the vacuum expectation value v_R has to be large.
The left-right symmetric model also allows for right-handed neutrinos in the standard model which then can be assigned a mass due to the Yukawa couplings. An additional mechanism, the see-saw mechanism [14], is needed in order to keep the Standard Model

neutrino masses small.
In case of light right-handed neutrinos the Reference Model, see next section, can be obtained. Heavy, non-stable right-handed neutrinos allow for different searches, e.g. [15].
Besides the left-right symmetric model, there are a lot of other theories that implement a new heavy charged gauge boson:

- Little Higgs: The SM Higgs Boson becomes a pseudo-Goldstone of an approximate global symmetry, which protects the Higgs mass from quadratically divergent corrections [16].
- GUT-Theories: Theories that unify the different forces by introducing a higher symmetry group, for example the SU(10) or the E6.
- Extra Dimensions: In the Kaluza-Klein theory [17] additional spatial dimensions are introduced to also describe gravitation in the quantum field formalism. Additional gauge bosons can then be interpreted as excitation states of the SM gauge bosons, one example is given later on in Section 1.4.3.

1.4.1. Reference Model

A more simplified approach and a guideline for the experimental search of heavy gauge bosons W′ at hadron colliders is made by the Reference Model [18] at the end of the 1980s. It describes the ad hoc implementation of new heavy charged gauge bosons which couple to the Standard Model leptons like the W boson, making the new bosons carbon copies of the Standard Model bosons with higher masses. It is a generalization of the left-right symmetric model with light right-handed neutrinos. The Reference Model has only one additional parameter, the mass of the W′. Besides the coupling to fermions also the coupling to massive Standard Model bosons is possible and strongly increasing with the W′ mass. At CMS also the search for $W' \to WZ$ is performed, see [19, 20]. This additional coupling to the SM bosons increases the width of the W′, for masses above 500 GeV the width gets bigger than the mass itself.
In order to keep this width small a suppression factor to the coupling to Standard Model bosons can be introduced:

$$\xi = (\frac{m_W}{m_{W'}})^2. \tag{1.41}$$

A similar suppression factor is naturally obtained if the SM W and the W′ are part of different gauge groups and the interaction is only possible by the symmetry breaking.
The Reference Model [18] allows to calculate the W′ width, branching ratios and the cross section as a function of the W′ mass.

1.4.2. Model used for the Leptonic Searches

A slight variation from the Reference Model is made for the searches of the fermionic decay $W' \to \ell\nu$ at hadron colliders. This model is implemented in the event generator Pythia [21], in the following it is called the Pythia Model. It is based on the Reference Model with two additional assumptions:

- The W′ does not couple to Standard Model bosons, therefore the decay $W' \to WZ$ is forbidden.

- There is no interference between the SM W and the new W′. If the W′ couples to left-handed fermions, then there should be interference between the SM W and the W′. So this model only allows for right-handed couplings of the W′.

This leads to the following possible decay channels of a W':

$$e + \nu_e \quad \mu + \nu_\mu \quad \tau + \nu_\tau \quad u + d' \quad c + s' \quad t + b'. \tag{1.42}$$

These are the same decay channels as for the Standard Model W with the exception of the $t + b'$, which is kinematically not allowed due to the high mass of the top quark. At sufficient high masses of the W′ the branching ratios get constant with about 8 % for each leptonic decay.
The width can then be computed by neglecting all the fermion masses except the ones from top and bottom by [22]

$$\Gamma_{\mathrm{W}'} = m_{\mathrm{W}'} \frac{g^2}{2} \frac{1}{48\pi} (18 + 3F(\frac{m_t}{m_{\mathrm{W}'}}, \frac{m_b}{m_{\mathrm{W}'}})) \tag{1.43}$$

$$\text{with} \quad F(x,y) = (2 - x^2 - y^2 - (x^2 - y^2)^2)\sqrt{(1-(x+y)^2)(1-(x-y)^2)}. \tag{1.44}$$

Note that F(0,0) = 2 leads to a linear dependence of the W′ width with its mass at sufficient high masses.
This model is the one that is implemented in Pythia [21] and was used for the leptonic searches at the Tevatron and LHC experiments so far.

1.4.3. Universal Extra Dimensions

There are also different models with extra dimensions, which predict additional vector bosons. Here only one model will be presented in a very brief way, which predicts a W′ with Standard-Model-like couplings, so that the limits derived with the Pythia Model can be reinterpreted in terms of this model.
The Universal Extra Dimensions model [23] is based on a five-dimensional space-time including an extra spatial dimension besides the four space-time components that are observable. The fifth dimension is compact meaning its range is limited to

$$x \in [-L, L] = [-\pi R, \pi R]. \tag{1.45}$$

All Standard Model particles have their Kaluza-Klein states, the interesting one here is the W_n; the n denotes the n-th Kaluza-Klein excitation state. The model parameters of the UED model are the size of the compact dimension R and the Dirac type mass term μ in five dimensions.
For the coupling and the mass of this W_n the following relations apply [23, 24]:

$$m_{W_n}^2 \equiv m_n^2 = m_W^2 + \left(\frac{n}{R}\right)^2. \tag{1.46}$$

$$g_n = g^{\mathrm{SM}} \mathcal{F}_n(\pi\mu R), \tag{1.47}$$

$$\mathcal{F}_n(x) = \begin{cases} 0 & \text{if } n = 2m+1 \\ \frac{x^2(-1+(-1)^m e^{2x})(\coth x - 1)}{\sqrt{2(1+\delta_{m0})(x^2 + m^2\pi^2/4)}} & \text{if } n = 2m. \end{cases} \tag{1.48}$$

where m is an integer. Odd modes do not couple to Standard Model particles because of Kaluza-Klein parity conservation, therefore only the even modes are interesting. For higher modes $n \geq 4$ there is vanishing sensitivity at current center of mass energies, therefore the most interesting mode is the $n = 2$ mode.
The W_2 or W'_{KK} is kinematically identical with the Standard-Model-like W$'$ of the Pythia Model , therefore the limits that are obtained with help of the Pythia Model in the channels W$' \to \ell\nu$ can be translated into exclusion regions in the UED parameter space. This is done in the CMS analysis note AN-11-471 [24].

1.4.4. Interference

A general way to write the Lagrangian describing the W$'$ coupling to fermions is given by [11]:

$$\mathscr{L}_{\mathrm{W}'} = \frac{W'^{\mu}}{\sqrt{2}}[\bar{u}_i(C^R_{qij}P_R + C^L_{qij}P_L)\gamma^{\mu}d_j + \bar{\nu}_i(C^R_{lij}P_R + C^L_{lij}P_L)\gamma^{\mu}e_j] + h.c. \quad . \tag{1.49}$$

containing both left- and right-handed couplings which are denoted by the L and R indices. These couplings C can be different for quarks (C_q) and leptons (C_l) and even differ for the various generations denoted by the indices i and j. If the left-handed couplings are different from 0 then there is interference between the W and the W$'$.
The Standard Model W boson can be also described by the Lagrangian in Equation 1.49 with the coupling constants for all generations $C^L_l = C^L_q = g$ and $C^R_q = C^R_l = 0$, when the CKM matrix coefficients arising from the quark mixing are put outside the couplings. For example the process

$$u + \bar{d} \to l + \nu \tag{1.50}$$

can either be achieved by the exchange of a SM W boson or by the exchange of a W$'$. The matrix element describing the exchange of a SM W boson is proportional to the corresponding propagator; neglecting the width of the boson the important dependencies of the matrix element can be written as:

$$M_W \propto g^2 \cdot V_{CKM} \cdot \frac{1}{q^2 - m^2_W}, \tag{1.51}$$

with the momentum transfer q. The matrix element for the exchange of a W$'$ with a left-handed quark and a left-handed fermion vertex is proportional to:

$$M_{W'} \propto C^L_q \cdot C^L_l \cdot \frac{1}{q^2 - m^2_{W'}}. \tag{1.52}$$

The matrix element describing the process $u+\bar{d} \to l+\nu$ has to take both matrix elements into account. The cross section depends on the square of the absolute value of the matrix element $\sigma \propto |\mathcal{M}|^2$, it can be written as:

$$|\mathcal{M}|^2 = |\mathcal{M}_W + \mathcal{M}_{W'}|^2 = |\mathcal{M}_W|^2 + |\mathcal{M}_{W'}|^2 + 2Re(\mathcal{M}^*_W\mathcal{M}_{W'}). \tag{1.53}$$

The last term in the equation is the interference term. Neglecting the width of the two bosons the important dependencies can be written as:

$$\mathcal{M}^*_W\mathcal{M}_{W'} \propto g^2 \cdot V_{CKM} \cdot C^L_q \cdot C^L_l \cdot \frac{1}{q^2 - m^2_W} \cdot \frac{1}{q^2 - m^2_{W'}}. \tag{1.54}$$

The interference term and therefore also the signal cross section depend on the left-handed couplings of the W′ and on the momentum transfer q, which corresponds to the center-of-mass energy in the s-channel production. For $m_W^2 < q^2 < m_{W'}^2$ the there is a sign flip in the interference term. Besides the change in the signal cross section also the kinematic distributions change due to the interference effects [25, 26] and therefore this interference affects the whole analysis. In Section 8 the impact on the analysis is shown for three different choices of the couplings C. Afterwards cross section limits are derived, which are independent of the chosen W′ couplings and allow to probe various models.
In the left-right symmetric model the W′ only couples to right-handed fermions, while the SM W only couples to left-handed particles, therefore there is no interference between them in this model. In the Reference Model both couplings are allowed, so in general there could be interference which is neglected in the Pythia implementation.

Current Limits

There are both direct and indirect limits for the search of heavy, charged gauge bosons. The best direct limits are achieved by collider experiments like the ones at the LHC. Before the start of the LHC the Tevatron was holding the most stringent limits on a W′ with Standard-Model-like couplings. The DØ experiment published their results in the search channel $W' \to e\nu$ with an integrated luminosity of $1\,\mathrm{fb}^{-1}$ and excludes a W′ with masses below 1 TeV [27]. Recently the CDF Collaboration published their latest result in the same channel with a larger integrated luminosity of $5.3\,\mathrm{fb}^{-1}$ and they exclude a W′ with $\mathrm{m}'_{\mathrm{W}} < 1.12\,\mathrm{TeV}$ [28] which corresponds to a limit on $\sigma \cdot \mathrm{BR}(\mathrm{W}' \to \mathrm{e}\nu)$ of about 10 fb. Even after the short running time the LHC has produced more stringent limits on the production of a Standard-Model-like W′ due to the higher center-of-mass energy. Besides the direct searches there are also indirect limits that can be made under certain assumptions from different observations, a nice summary can be found in the Review of Particle Physics [11] by the Particle Data Group. For example, if the W′ has a coupling to right-handed quarks like in the left-right symmetric case, it has a severe impact on the $K_L - K_s$ mixing, leading to a mass limit of $m_{\mathrm{W}'} > 2.5\,\mathrm{TeV}$ [29].

1.5. Conventions

Throughout this analysis several conventions are used which will be explained here. The common natural units of particle physics are used, $\hbar = \mathrm{c} = 1$. This leads to the same units for mass, momentum and energy of a particle:

$$[\text{mass}] = [\text{momentum}] = [\text{energy}] = \text{GeV}. \tag{1.55}$$

The invariant mass of a system is given by the energy-momentum relation:

$$p^2 = p_\mu p^\mu = E^2 - |\vec{p}|^2 = m^2 \tag{1.56}$$

in the four dimensional coordinate system $p^\mu = (E, \vec{p})$. It is a conserved quantity, which is particular interesting in collider experiments, because it is the energy which can be used to produce new particles, for a single particle the invariant mass is equal to its rest

mass.
A spherical coordinate system is used in this analysis with the azimuthal angle ϕ and the polar angle θ. In collider physics it is common to use the pseudorapidity instead of the polar angle, it is defined as:

$$\eta = -\ln(\tan\frac{\theta}{2}). \tag{1.57}$$

Also often the transverse component of some variable is used, for example the transverse momentum $\mathrm{p_T}$, it is defined as the following:

$$p_T = \sqrt{p_x^2 + p_y^2}, \tag{1.58}$$

where p_x and p_y are the components of the momentum in the transverse plane.

2. LHC and CMS

2.1. The Large Hadron Collider

The Large Hadron Collider LHC [30] is the world's largest particle collider, located at the CERN complex close to Geneva. It is designed to accelerate and collide protons and ions. The design energy for proton beams is 7 TeV resulting in a center of mass energy of 14 TeV, for lead ions the beam energy is 2.76 TeV per nucleon. The design luminosity for proton collisions is $10^{34}\,\mathrm{cm}^{-2}\mathrm{s}^{-1}$ and $10^{27}\,\mathrm{cm}^{-2}\mathrm{s}^{-1}$ for lead-ion collisions. It is built in the 26.7 km long tunnel of the former electron-positron collider LEP accelerator.
Since the beginning of 2010 the LHC is running with a center-of-mass energy of 7 TeV. The instantaneous luminosity $\mathcal{L}$ per experiment for a collider with two beams with n_B bunches per beam, where each bunch of the first beam consists of N_1 protons and each bunch of beam two of N_2 protons, can be calculated by the formula:

$$\mathcal{L} = f \cdot \frac{n_B N_1 N_2}{A_{eff}} \tag{2.1}$$

where f denotes the revolution frequency and A_{eff} the effective overlap area of the beams. So far the LHC reached a bunch-spacing of 50 ns, which corresponds to a collision frequency of 20 MHz, and operated with up to 1330 bunches, each of them consisting of about $1.4 \cdot 10^{11}$ protons.
A very convenient way to state the integrated luminosity is to use inverse barns as unit. Usually barns are used for measuring cross sections, one barn is defined as: 1 b = $10^{-24}\,\mathrm{cm}^{-2}$. In 2011 the LHC has delivered about $5\,\mathrm{fb}^{-1}$ of data to the experiments.
The radiation losses due to synchrotron radiation depend on $\frac{1}{\mathrm{R}}\frac{\mathrm{E}^4}{\mathrm{m}^4}$, at design parameters this accounts for 3.6 kW of energy loss. This is the reason why only hadron machines can achieve these high energies, an electron collider with the same radius would loose $(\frac{\mathrm{m_{proton}}}{\mathrm{m_{electron}}})^4$ times more energy, which is not practicable. The LHC is only the last, but by far the largest, accelerator in a complex accelerator chain. CERN with all its accelerators is shown in Figure 2.1. The beam starts at a small bottle of hydrogen, the hydrogen gets ionized and the resulting protons get accelerated in the first accelerator LINAC2 up to 50 MeV. Afterwards the protons are send to the first circular accelerator, the Proton Synchrotron Booser (PSB), which accelerates them up to 1.4 GeV and sends them to the Proton Synchrotron (PS), where they get accelerated up to 25 GeV. The last pre-accelerator is the Super Proton Synchrotron (SPS), which accelerates the protons up to 450 GeV, at this energy they are injected into the LHC and reach their final energy.
The LHC is divided in 8 bent arcs and 8 straight sections, on four of the straight sections there are the interaction points at which both beams of the LHC collide. At the different interaction points the four big experiments are located. There are the two big multi-purpose detectors CMS [32] and ATLAS [33], which will need the full luminosity. Besides that there are also the ALICE [34] detector aiming for heavy-ion physics and LHCb [35], which focuses on CP violation in B-physics, they are arranged around the ring in the different interaction points, see Figure 2.1.

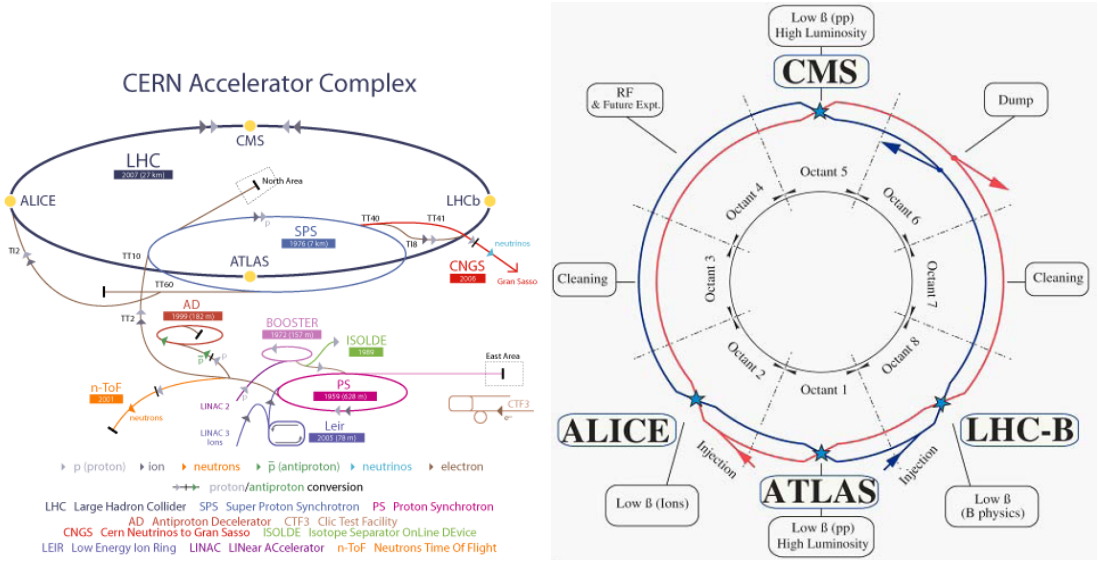

Figure 2.1.: Schematic view of the pre-accelerator chain and the CERN complex (left), From reference: [31]. On the right an overview of the different experiments at the LHC is given. From reference [30].

In order to keep the beams on their orbit 1232 superconducting dipole magnets are placed in the arc sections of the LHC. Each of them has to have a maximum magnetic field of about 8.4 T for the maximal beam energy of 7 TeV. Because of the Lorentz force both beams of the LHC cannot share the same beampipe, each of them needs a different direction of the magnetic field to be kept on the circular orbit. Therefore a special concept for the dipole magnets was developed producing both direction with one magnet, see Figure 2.2.
The cooling system and the mechanical structure are the same for both beampipes but due to the arrangement of the superconducting coils two homogeneous fields with inverse polarities are produced in the two beampipes. Each of the magnets is 15 m long and cooled by superfluid helium down to 1.9 K. In this way it is possible to achieve currents of 11.7 kA, which produce the required, very strong magnetic field of 8.4 T. The limiting factors for the energy of the beams are the fixed radius of the tunnel and the magnetic field of the dipoles.

2.2. The CMS - Experiment

The Compact-Muon-Solenoid (CMS) [32] is one of the two multi-purpose detectors operating at the LHC. The main aims of the detector are to be able to detect a potential Higgs boson as well as to detect new physics phenomena at the TeV-scale.
The CMS detector is 21.6 m long and has a diameter of 14.6 m with an overall weight of about 14000 tons. To be able to detect the different particles produced in a collision the apparatus consists of several different detector types.
A schematic view of the whole detector with the sub-detectors is shown in Figure 2.3. From the inside out the different sub-detectors are the silicon pixel vertex detector, the

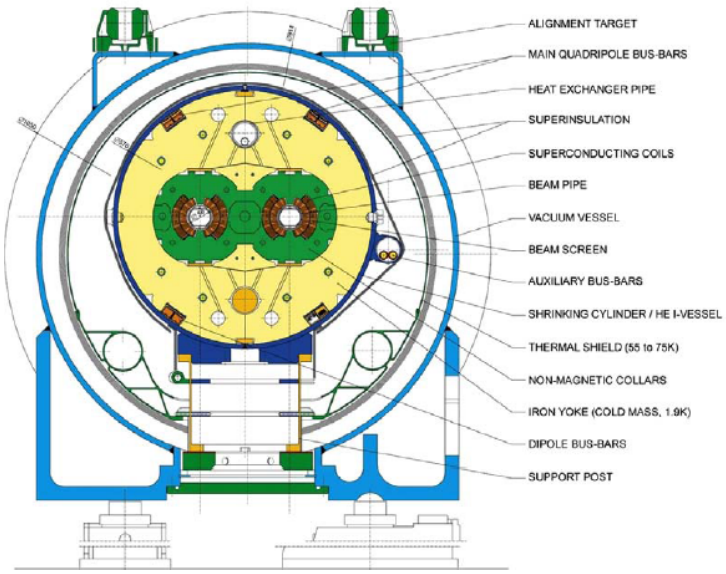

Figure 2.2.: Schematic view of the dipole magnets with their special design to host both beampipes with opposite polarities. From reference [30].

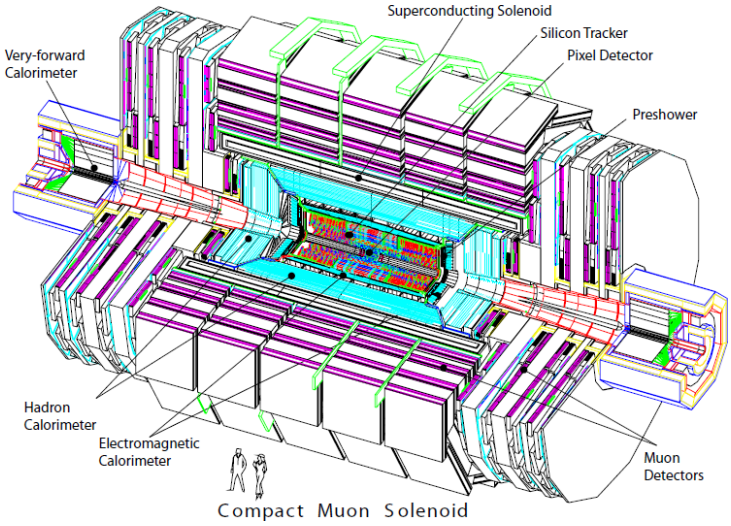

Figure 2.3.: Schematic view of the CMS experiments with its different subsystems. From reference [32].

silicon strip tracker, the electromagnetic calorimeter, the hadronic calorimeter, the coil of the solenoid and the iron return yoke with the muon system.
The tracker and the calorimeters are inside the solenoid with a homogeneous magnetic field of about 3.8 T, in the iron return yoke the magnetic field is about 2 T. The solenoid has a diameter of 6 m and a length of 12.5 m, at full magnetic field the total energy stored accounts for about 2.6 GJ, the highest value ever achieved by a single magnet. To get to this high fields the superconducting solenoid operates at currents of 19.1 kA and is cooled by 220 tons of helium to 4.45 K.
The iron accounts for most of the weight of the detector but also for the mechanical stability. As seen in Figure 2.3, the detector is divided into 5 wheels in the central part, the so-called barrel, and two additional disc-like endcaps.
The different detector parts will now be described briefly.

2.2.1. The Tracking System

The following short overview is based on [36]. The main reasons why CMS chose to make an all silicon tracker were: The tracker has to have a high spatial resolution to reconstruct secondary vertices, it has to be fast to deal with the 25 ns bunch crossing, it has to have a high granularity to deal with the high amount of tracks generated at proton-proton collisions and it has to withstand the high radiation damage produced by the high event rate. All this can be achieved with silicon detectors.
The all silicon tracking system inside the strong solenoid field consists of a silicon vertex detector with 1440 pixel modules and a silicon strip detector with 15148 strip detector sensors. Both parts combined have a length of 5.8 m and a diameter of 2.5 m covering a geometrical acceptance up to $|\eta| < 2.5|$ with η being the pseudorapidity. In order to reduce the damage from hard radiation and to reduce leak currents the tracker is cooled down to $-10°$ C. The high amount of silicon can cause multiple scattering, bremsstrahlung and photon conversion, this has to be accounted for at the reconstruction stage.
The design of the tracker system can be seen in Figure 2.4.

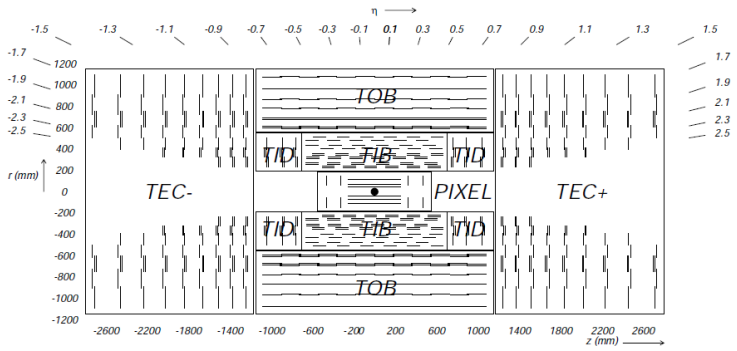

Figure 2.4.: The tracker system of CMS with the silicon pixel and the silicon strip detector. From reference [32].

Silicon Pixel Tracker

The pixel detector is the innermost part of the detector, it is needed for the reconstruction of the tracks of primary produced particles in the collision as well as for the reconstruction

of secondary vertices due to very short lived particles, like τ-leptons or b-hadrons.
The pixel detector surrounds the beam pipe in the barrel in 3 layers with radii of 4.4, 7.3 and 10.2 cm and additional side discs with two layers on the endcaps. It consists of about 66 million pixels build on 1440 pixel modules to cover an area about $1\,\mathrm{m}^2$. Each pixel has the size of $150\,\mu\mathrm{m} \times 100\,\mu\mathrm{m}$ and due to the possible three dimensional reconstruction the vertices can be reconstructed with a resolution of about $\sim 10\,\mu\mathrm{m}$.

Silicon Strip Tracker

Outside of the pixel tracker the silicon strip tracker covers the radial region between 20 cm and 116 cm with a total of about $200\,\mathrm{m}^2$ active area. It is divided further into several subsystems, see Figure 2.4.
The innermost part consists of the Tracker Inner Barrel (TIB) and the Tracker Inner Disks (TID), both parts extend up to a radius of 55 cm. The TIB consists of four layers parallel to the beampipe, while the TID only consists of three layers. The Tracker Outer Barrel (TOB) and the Tracker End Caps (TEC) cover the radial range between 55 cm and 116 cm and are made of 6 and 9 layers, respectively.
The modules allow to measure the r-ϕ coordinate; some of the layers are made of double sided modules, which allows to also measure the z coordinate. In the barrel region the size of the strips increases with increasing distance to the beampipe from $10\,\mathrm{cm} \times 80\,\mu\mathrm{m}$ to $25\,\mathrm{cm} \times 180\,\mu\mathrm{m}$, the spatial resolution changes from $20\,\mu\mathrm{m}$ to $40\,\mu\mathrm{m}$.
For high energy tracks the transverse momentum resolution in the barrel part is about 1-2 % [32].

2.2.2. The Calorimeters

Outside of both the tracking detectors, but still in the magnetic field of the solenoid, two kinds of calorimeters are located, the electromagnetic and the hadronic calorimeter.

The Electromagnetic Calorimeter - ECAL

In the Electromagnetic Calorimeter (ECAL) [37] the particles interact electromagnetically until they are absorbed while producing photons by scintillation. By detecting the produced photons the energy of the original particle can be determined.
The purpose of the ECAL is to measure electron and photons, but also the electromagnetic part of jets with a good energy resolution. Due to the constraints by the compact design of the CMS detector lead tungstate ($PbWO_4$) crystals were chosen as detector material. It can act as both absorber and scintillator making the ECAL a homogeneous calorimeter. Lead tungstate is a fast inorganic scintillator and has a very high density of $8.28\,\mathrm{g/cm}^3$, a short radiation lenght of 0.89 cm and a small Molière radius of 2.2 cm. Each of the crystals has a length of 23 cm which corresponds to about 26 radiation length.
The ECAL consists of 61200 crystals in the barrel and 7324 in each of the endcap; the design can be seen in Figure 2.5. In the barrel region up to pseudorapidities of $|\eta| < 1.479$ each crystal is equipped with an avalanche photodiode (APD) for the photon detection. APDs were chosen because of the low light output of lead tungstate of about 30 photons per MeV of an electron and because they are insensitive to the high magnetic field. The photon quantum efficiency of the APDs is about 75 % at the maximum of the scintillation light spectrum of 430 nm.

The ECAL endcaps cover the region from $1.479 < |\eta| < 3.0$ and for the photon detection vacuum phototriodes (VPT) were chosen because of the higher particle fluxes in this region.
In Figure 2.5 there is also another detector located in the endcaps, the Preshower (ES), it covers the range $1.653 < |\eta| < 2.6$. Its purpose is to improve the detection of $\pi \to \gamma\gamma$, which can get misreconstructed as a single high-energetic photon. The Preshower is a sampling calorimeter consisting of two layers of lead radiator and silicon strips to measure the energy and the shower shape.
The energy resolution can be separated into three terms, statistical, noise and constant [32]:

$$(\frac{\Delta E}{E})^2 = (\frac{2.8\,\%}{\sqrt{E/GeV}})^2 \oplus (\frac{12\,\%}{E/GeV})^2 \oplus (0.3\,\%)^2. \tag{2.2}$$

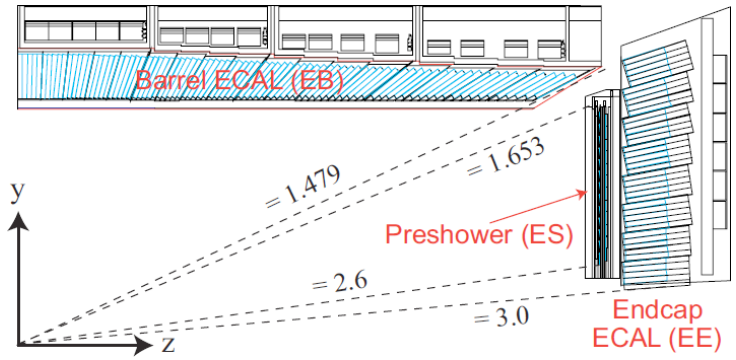

Figure 2.5.: Schematic view of the electromagnet calorimeter with it components in the barrel and the endcaps as well as the preshower. From reference [38].

The Hadronic Calorimeter

In the Hadronic Calorimeter (HCAL) [39] the particles interact by the strong interaction and produce new particles, which results in a hadronic shower of particles. The HCAL is a sampling calorimeter with brass and steel as absorber material and a plastic scintillator to detect the electromagnetic part of the showers.
The HCAL has a big geometrical acceptance of $|\eta| < 5.2$ when including the forward components surrounding the whole ECAL. A big coverage as close to the beampipe as possible is needed in order to derive a correct missing energy determination. The HCAL consists of four sub-detectors, their position inside the detector can be seen in Figure 2.6.

Hadron Barrel (HB)

The Hadron Barrel is located outside the ECAL at a distance of 1.77 m to the beampipe and extends to the solenoid coil at a distance of 2.95 m with an acceptance up to $|\eta| < 1.3$. It is built of layers of 50.5 mm brass and 4 mm plastic scintillator. The emitted light is collected with wavelength-shifting fibers which are attached to hybrid photodiodes. The material accounts for 5.8 interaction lengths λ_1 for $\eta = 0$ and extends up to 10.6 interaction lengths for $\eta = 1.3$

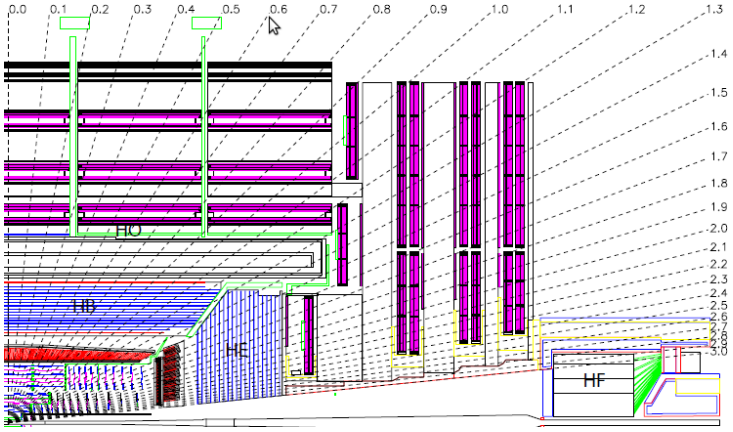

Figure 2.6.: Overview of the different elements in the hadronic calorimeter. From reference [32].

Hadron Endcap (HE)

The detection mechanism in the Hadron Endcap is the same as for the Hadron Barrel, it covers the range $1.3 < |\eta| < 3.0$ and accounts for 9-10 interaction lengths.

Hadron Outer (HO)

In the very central region $|\eta| \sim 0$ the HB and the ECAL do not provide enough radiation length to stop particles that are produced late in a shower. Therefore another detector was designed, the Hadron Outer, which works as a tail catcher for the showers. It utilizes the solenoid coil as an absorber, therefore a layer of scintillator is placed directly behind the solenoid coil, which is read out by wavelength shifting fibers. With this additional material the interaction lengths of ECAL, HB and the solenoid coil add up to 11.8 λ_I.

Hadron Forward (HF)

In the very forward region about 11.2 m away from the interaction point the Hadron Forward Calorimeter (HF) is located. It is about 3.5 m long and covers the range of $2.9 < |\eta| < 5.2$. Due to the high fluxes in the forward direction different materials are chosen for the Hadron Forward: Steel is used as the absorbing material and quartz fibers are used as the active material. The particles produced emit Cherenkov light, which is detected by photomultipliers.
Combining all parts of the hadronic and electromagnetic calorimeter there is a minimum of at least 11.8 interaction lengths. The overall energy resolution in an energy range of 30 GeV $<$ E $<$ 1 TeV is given by [39]:

$$\frac{\Delta E}{E} = \frac{1\,GeV}{E} \oplus 4.5\,\%. \tag{2.3}$$

2.2.3. The Muon System

The muon system [40] is the outermost part and located in the iron return yoke of the CMS detector. Muons are part of several very important physics signatures, like the decay of the Higgs boson into four muons or many signatures of new physics phenomena.

Therefore the muon system is used for identification and triggering of the muons as well as for measuring their momentum and their charge over a wide acceptance.
Muons are minimum ionizing particles over a wide range of momentum, therefore they can leave the inner parts of the detector and even the iron return yoke without being stopped and they can be detected in the muon system afterwards. They are the only particles that are likely to be detected in the muon system.
The muon systems consists of three different gaseous detector types which have their

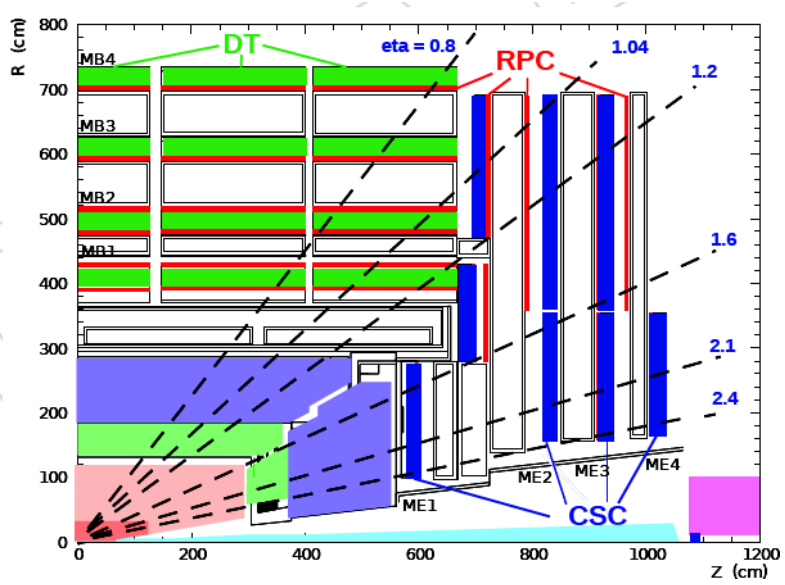

Figure 2.7.: Schematic overview of the different components of the CMS muon system. From reference [41].

specific advantages, their arrangement inside the detector is shown in Figure 2.7. The three different types are the following:

- In the central range of the barrel $|\eta| < 1.2$ the flux of muons and the magnetic field are low. Therefore in this region drift tubes (DT) with their very good spatial resolution are used. They can also used for triggering.
- Due to the higher flux of muons and the strong and non-uniform magnetic field cathode strip chambers (CSC) are used in the endcaps $0.9 < |\eta| < 2.4$. They are faster and have a higher granularity than the DTs used in the barrel region; like the DTs the CSCs can also be used for triggering.
- In both regions, barrel and endcaps, resistive plate chambers (RPC) are used. They have a very fast response of a few ns and provide an independent way of triggering muon events due to their good time resolution. In this way a redundancy is ensured and muons can easier be identified. A down-side of the RPCs is their coarse spatial resolution.

Drift Tubes (DT)

The muons system in the barrel where the magnetic field is rather homogeneous and low ($< 2\,\mathrm{T}$) is built of drift cells, a schematic view can be seen in Figure 2.8. In total

about 170000 of these cells are used and cover up to $\eta < 1.2$. They have a width of 42 mm and a height of 13 mm, and their length varies between 1990 mm and 3020 mm depending on the position inside the detector. Each cell consists of a 50μm anode wire in the middle with an attached voltage of +3600 V and two cathodes with a voltage of -1200 V each. Two field forming electrodes with an applied voltage of +1800 V are placed on the middle top and the middle lower side of each cell.

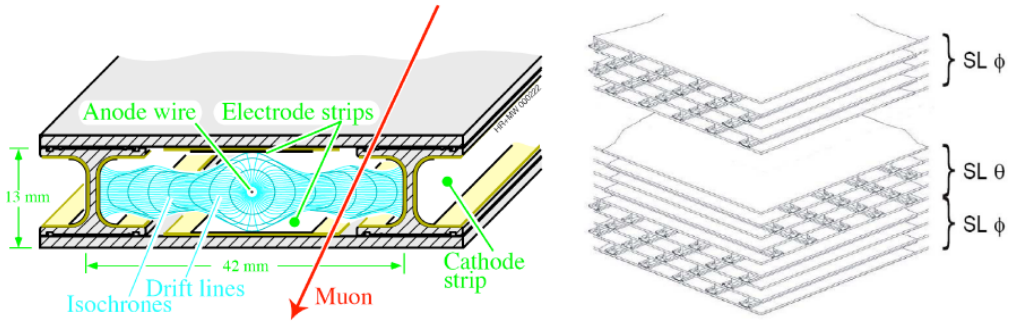

Figure 2.8.: Left: Schematic view of one drift cell. Right: Arrangement of the different layers to form the superlayers, and the superlayers forming the drift chamber. From reference [32].

The cells are filled with a gas mixture of 85 % Argon and 15 % CO_2. Charged particles, mostly muons, traversing the cell ionize the gas producing free electrons and ions. The ions drift to the cathode while the electrons drift to the anode wire. Due to the very strong field close to the anode wire the electrons cause an avalanche of secondary ionization. The measured signal is proportional to the initial ionization of the muon. The electric field inside the cell has a sufficient linear dependence of the drift time and the drift path; with a drift-velocity of 55 μm/ns the maximal drift time is 380 ns for the maximal drift-path of 21 mm.
Four layers of drift cells are arranged to form the so-called superlayers as shown in Figure 2.8. Neighboring layers are displaced by half a drift sell size to reduce ambiguities in the reconstruction. These superlayers are combined to from the drift tube chambers. The drift chambers are arranged around the beampipe forming concentric cylinders in the r-ϕ projections at four different radii, called MB1 - MB4, with 60 chambers in the three inner cylinders and 70 in the outer cylinder resulting in 250 total drift chambers. The MB1 chambers are placed directly outside the Hadron Outer, the MB2 and MB3 are inside the iron yoke. The MB4 is just outside the iron yoke, it is building the most outside part of the CMS detector. The chambers MB1 - MB3 consist of three superlayers, while the MB4 only consists of two superlayers. The outer superlayers of MB1 - MB3 are arranged with the anode wire parallel to the beampipe to measure inside the magnet bending plane (r-ϕ) and the middle one being rotated by 90° to measure the z-coordinate, the middle layer is missing in MB4.
The single wire resolution is better than 250 μm and the chambers reach a resolution of 100 μm with 8 track points in the r-ϕ plane.

Cathode Strip Chambers (CSC)

Cathode Strip Chambers (CSC) are used in the endcap to cover the range of $0.9 < \eta < 2.4$, leaving the area of $0.9 < \eta < 1.2$ being covered by CSCs and DTs. Due to the

higher fluxes of particles and the inhomogeneous magnetic field the CSCs were chosen for the endcaps. In total they cover an area of 5000 m^2 and have a gas volume of more than 50 m^3.
The CSCs are multiwire proportional chambers with a trapezoidal shape, see Figure 2.9. Each CSC consists of 7 panels of cathode strips oriented radially allowing them to measure in the ϕ direction. In the middle of the gas-filled-gaps 6 layers of wires are inserted between the cathode panels rotated by 90° to the cathodes to measure the radial coordinate.

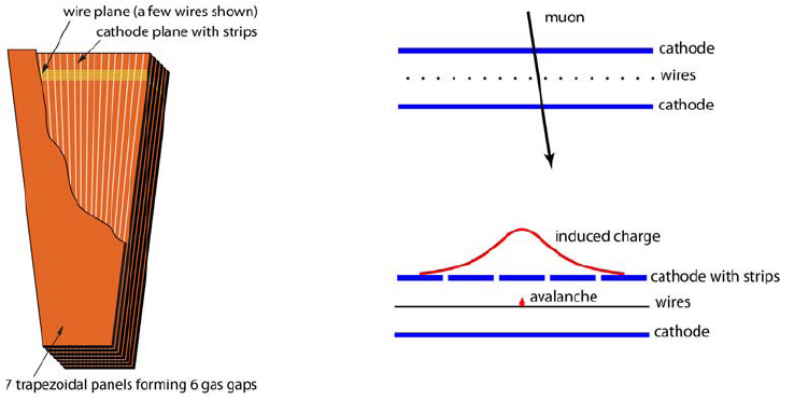

Figure 2.9.: Schematic view of the CSCs used in the endcaps of the CMS detector. On the right the working principle is shown. From reference [32].

The working principle is shown in Figure 2.9. A charged particle passing through the CSCs ionizes the gas, the produced electrons drift towards the wires and produce an avalanche of additional electrons. The moving charged particles induce a charge on the cathodes and due to the segmentation of the electrodes and the measured charge distribution a reconstruction of the track is possible.
The endcap muon system consists of 540 CSCs in total, they are arranged in four disks at each endcap, see Figure 2.7.
The inner CSCs have a narrower wire spacing and reach a spatial resolution of below 50 μm while the outer ones reach a resolution of about 80 μm.

Resistive Plate Chambers (RPC)

Resistive Plate Chambers (RPC) are gaseous parallel-plate detectors with a coarser spatial resolution then the other two muon detectors but with an excellent time resolution of only a few ns. They are fast enough to separate between different bunch crossings, which have a minimal spacing of 25 ns, and therefore are mainly used for trigger purposes. In the barrel six layers of RPCs are used and three in the endcaps, see Figure 2.7. The structure of a RPC is shown schematically in Figure 2.10. The CMS RPCs are made of two gas filled chambers with a gap width of about 2 mm and operate in "Avalanche Mode". Each of these chambers is embedded in two bakelite plates which are coated with conductive graphite to from the electrodes. A high voltage of up to 12 kV can be applied to the electrodes. To read-out the signal, aluminum strips are positioned between the resistive plates, see Figure 2.10. The aluminum is separated from the graphite coating by a thin insulating film. Due to the double structure the RPCs do not have to operate

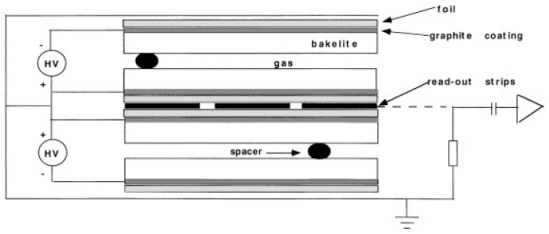

Figure 2.10.: Schematic design of the Resistive Plate Chambers (RPC) used in the barrel and the endcap. From reference [38].

at the maximum voltage to achieve the needed efficiency; the lower voltage reduces the aging.
A muon passing through the gas filled gaps ionizes the gas which starts an avalanche effect, the drifting charged particles induces a 'fast charge' in the aluminum which is read out and used as a signal.
By the combination of the muon system and the inner tracker a transverse momentum resolution of about 10 % for very high energetic muons ($\sim$ 1 TeV) is achieved, see Section 3.

2.3. Trigger System

The LHC is designed to produce a very high event rate in proton-proton collisions. A bunch spacing of 50 ns corresponds to a bunch collision frequency of 20 MHz, at each bunch collision about 20 simultaneous proton-proton collisions happen due to the very collimated proton bunches.
It is impossible to store and process the resulting data of each of the events, therefore a drastic reduction of the events to be analyzed has to be achieved. This is done in a two-staged trigger system which leads to a factor of event reduction of about 10^6 [32,42]. The rate which can be processed and stored is about 100 Hz.
The trigger system is divided into two separate parts, the Level-1 (L1) trigger, which consists of custom-designed and largely programmable electronics, and the totally software based High-Level-Trigger (HLT), which gets processed on a processor farm of about one thousand processors.

The Level-1 Trigger

The L1 trigger uses coarsely segmented data from the muon system and the calorimeters, but not the tracker. The high-resolution data used in the HLT is held for about 3.2 μs in the front-end electronics. The L1 trigger has to analyze every event and has an output rate of about 100 kHz.

The structure of the L1 trigger system can be seen in Figure 2.11, it can be divided into local, regional and global components. The Local Triggers use energy deposits in the calorimeters and track segments and hit patterns from the different muon chambers. The Regional Triggers combine the information provided from the Local Triggers. The trigger objects are ranked according to their energy or momentum and their quality. The quality is based on the amount of information and the confidence with which the

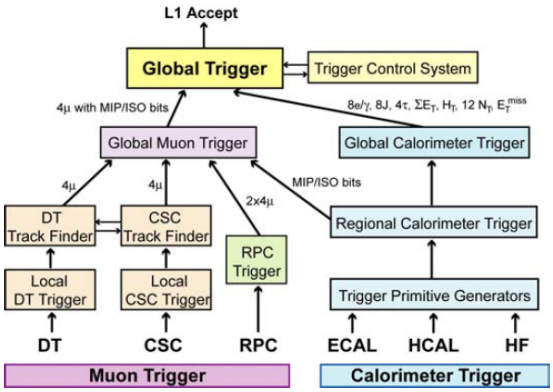

Figure 2.11.: Overview of the local, regional and global components of the L1 trigger chain. From reference [42].

parameters where measured. The Global Muon and Global Calorimeter Trigger then determine the highest ranked trigger object of the whole CMS detector and pass the information to the Global Trigger, the end of the L1 chain. The Global Trigger then decides whether to pass the event to the HLT or not. The decision is based on calculation algorithms and the readiness of the different subdetectors and the data acquisition system and has to be done in the 3.2 μs.
Muons are particularly interesting in this analysis, therefore the muon L1 trigger will be described briefly [32]. All three subsystems of the muon system, the DT, CSC and RPC, take part in the trigger, especially all of them are used to assign the right bunch crossing. In the barrel the DT provide track segments in the ϕ projection and hit patterns in the η projection, while the CSC provide three dimensional track segments in the endcaps. The Regional Trigger joins the segments of different DTs and CSCs and completes the track and assigns physical parameters to them. Also some information from the RPC hit patterns are taken into account at this step.
The Global Muon Trigger gets up to four muon candidates from the DTs and four candidates from the CSCs, and up to eight candidates from the RPCs, four in the barrel and four in the endcaps, see Figure 2.11. Each of the candidates has an assigned value for p_T, η and ϕ as well as an assigned quality code. Then the information of the different subdetectors are merged. In a first step the candidates of the RPCs are matched with the ones from the DTs and CSCs. In a second step also the different barrel and endcap candidates in the overlap region are merged to prevent double counting.
Also some data from the Calorimeter Trigger are used to check the isolation and the hypothesis of a minimal ionizing particle (MIP), therefore the tracks are extrapolated through the calorimeters to the vertex and the needed isolation and MIP information are passed to the Global Trigger. The Global Muon Trigger then provides a list of four muon candidates, which are passed to the Global Trigger. The events are sorted by the transverse momentum and the quality.
The Global Trigger then takes the decision to accept the event based on the information passed from the Global Muon Trigger and the Global Calorimeter Trigger. Besides the transverse momentum and the η and ϕ coordinates also the charge, isolation and the MIP information are available to take the decision. In case the event is accepted it is passed to the High-Level-Trigger (HLT).

The High-Level-Trigger

The HLT [43] is purely software based and reduces the event rate by a factor of 10^3 to the order of 100 Hz. The HLT can basically use all the information of the event, therefore a multitude of different HLTs is possible. The muon reconstruction starts with the muon candidate of the L1 trigger and improves the fit taking into account the detector material. Afterwards, in a second step the information from the muon system is combined with the corresponding hits in the tracker to form a trigger object close to the one used in the offline analysis. For both steps the Kalman-filter [44] technique is used.
In this analysis only Single-Muon triggers are used, they consist of a single muon trigger object with a sufficiently high p_T threshold. In the year 2011 the threshold varied between 24 and 40 GeV due to changes in the instantaneous luminosity.

2.3.1. Data Acquisition and Data Distribution

The high event rate of the LHC is a big challenge for the data acquisition system(DAQ). As stated previously the L1 trigger reduces the rate from 40 MHz to about 100 kHz. With a typical eventsize of 1 MB the total rate that has to processed by the HLT and the processor farm is about 100 GB/s. Every event that passes the L1 trigger is sent to the processor farm, where a physics selection is performed by using faster versions of the offline reconstruction software. The reduction due to the HLT has to be about 1000 and in case an event is accepted by the HLT it is stored. The DAQ of CMS is shown schematically in Figure 2.12.
To handle the remaining amount of data the LHC Computing Grid [45] is used. One

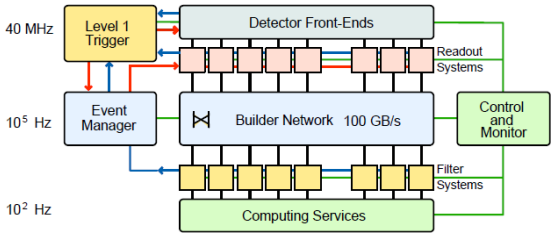

Figure 2.12.: Schematic view of the CMS DAQ system with the expected rates. From reference [43].

copy of the recorded data is stored at the computing center at CERN, called the Tier-0, where it can be processed to produce reconstructed datasets. From here it can be distributed to the Tier-1 computing centers, where also reconstruction, computation intensive analyses and simulations are performed. Besides the Tier-1 computing centers there are also Tier-2 computing centers, they are used for storing small parts of the datasets and performing the physics analysis.

2.3.2. Luminosity Measurement

Apart from the center-of-mass energy the luminosity is the most important quantity for the LHC experiments, because it allows to relate between the cross section σ and the event rate $\dot{N}$ of a specific process:

$$\dot{N} = \mathcal{L} \cdot \sigma \tag{2.4}$$

with the instantaneous luminosity $\mathcal{L}$. There are several ways to determine the luminosity, here only a brief summary of the most important ones is given:

- The first method is based on Formula 2.1. Since the revolution frequency, the number of bunches and the protons per bunch can be measured easily, the only remaining quantity is the effective overlap area of the beams. The effective overlap area can be measured with a "Van der Meer Scan" [46], where the beams are scanned through one another in the transverse direction. By recording the event rate as a function of the beam separation in the x and y direction the beam profile can be obtained, which then allows to make the absolute luminosity determination. These "Van der Meer Scans" are only executed when the beam parameters change, therefore they are only performed a few times per year.

- The instantaneous luminosity is time dependent, so besides the absolute calibration also a measurement of the luminosity per bunch crossing is needed. Therefore the Hadron Forward Calorimeter is used. From the energy deposit in this part of the detector, to be more precise from the number the towers without energy deposit, it is possible to determine the number of interactions per bunch crossing [47]. This number of interactions is related to the instantaneous luminosity and therefore allows to determine the time dependence. Since this method can be applied online, it is used to monitor the development of the luminosity. However, there are some non-linearities and dependencies on earlier bunch crossings, which have to be taken into account for a precise measurement. This is done in the offline luminosity determination.

- Another way to determine the number of interactions is to use the Pixel Cluster Counting Method [48]. Due to the very high number of pixels in the inner tracker the probability for one pixel being hit by more than one track is extremely small. The number of pixels is directly related to the number of tracks, which is a linear function of the number of interactions and hence allows a measurement of the luminosity.

Based on the first two methods the absolute calibration of luminosity is determined with an systematic uncertainty of 4.5 % [49], which is used in this analysis. The Pixel Cluster Counting Method yields a smaller uncertainty, but the study was not finished at the time of this analysis.

3. Reconstruction and Object Definition

In the following the reconstruction of the two most interesting objects in this analysis, the muon and the missing transverse energy, is explained briefly.
The reconstruction of muons is described in full detail in [41, 50]. There are three goals for the muon reconstruction:

- Identifying tracks belonging to a muon with the muon system.
- Measuring the momentum of the muon.
- Measuring the charge of the muon.

One special challenge in the reconstruction is the design of the CMS detector with the iron in the muon system, which causes high energetic muons to shower.

3.1. Muon Reconstruction

The subsystems of the CMS detector only detect a particle when it travels through the active material. The resulting signals are individual points, also called hits. These individual hits have to be arranged together to form the muon's trajectory in order to determine the muon's charge and momentum.
Due to the Lorentz force the trajectory of the muon is bent in the magnetic field of the CMS detector. From bending it is possible to measure the momentum and the charge of the muon. There are some conditions due to the design of the CMS detector and the used detector materials:

- The magnetic field is not homogeneous over the whole detector.
- The muon looses energy on its way through the detector due to interaction with the subsystems preceding the muon system.
- The trajectory is deflected in a stochastic manner by multiple scattering.

All these effects have to be included in the reconstruction in order to get a good measurement of the momentum. To describe a trajectory state in a known magnetic field five parameters are needed. In CMS the following five are chosen to characterize a muon state vector at a reference surface z_r: $x, y, \partial x/\partial z, \partial y/\partial z, q/|\vec{p}|$.
The track building algorithm can then be divided into four steps [50]: Trajectory Seeding, Trajectory Building, Trajectory Cleaning, Trajectory Smoothing.

1. **Trajectory Seeding**: In the initial step a starting point, also called seed, for the trajectory building is determined by using an estimated trajectory state (state-based seed) or a set of hits (hit-based seeds). The hit-based seed consists of two or three hits compatible with the beam-spot to build the initial starting vector.

The state-based seeds are specified by an initial momentum and direction, e.g. estimated trajectory parameters by the Level-1 trigger. These seeds are the starting points for the Trajectory Building and already have a defined direction in which the muon traversed the detector.

2. **Trajectory Building**: The Trajectory Building starts from the seed position and searches in the direction specified by the seed for compatible hits in the subsequent detector layers. The track finding and fitting is done by using a combinatorial Kalman filter [44], which uses the whole knowledge of the track parameters at each layer to find compatible measurements in the next layer. The Kalman filter is an iterative approach that updates the trajectory estimate with its covariance matrix by incorporating the material effects. It starts with the trajectory parameters $\tilde{k}_i$ and their covariance at a known surface and then propagates them to the next surface $\tilde{k}_{i+1}$ by taking into account the equation of motion and the material effects. The parameters are then updated with a compatible hit in the next layer. The final trajectory estimate is then weighted according to the measurement in the new layer together with all the measurements of the previous layers. The propagation of the trajectory has to take into account the inhomogeneous magnetic field in the detector and the different material effects mentioned before.

3. **Trajectory Cleaning**: In the step of the Trajectory Building a large number of tracks is built. The various hits in the detector are not unambiguously assigned to one track, many of the tracks are sharing some of their hits. In the Trajectory Cleaning step these ambiguities between the trajectories are resolved depending on the type of reconstruction that is chosen. In most of the cases the combination of hits with the lowest χ^2 is chosen.

4. **Trajectory Smoothing**: In the last step the trajectory is fit backwards, this allows to apply all covariance matrices to the intermediate points, so that the whole information available is used for building the trajectory.

3.2. Reconstruction Algorithms

There are several muon reconstruction algorithms [41, 50] depending on which detector subsystems are used for the reconstruction and where the reconstruction starts.

Standalone Muon

The standalone muon track only uses the muon system, but not the tracker. The track reconstruction can start from an offline seed or a Level-1 estimated track determined online and recorded in the data. If the building starts in one of the outer chambers (MB2-4), then the trajectory is propagated to the innermost muon chamber to search for a matching segment. Then a pre-filter is applied propagating the track back to the outside of the muon system (inside-out) to improve the primary seed. Afterwards the main filter is applied, the filter propagates from the outside-in and decides which hits in the muon system are used depending on the χ^2 of the fit. As a final step the trajectory is extrapolated to the point of closest approach in the beamline imposing a constraint on the nominal interaction point, thus improving the momentum resolution.

Inner-Track

Similar to the "standalone-track" the "tracker-only"(also "inner-track") also uses only one detector sub-system. The "tracker-only" reconstruction only uses the measurements from the silicon tracker, but not the muon system. The "tracker-only" approach is useful for very low energetic muons, where the resolution is determined by the high resolution tracker.

Global Muon

The global muon algorithm uses a different approach, it combines the hits of the tracker and the muon system as already planned in the technical design report [40] in order to obtain a more accurate measurement. It starts from the "standalone-muon-tracks" in the muon system and extrapolates them to the tracker (outside-in) allowing a certain volume of η and ϕ in the tracker. In the tracker volume tracks are considered as candidate tracks, if the transverse momentum p_T of the "inner-track" is within 60 % of the standalone p_T. Then in a next step the "standalone-track" from the muon system and the candidate tracks are combined to a common surface implying more stringent matching criteria on the spatial distance and the measured momenta. For successful matches a refit is performed as a last step in which hits can be removed from the fit, if the χ^2 improves significantly. If more than one combination is possible, the one with the lower χ^2 is chosen.
Due to the combination of the tracker and muon system the global muon shows a good performance over a wide momentum range, see Figure 3.1.

Tracker Muon

A similar approach is done for the "tracker muon", but instead of the outside-in approach it starts from the "inner-track" and tries to find matching muon hits, inside-out. This is particular useful for muons with very low momenta, because these are very likely to only get a few hits in the muon system, therefore they are not producing any seeds in the muon system. However the muon system is still used for the identification of the muon.

Refit Algorithms for TeV Muons

In this analysis very high energetic muons with momenta of several hundred GeV are of interest. At such high energies the muon track is nearly straight and radiative processes, which can alter the muon's trajectory, have to be taken into account. Due to the radiation the muon can start an electromagnetic shower and the shower results in extra hits in the muon system, which produce ambiguities for the reconstruction algorithms and may yield a wrong momentum measurement. Therefore a set of so called TeV algorithms were developed to deal with these additional complications:

- Tracker-Plus-First-Muon-Station (TPFMS): The algorithm is a refit of the global fit. It starts with the hits used in the global fit, but then only includes the hits located in the first muon station in the refit. This is done to reduce the impact

of possible showers along the muon's trajectory through the iron. The first muon station is included in the fit, because it is located just before the iron return yoke and therefore the probability of showers is low while a nearly maximal lever arm is used.

- Picky: The Picky fit is also a refit procedure and starts again from the hits from the global fit. Hits from chambers with high occupancy, which is likely due to a shower, are required to have a χ^2 with respect to the trajectory to be below some threshold to be used in the fit. The algorithm therefore picks only the valid hits and uses them in the refit.
- Dynamic Truncation algorithm(DYT): This algorithm does not start at the global fit, but at the "inner-tracks" built in the tracker. It then propagates the tracker only fit to the muon stations and adds successive additional hits that are compatible with the trajectory.

Cocktail Algorithm

To improve the resolution, especially to reduce the tail of the momentum resolution for very high momenta, a mixture of some of the reconstruction algorithms mentioned before is chosen, the so called "Cocktail" or "Tune-P". It chooses on a muon-by-muon basis between the Inner-Track, the TPFMS and the Picky reconstruction. By default it uses the Picky reconstruction. If the tail probability of the Inner-Track fit is significantly better than the one from the Picky fit, it switches to the Inner-Track fit. Finally it compares the chosen track to the one from the TPFMS track, changing again if the tail probability improves.

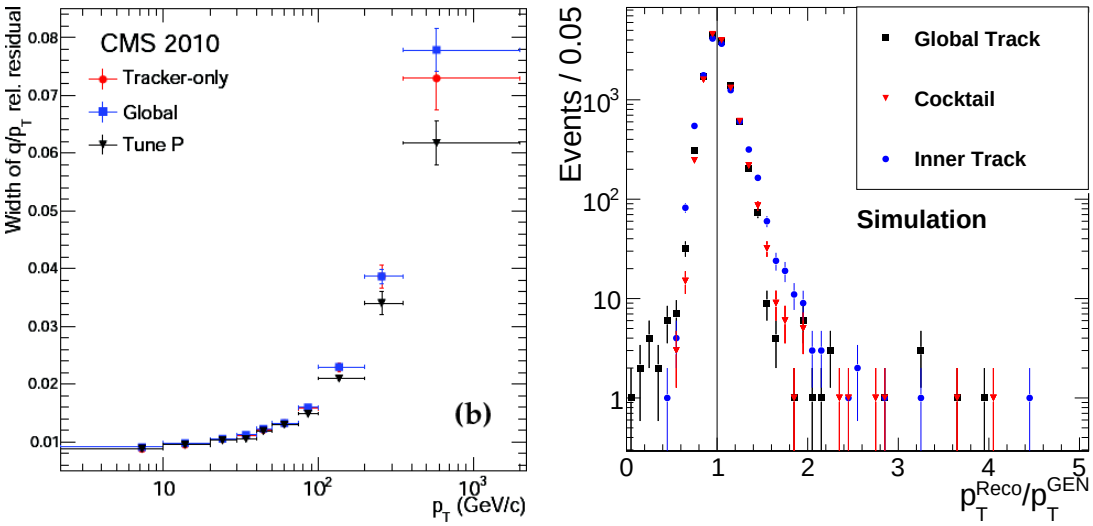

Figure 3.1.: Left: Resolution of the Cocktail, the Global and the Tracker-only muon reconstruction as a function of the muon p_T measured with cosmic muons in 2010. From reference [41]. Right: Ratio of reconstructed p_T to the generated p_T for the different algorithms using a simulated W′ sample.

In Figure 3.1 the muon momentum resolution as a function of the muon p_T is shown for the Cocktail (Tune-P), the Global and the Inner-Track (Tracker-only) reconstruction.

The Cocktail (Tune-P) algorithm shows the best resolution for very high p_T. In the right picture also the ratio of reconstructed p_T to the generated p_T is shown for one simulated W′ sample. The three algorithms show good agreement, the Inner-Track shows a wider peak, which is due to the worse resolution for high-p_T muons. The Global algorithm reconstructs some of the muon with a too low transverse momentum, which results in a few events at the very beginning of the distribution. The distribution for the Cocktail algorithm is the narrowest one with only a few outliers, hence the Cocktail algorithm and the corresponding track are used in the analysis.

3.2.1. Particle-Flow

The particle-flow reconstruction [51] uses a combination of all CMS subdetectors to reconstruct and identify all stable particles and measure their directions, energy and type. This algorithm ensures that for each type of particle the best detector component is chosen enhancing the overall event resolution.
From the list of reconstructed particles "higher-level" particle-based objects can be constructed, e.g. hadronic jets or the missing energy. Due to the reconstruction on the basis of individual particles this particle-flow results in the best possible resolution as well as knowledge about these high-level objects. For this analysis the "Missing Transverse Energy" (MET or $\vec{\not{E}}_T$) is taken from the particle-flow algorithm.
The particle-flow algorithm focuses on reconstructing particles over the whole momentum range including very low energetic muons, therefore it does not use the Cocktail muon reconstruction, but the Global muon reconstruction. In order to be consistent throughout the analysis, the missing energy has to be adjusted for the difference of the particle-flow muon p_T measurement and the Cocktail muon p_T measurement. In the majority of events both reconstructions agree reasonably well, but in in a handful of events this correction has a severe impact and has to be taken into account.

Missing Transverse Energy - MET

In the initial state the colliding partons have negligible transverse momenta. By momentum conversation the final state has to have negligible transverse momentum as well, so in an ideal case, when all particles get reconstructed perfectly, the vectorial sum of all their transverse momenta should vanish. Some events contain neutrinos, which do not create hits in the CMS detector, so they result in missing energy, this is the so-called physics content of the MET. Unfortunately not all particles are reconstructed correctly, there are for examples particles that leave the acceptance of the detector and are not measured at all or particle momenta are measured inaccurately, these effects are also contributing to the missing energy. We speak of instrumental MET, because these effects are caused by the limited resolution and the limited acceptance of the detector.
In Figure 3.2 the reconstructed MET is shown as a function of the generated MET for a simulated W′ sample. The generated MET corresponds to the transverse momentum of the neutrino. For small generated MET the reconstructed MET is smeared strongly around the true value, because the instrumental MET is having a significant impact on the reconstructed MET. For higher generated MET this effects looses importance and the agreement between generated and reconstructed MET gets better. For high MET there are some outliers, which are due to mis-measurement of particles energies in the event.

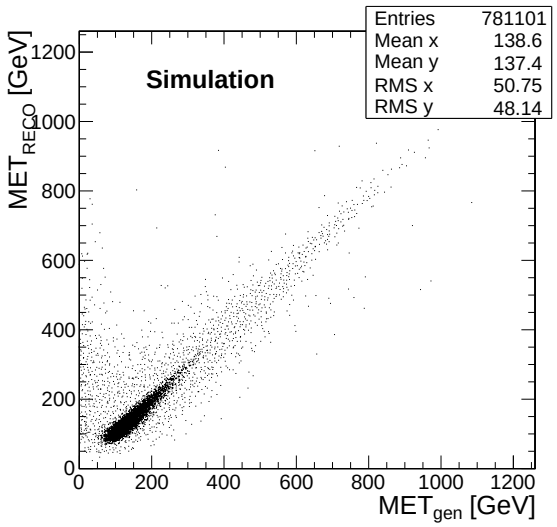

Figure 3.2.: Reconstructed missing transverse energy as a function of the generated missing transverse energy, which is the transverse momentum of the neutrino, for a simulated W′ sample.

The signal in this analysis consists of a muon and a neutrino, the transverse components of the neutrino are represented by the missing transverse energy, which is taken from the particle-flow algorithm, which has shown the best performance.

4. Analysis Framework and Data Samples

In order to analyze the recorded data of the CMS detector and to quantify the results of this analysis Monte-Carlo simulations for the expected background processes and for the signal are needed.
In this chapter the basic tools for analyzing the CMS data as well as the used datasets will be discussed.

4.1. Software Setup

To access the content of the data files the CMS software CMSSW [52] is used. Besides the storing and accessing of event information, CMSSW is also used for the simulation, reconstruction and calibration, therefore some properties of the events are depending on the version. In this analysis the version CMSSW_4_2_5 is used.
Simulated and CMS data events are stored in three basic data formats:

1. RAW: In the RAW data format all the digitalized detector output is stored. On this level of the event storing no reconstruction has been performed, it is the raw output from the detector and the triggering system.

2. RECO: After the reconstruction the events get stored in the RECO data format, all reconstructed physic objects like muons, electrons, jets are available in this format.

3. AOD: In the AOD data format all the high level physics objects are stored, it is a condensed part of the RECO format and should have all the information available that is needed for the different physics analyses. The average size of an event is about 500 kB.

All datasets that are used in this analysis are in the AOD format.
To further reduce the file size the skimmer of the ACSUSYAnalysis framework [53] is used to select only the needed part of the event content and to store it in ROOT [54] trees. This reduces the average filesize by a factor of 50 to about 10 kB per event and makes the local storing of the skimmed data files possible.
For further plotting and analyzing purposes the ROOT [54] framework in the version 5.30.02 is used. The statistical analysis is performed in the RooStats [55] framework together with the Bayesian Analysis Toolkit [56].

4.2. Data Samples

The analysis is based on the full 2011 dataset of proton-proton collisions at a center-of-mass energy of $\sqrt{s} = 7$ TeV. The time dependence of the integrated luminosity can be seen in Figure 4.1, the total integrated luminosity used in this analysis corresponds to $4.68\,\mathrm{fb}^{-1}$. Only runs that were certified by the data certification group [57] are used, that requires that all sub-detectors were switched on and working during the whole run.

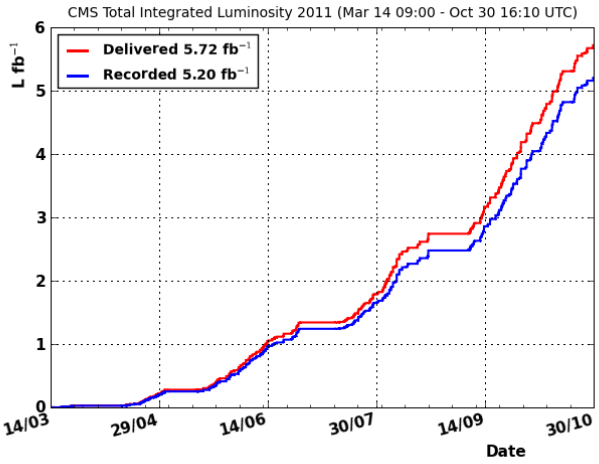

Figure 4.1.: Integrated luminosity as a function of time during data taking in 2011. From reference [58].

Due to the high eventrate the events get divided in runs and lumi sections. To select only good runs and lumi sections, the data certification group provides JSON[1] files containing the certified runs and lumi sections. The JSON files used in this analysis are the following:

`Cert_160404-163869_7TeV_May10ReReco_Collisions11_JSON1_v3.txt`
`Cert_170249-172619_7TeV_ReReco5Aug_Collisions11_JSON_v3.txt`
`Cert_160404-180252_7TeV_PromptReco_Collisions11_JSON.txt.`

The first two numbers in the name of the JSON file indicate the run range for which the JSON files is valid and the name in the middle gives the dataset for which it the JSON should be used.
For this analysis the dataset that is triggered with a single muon trigger is used, it is divided into several parts. The prompt reconstruction is chosen with the exception of two parts, where a rereconstruction was performed. The rereconstruction was needed, because of a change of the CMSSW software and a severe problem in the the electron reconstruction in the prompt reconstruction. A full list of the samples, the run ranges, the used trigger and the corresponding integrated luminosity is available in Table 4.1.

4.3. Considered Background Samples

Monte Carlo samples are used to evaluate signal and background efficiencies as well as to determine the expected background. Therefore simulated events are processed through the full GEANT4 [59] detector simulation, trigger emulation and the event reconstruction chain of CMSSW.
All Standard Model processes that could produce a signal-like signature are considered

[1] JSON = JavaScript Object Notation, a text-based open standard for human-readable data exchange

Dataset	Trigger	Run Range	L(pb^{-1})
/SingleMu/Run2011A-May10ReReco-v1/AOD	HLT_Mu24_v1	160431-163255	48
	HLT_Mu24_v2	163270-163869	169
/SingleMu/Run2011A-PromptReco-v4/AOD	HLT_Mu30_v3	165088-167043	687
	HLT_Mu30_v5	167078-167913	243
/SingleMu/Run2011A-05Aug2011-v1/AOD	HLT_Mu40_v5	170249-172619	368
/SingleMu/Run2011A-PromptReco-v6/AOD	HLT_Mu40_v5	172620-173198	412
	HLT_Mu40_v6	173236-173692	247
/SingleMu/Run2011B-PromptReco-v1/AOD	HLT_Mu40_v6	175832-175921	75
	HLT_Mu40_eta2p1_v1	175973-178420	1620
	HLT_Mu40_eta2p1_v4	178421-180252	812
Total luminosity		160431-180252	4680

Table 4.1.: List of the datasets, the run ranges, the used trigger and the corresponding integrated luminosity.

as possible background events. The signal consists of a high p_T muon and a neutrino, which shows up as missing transverse energy. The main background is the Standard Model W boson, which is in rare cases produced largely off-shell and results in a high-p_T event that exactly looks like a potential W′ event. Besides this there are backgrounds arising from multi-jet(QCD), Drell-Yan, top pairs, single top and diboson events. All the samples are taken from the official Summer11 production [60] and for the Pythia [21] samples the Tune Z2 has been used.
In the following the different backgrounds are explained and how they can produce signal-like events structures is described:

- The most important background source is the Standard Model $W \to \mu\nu$ due to the exact same kinematics as the signal. Especially the very off-shell part of the distribution is interesting, because the produced leptons are highly boosted and produce high-p_T muons. For this important background several generators(Pythia, Madgraph [61] and Powheg [62]) were compared, one important kinematic distribution, the transverse mass (see Section 5), is shown in Figure 4.2. The shape of the distributions is for all generators similar, therefore the combination of the officially produced Pythia $W \to \mu\nu$ sample with a dedicated high-p_T tail was chosen. The high-p_T tail is also produced with Pythia, just with a cut on generator level on a minimum transverse momentum of 100 GeV.

- Besides $W \to \mu\nu$ also the process $W \to \tau\nu$ is important, because the τ is not stable and can decay into a muon with a branching ratio of about 17 % [11].

- Multi-jet events that are produced by the strong interaction. In some rare cases isolated muons like in signal events are produced. Due to the very high cross section of multi-jet events even these rare cases could fake several signal-like events. A muon enriched sample is used, it is produced with the leading order generator Pythia.

- The Drell-Yan process describes the production of lepton pairs in hadron-hadron interactions. If a pair of muons is produced and one of the two muons escapes detection, the remaining one contributes to the background in this analysis. The Drell-Yan sample describing the production of two muons is divided into several p_T-bins to get higher statistics in the tail of the distribution.

- Also the process Drell-Yan into two tau leptons is needed, because one or both of the taus could decay into a muon. Both samples are produced with Pythia.
- Top pairs or events with single top production are another source of potential background. In all top decays a Standard Model W is produced which then could decay into a muon and neutrino with a branching ratio of about 10.6 % [11]. Due to the high mass of the top quark these leptons are boosted and look like the signal events. The top pair events are simulated with the leading order matrix element generator Madgraph [61] and the single top events with the next-to-leading order generator Powheg [62].
- Events containing two bosons (WW,WZ,ZZ) decaying into muons are also considered, these events are generated with Pythia.

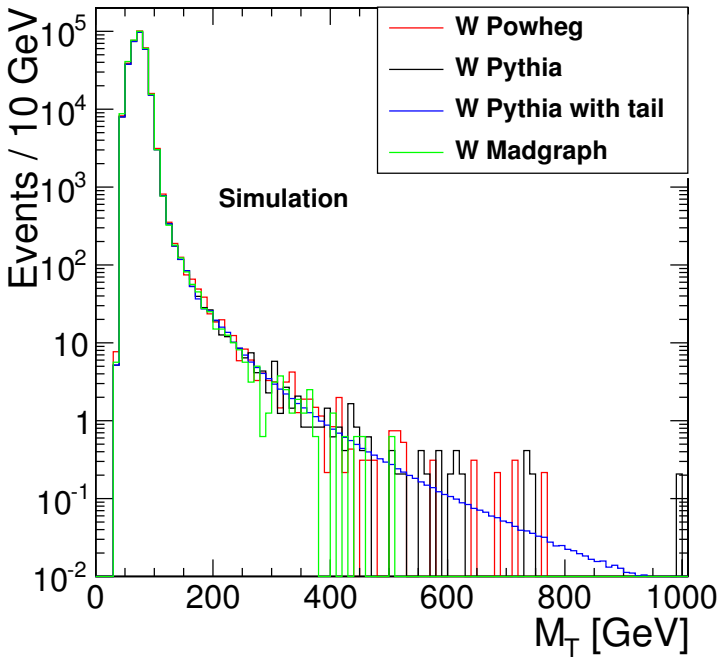

Figure 4.2.: Reconstructed transverse mass distribution of $W \to \mu\nu$ for several generators.

To compare the simulated events to the taken data they have to be scaled according to their cross sections, the number of generated events and to the luminosity in data. Assuming a process has a cross section σ, N events were generated and the data corresponds to an integrated luminosity L, then the total number of expected events would be:

$$N_{exp} = L \cdot \sigma. \tag{4.1}$$

N and N_{exp} can be different, so in order to scale simulation to the data each of the N generated events has to be weighted by:

$$w = \frac{N_{exp}}{N} = \frac{L \cdot \sigma}{N}. \tag{4.2}$$

4.3.1. Parton Distribution Functions

The LHC is a hadron collider with a center-of-mass energy in the proton-proton frame of up to $\sqrt{s} = 7\,\text{TeV}$, but protons are no elementary particles, they consist of quarks and gluons, the so-called partons. The energy that is available to produce new particles is the center-of-mass energy of the colliding constituents of the protons. The center-of-mass energy in the parton-parton frame $\sqrt{\hat{s}}$ is given by:

$$\sqrt{\hat{s}} = \sqrt{x_1 \cdot x_2}\sqrt{s}, \tag{4.3}$$

where $x_{1/2}$ are the fractions of the parton momenta with respect to the total proton momenta. These fractions x have to be smaller than 1 and they follow a continuous distribution, which can be described by parton distribution functions (PDFs). As a result of this, the energy available in the collision varies in each collision and is smaller than the center-of-mass energy of the proton-proton collision. For each parton in the hadron there is a PDF, which gives the probability of finding this parton with the momentum fraction x. The PDFs can only be determined experimentally and they depend on the energy scale Q^2 at which they are evaluated. There are different approaches in determining the PDFs, which results in different sets of PDFs [63, 64]. Two examples are given in Figure 4.3 with the next-to-leading order MSTW2008 PDFs for a proton for two values of the energy scale Q^2.

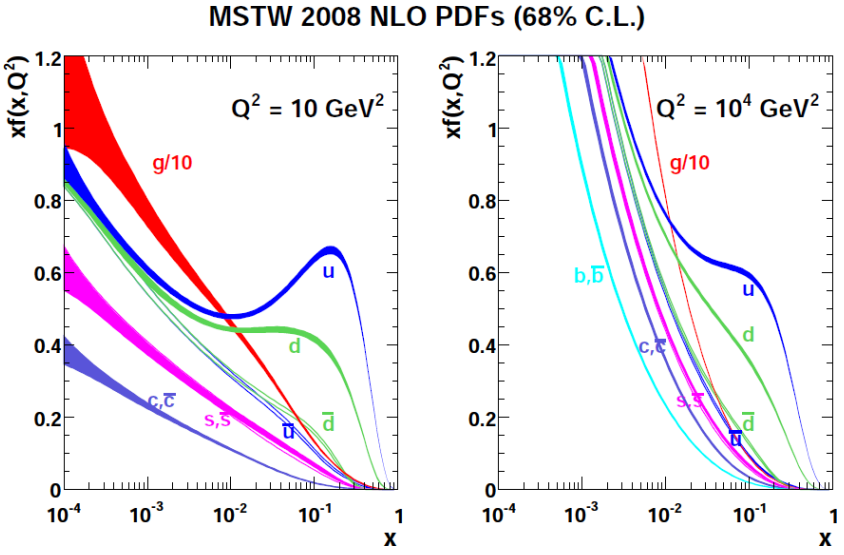

Figure 4.3.: Proton PDFs of the next-to-leading order PDF set MSTW2008, the Q^2 denotes the energy scale at which the PDFs are evalueted. From reference [63].

For large momentum fractions x the probability of the valence quarks of the proton dominates the PDFs. For very low momentum fractions the PDFs of all partons, especially the one of the gluon, increase steeply.

4.3.2. Cross Sections

The PDFs also have an impact on the calculation of the cross section of a specific process in proton-proton collisions, because the center-of-mass energy available in the interaction is depending on the momentum fractions of the colliding partons. In order to get the correct cross section one has to sum over all the partons and integrate over the momentum fractions x of the partons. The resulting cross section can be written as:

$$\sigma = \sum_{i,j} \int_0^1 \int_0^1 dx_1 dx_2 f_i(x_1, Q^2) f_j(x_2, Q^2) \hat{\sigma}_{i,j}(\hat{s}) \tag{4.4}$$

with the momentum fractions of the two partons $x_{1/2}$ and the corresponding PDFs for all partons $f_{i/j}$. The $\hat{\sigma}_{i,j}$ is the cross section of the parton-parton interaction at the center-of-mass energy $\hat{s}$.
The cross section for the various background processes are calculated theoretically [65] [66] for all processes in NNLO[2] except for ttbar and the di-boson processes, which are only calculated up to NLO[3] and the multi-jet background where only the LO[4] cross section is available. Pythia and Madgraph are LO generators and Powheg is a NLO generator, so a k-factor is applied to the generator cross section to get to the higher order cross section.

$$\sigma_{NLO/NNLO} = \text{k-factor} \cdot \sigma_{LO}. \tag{4.5}$$

An overview over the used background samples, their generators, the LO and the higher order cross sections together with their total number of simulated events and the chosen PDF[5] sets can be found in the appendix in Table A.1. The full names of the datasets inside the CMSSW and the computing grid are shown in the appendix in Table A.2.

4.4. Signal Samples

Besides the background samples also signal samples are needed. For the first part of the analysis signal samples were generated using the LO generator Pythia [21]. The model implemented in Pythia corresponds to the benchmark model described in Section 1.4, where the W′ has Standard-Model-like couplings and the decay into Standard Model bosons is not allowed. Also the interference of W and W′ is not implemented in Pythia. Signal samples for W′ masses between 0.5 TeV and 2.5 TeV have been produced with Pythia in 100 GeV steps together with samples for heavier W′ masses of 2.7, 3.0, 3.5 and 4.0 TeV. The samples with masses above 1.0 TeV contain about 17000 events and are taken from the official Summer11 [60] production, the lighter ones are produced privately with about 10000 events.
Even though W′ with Standard-Model-like couplings are excluded below 1 TeV [27] the lighter samples are used to set an exclusion limit on the signal production cross section. This allows to test models with a different signal cross section, to which the exclusion limit on the W′ mass does not apply.
Besides this Pythia signal samples also some samples were produced including certain models of interference, see Section 8.

[2] NNLO = Next-to-Next-to-Leading Order
[3] NLO = Next-to-Leading Order
[4] LO = Leading Order
[5] PDF = Parton density function

4.4.1. Signal Cross Section

In order to weight the signal events according to the luminosity of the data the theoretical signal cross section is needed. The leading-order cross section is calculated directly in Pythia and the NNLO cross sections have been calculated for this model using FEWZ [67]. FEWZ is a software which allows to make predictions of observables like the cross section at NNLO in the strong coupling constant, the calculation is documented in analysis note AN-11-273 [68]. FEWZ allows to calculate the k-factor between the NNLO cross section and LO cross section, which have been calculated with the PDF sets CTEQ6L1 and MSTW2008, respectively, for various W′ masses. The k-factor is then calculated by

$$\text{k-factor} = \frac{\sigma(NNLO, MSTW2008)}{\sigma(LO, CTEQ6L1)} \tag{4.6}$$

and then applied to the LO cross section taken from Pythia generated with the PDF set CTEQ6L1.
A visualization of the LO and NNLO cross section can be seen in Figure 4.4 and the numerical values are shown the appendix in Table A.3 together with the k-factor and the number of generated events for each masspoint.
For a W′ mass of 500 GeV the k-factor is 1.36 and for higher masses the k-factor continuously decreases up to masses of around 2.5 TeV with a k-factor of 1.14. For even higher masses the k-factor increases up to 1.38 for a 4 TeV W′. For small W′ masses the k-factors decrease with the mass of the W′, this implies that for heavier W′ the higher order corrections are getting smaller. The later increase of the k-factors follows from the increasing off-shell production of the W′, which will be shown later. For very heavy W′ the center-of-mass energy of the LHC is not enough to produce the W′ on-shell.

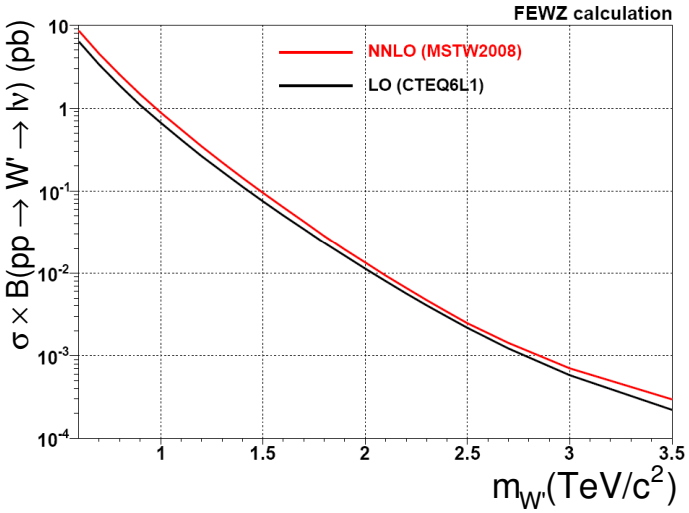

Figure 4.4.: The LO and NNLO cross section times branching ratio as a function of the W′ mass. Adapted from reference [68].

4.4.2. PDF Uncertainties

Another important value to know about the signal is the uncertainty due to the uncertainty of the PDFs. A detailed documentation can be found in analysis note AN-11-273 [68]. The uncertainty on the W′ production cross section due to varying the PDF and the strong coupling constant α_s are calculated according to the PDF4LHC [69] recommendations by using the Les Houches Accord PDF Interface [70] package.
The signal samples are produced with Pythia using the LO PDF set CTEQ6L1. The cross section then gets recalculated using a different PDF set. This is done by applying a weighting factor to each event based on the momenta of the partons producing the W′ and the NLO PDF sets MSTW2008, CTEQ6.6 and NNPDF2.0, which then leads to a different cross section. The different cross sections are calculated for every W′ mass separately.
The result is shown in Figure 4.5 where the PDF uncertainty is shown as a function of the W′ mass. For very light and very heavy W′ the PDF uncertainty is rather small (about 2 %), but for intermediate masses around 2 TeV it rises up to 10 %. This behavior can again be explained by the off-shell production, which starts to dominate for W′ masses above 2.5 TeV, see next Section.

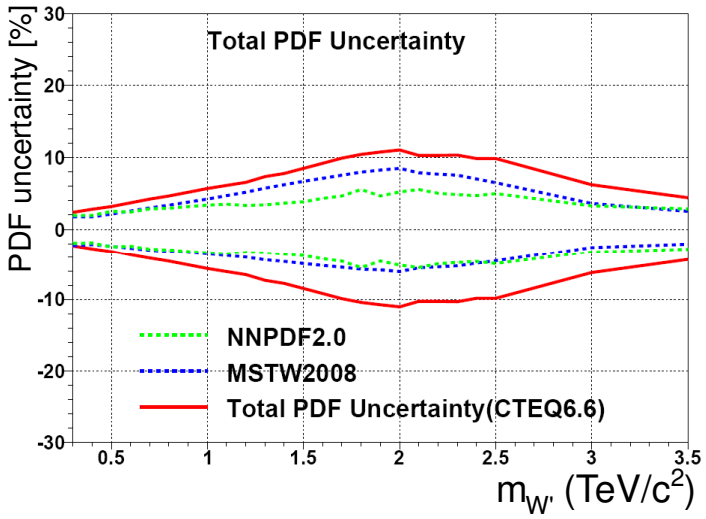

Figure 4.5.: Uncertainites as a function of the W′ mass for various PDF sets with respect to CTEQ6L1 which was used to generate the signal samples. The total PDF uncertainty is shown with the red curve. Adapted from reference [68].

The uncertainties due to the PDF and α_s variations of the three PDF sets are combined. This is done by symmetrizing the maximum upwards and downwards deviation:

$$\text{uncertainty} = \frac{1}{2}[\text{Max}(\text{MSTW2008}, \text{CTEQ6.6}, \text{NNPDF2.0}) - \text{Min}(\text{MSTW2008}, \text{CTEQ6.6}, \text{NNPDF2.0})].$$

5. Signal Selection

After all the objects in the event have been reconstructed, signal like events have to be separated from possible background events. The Feynman diagram describing a W′ decaying into a charged lepton and a neutrino is shown in Figure 5.1.

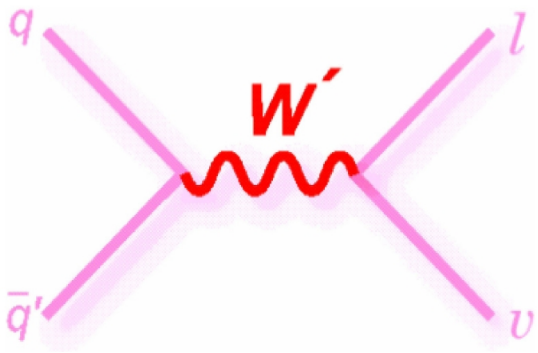

Figure 5.1.: Feynman diagram showing the production of the W′ and the subsequent decay into a charged lepton and neutrino.

The lightest W′ considered in this analysis have a mass of 500 GeV, due to this high mass the generated leptons get a very high momentum of the order of several hundred GeV. Hence the signature consists of a very high-p_T charged lepton, a muon in this case, and a neutrino.
The W′ decays into a muon and a neutrino, so the mass of a potential W′ can be reconstructed by calculating the invariant mass of these both particles, if they are measured completely. The invariant mass distribution is shown in Figure 5.2 for five different samples with masses between 1 TeV and 3 TeV, for this plot the generated and not the reconstructed particle properties are used. For the lighter samples a very narrow peak is visible exactly at the generated W′ mass. The peaks get broader with increasing mass of the W′, this is a result of the linear dependence of the W′ width with the mass, see Section 1.4.
For very heavy W′, especially for the 3 TeV sample, another effect is visible: Many of the simulated W′ bosons have a mass far below the generated mass, there is a second peak in the very low invariant mass region. In order to produce a heavy W′ on-shell, the involved partons are required to carry significant parts of the proton momenta. This second peak is caused by the behavior of the parton distribution functions for low momentum fractions, see Section 4.3.1. The increase of the PDFs for low fractions of the proton momentum enhances the production of the W′ in the low invariant mass region. The cross section of this second peak is rather small, but because of the small on-shell production cross section for heavy W′s the fraction of off-shell produced W′s increases with the mass of the W′. A more detailed description of this effect can be found in Section 7.3 of the Pythia Manual [21]. At the low invariant mass region the background

from other processes is more dominant, that is the reason why such a second peak, if it exists, has never been observed. If the resonant production is studied, a limit on the mass of the produced W′ can be applied, which lowers the signal cross section for the heavy W′ samples. However, this limit on the produced W′ mass is not needed in this analysis, because events with off-shell produced W′s do not survive the signal selection and therefore do not contribute to the analysis.

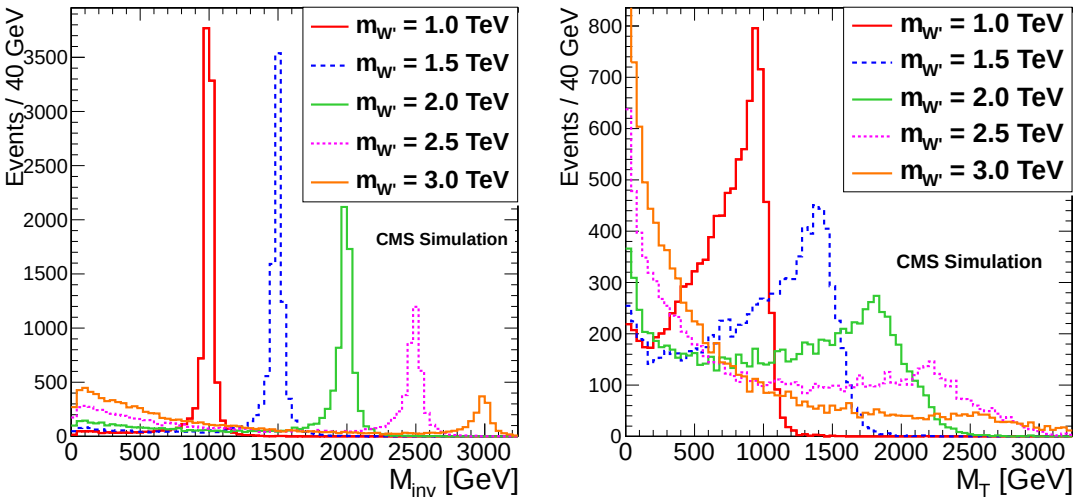

Figure 5.2.: Left: Invariant mass distribution for W′ masses between 1 TeV and 3 TeV using the generated particle information. Right: Generated transverse mass distribution with the typical Jacobian Peak for the same W′ samples.

5.1. The Transverse Mass

The emerging neutrino cannot be detected directly by the detector, but at least the transverse components can be detected indirectly: The initial state has no transverse momentum, therefore by momentum conservation the final state has to have none as well. If all other particles are reconstructed and the sum of the transverse component of their momentum differs from zero, the remaining part is called the missing transverse energy (MET) and represents the neutrino. The MET of the signal events is based on real physical content, the neutrino, and not caused by instrumental MET. Neutrinos are the only Standard Model particle that contribute to the missing energy.
Only the transverse component of the neutrino can be reconstructed, so that the invariant mass is not available. The so called transverse mass M_T can be calculated instead:

$$M_T = \sqrt{2 \cdot p_T^{\mu} \cdot p_T^{\nu} \cdot (1 - \cos \Delta\phi_{\mu,\nu})}, \tag{5.1}$$

$$= \sqrt{2 \cdot p_T^{\mu} \cdot MET \cdot (1 - \cos \Delta\phi_{\mu,MET})}, \tag{5.2}$$

where p_T^{μ} represents the transverse momentum of the muon and p_T^{ν} the transverse component of the neutrino, which is the missing transverse energy. In Figure 5.2 the generated transverse mass distribution for a potential W′ with masses between 1 TeV and 3 TeV

is shown. In contrast to the invariant mass spectrum, where a Breit-Wigner shape is expected, the transverse mass shows the characteristic Jacobian Peak. The signal rises with the transverse mass up to the peak at $M_T = M'_W$, where it starts to fall rapidly, this shape is obtained by projecting the Breit-Wigner into the transverse plane. The clean Jacobian Peak structure is most visible for light W′, for heavier W′ it is also visible that the peak gets broader due to the increasing width of the W′. Also the increasing off-shell part can be seen in this distribution. For increasing on-shell mass of the W′ an increasing fraction of events is produced with very small transverse mass.
In Figure 5.3 the reconstructed transverse mass of potential signal with a W′ mass of 1.5 TeV is shown for the decay into a muon and a neutrino as well as for the decay into a electron and a neutrino. The resolution for measuring high energy electrons is much better than the resolution of high energy muons, because the electrons get fully absorbed in the crystals of the electromagnetic calorimeter. Therefore the Jacobian Peak in the electron channel is much more narrow and less smeared out.

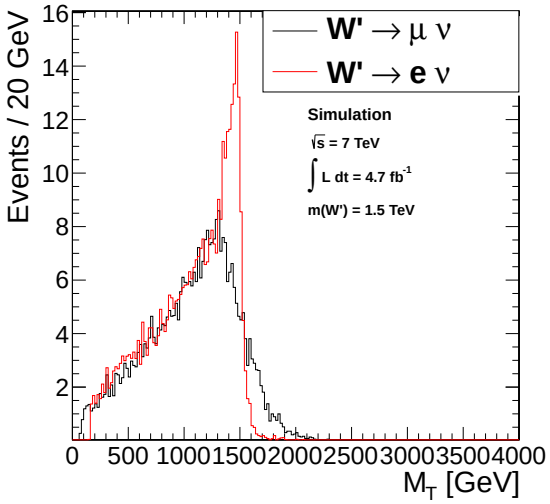

Figure 5.3.: Reconstructed transverse mass showing the Jacobian Peak of a W′ with mass of 1.5 TeV in the electron channel and the muon channel.

The transverse mass distribution is the main analysis distribution and will be used for the statistical analysis later on, but first some quality and analysis criteria have to be applied to select only well reconstructed W′ candidate events and reduce the possible Standard Model background.

5.2. Muon Selection

The W′ in this channel decays into a muon and neutrino, in the W′ rest frame both of these leptons will get the same amount of momentum due to momentum conversation. In most of the cases both leptons get very high momenta of several hundred GeV due to the high mass of the W′ , this is a unique property and very rare in Standard Model processes.
As already mentioned before there are dedicated muon algorithms for these so called TeV-muons; the Cocktail algorithm [41] shows the best performance and is chosen for

all p_T-measurements.
The selection criteria will now be explained and a summary can be found in Table 5.2.

Trigger and Acceptance

As a first selection step a trigger is required and for this analysis a single muon trigger is suited best. During 2011 data taking the minimum p_T threshold of the lowest unprescaled trigger increased several times, starting from 24 GeV to 40 GeV in the end. In the simulated MC events only the trigger with the trigger threshold of 24 GeV is chosen even though higher values are simulated as well. These thresholds are way below the muon momentum of the signal events, so the analysis is not divided in different pieces with varying p_T values.

- A minimum muon p_T of 40 GeV is required for all the events in addition to the trigger requirement. The selection threshold was adjusted to match the highest trigger threshold.

- The muon trigger system is instrumented in the geometrical acceptance range of $|\eta| < 2.1$. Therefore all the considered muons have to be in this geometrical acceptance of $|\eta| < 2.1$.

Muon Quality Criteria

The next selection steps are used to make sure that the reconstructed muon is well reconstructed. A set of selection criteria on the reconstructed track and the isolation is made following the CMS Exotica muon recommendations [71]. There are several analyses using high energetic muons, therefore a set of selection steps ensuring well reconstructed muons is provided by the Exotica Group. The selection steps are based on the "tight" muon identification recommendations by the CMS Muon Physics Object Group [72] with some slight variations. The different criteria will now be explained in more detail:

- First of all every muon has to be reconstructed as both tracker and global muon, this means that the inside-out and the outside-in algorithms reconstruct the muon, cf. Section 3. The standard muon ID only requires a global muon.

- There have to be at least two muon stations which contain segments. This is done in order to avoid "punch-through" events. "Punch-through" describes hadrons that leave the hadronic calorimeter and enter the muon system. Due to the iron in between the muon chambers the hadrons can only enter the first one and are absorbed in the iron. The two muon stations can be seen in the event displays, see Appendix B, where in each of the events the muon was detected by at least two muon stations.

- Of these hits in the muon system at least one has to be valid for the global fit. The global fit is not used directly in this analysis, but some of the muon reconstruction algorithms entering the Cocktail algorithm are using a refit of the global fit, therefore this selection criterion is used.

Besides the muon system there are also some requirements on the quality of the detected muon in the silicon tracker.

- In the innermost part, the pixel vertex detector, at least one pixel has to have fired. This is needed in order to reconstruct the vertex at which the muon is produced.
- In the CMS standard muon identification recommendation there should be also at least 10 hits in the complete tracker, meaning pixel and strip part of the tracker. Requiring only the ten hits produces some outliers, which have an uncertainty of the order of 100 % on their p_T-measurement, see Figure 5.4. The transverse momenta for the different TeV reconstruction algorithms, see Section 3, of the three events with the biggest uncertainty on the measurement is shown in Table 5.1.

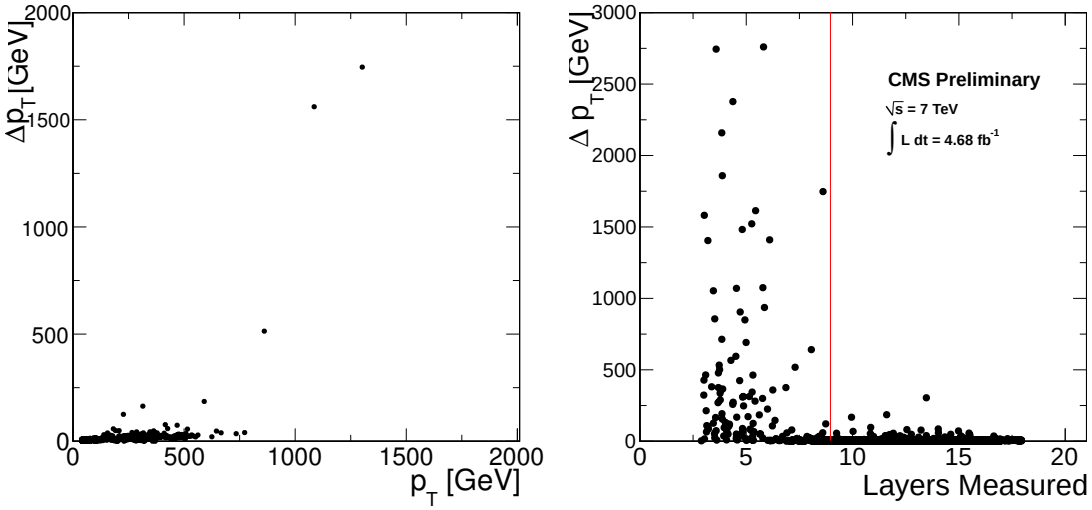

Figure 5.4.: Left: Uncertainty on the p_T measurement as a function of p_T after requiring at least 10 hits in the tracker without any requirement on the number of layers. There are clearly 3 outliers visible with huge uncertainties on the measurement. Right: Uncertainty on the p_T measurement as a function of the measured layers in the tracker without the requirement of at least 10 hits in the tracker. The red line indicates the optimized selection value.

Reconstruction algorithm	Event 1	Event 2	Event 3
Cocktail [GeV]	860 ± 520	1090 ± 1560	1310 ± 1740
Inner-Track [GeV]	860 ± 520	1090 ± 1560	1310 ± 1740
TPFMS [GeV]	134 ± 7	81 ± 7	206 ± 17
Picky [GeV]	155 ± 9	150 ± 24	172 ± 6
Global [GeV]	124 ± 6	136 ± 19	2310 ± 2010

Table 5.1.: Transverse momenta of the different reconstruction algorithms for the three outliers in Figure 5.4.

In all three of these events the Cocktail algorithm chooses the "Inner-Track", whose reconstructed p_T value is different from the other algorithms by one order

of magnitude. The reason for this high uncertainty on the transverse momentum is that all these events have only a small number of layers that have measured the muon.
Fortunately the selection criterion on the number of hits has been optimized for Exotica Muon purposes and replaced by a requirement on the number of layers, which have detected the muon, to be larger than 8. This has been done because muons with less than 9 layers have a higher fake rate [73] and also the uncertainty on the p_T-measurement decreases with the number of measured layers. The three events discussed before are clearly mis-reconstructed, but by applying this layer requirement instead of the number of hits requirement these events are removed.
The uncertainty on the p_T-measurement Δp_T as a function of the measured layers can be seen in Figure 5.4 on the right, where for less than 9 measured layers the uncertainty on the p_T measurement increases drastically.

- In the CMS standard muon identification recommendation there is also a very loose requirement on the global track fit, the $\chi^2/ndof$ of the fit has to be smaller than 10. Following the $Z' \to \mu\mu$ analysis [74] this selection criterion is dropped for high-p_T searches, because it introduces some inefficiency for high-p_T muons. Such a high $\chi^2/ndof$ normally indicates a bad fit, however, the $\chi^2/ndof$ of the Cocktail track fit is always smaller than 5.

Vertex Reconstruction

Only events with at least one good reconstructed primary vertex are considered in the analysis. The criteria for a good primary vertex are the following:

- There are at least 4 degrees of freedom (tracks) associated to the vertex.
- The distance in the longitudinal direction is less than 24 cm.
- There is only a small probability that the vertex is a faked vertex.

5.2.1. Transverse Impact Parameter d0

As a next criterion the transverse impact parameter d0, that is the transverse spatial distance of the muon track to the primary vertex, is required to be less than 0.02 cm. The primary vertex is in case of multiple reconstructed vertices the vertex, where the sum of all transverse momenta of the associated tracks is the biggest. The d0 has to be lower than the threshold of 0.02 cm, which is one order of magnitude tighter than the standard CMS Exotica muon recommendation. The distribution of the transverse impact parameter can be seen in Figure 5.5.
The standard recommendation [72] is to cut on a value of 0.20 cm, but more than 99 % of the signal events are accumulated in the first bin of Figure 5.5 which contains all events with $d0 < 0.02$ cm. By tightening this threshold one order of magnitude the signal efficiency gets lowered by less than 1 %, but a lot of background events, especially the ones coming from multi-jet interactions, are removed. The main background, $W \to \mu\nu$, shows d0 distribution similar to the signal. The tightening also allows to determine the cosmic contamination, see Section 5.5.

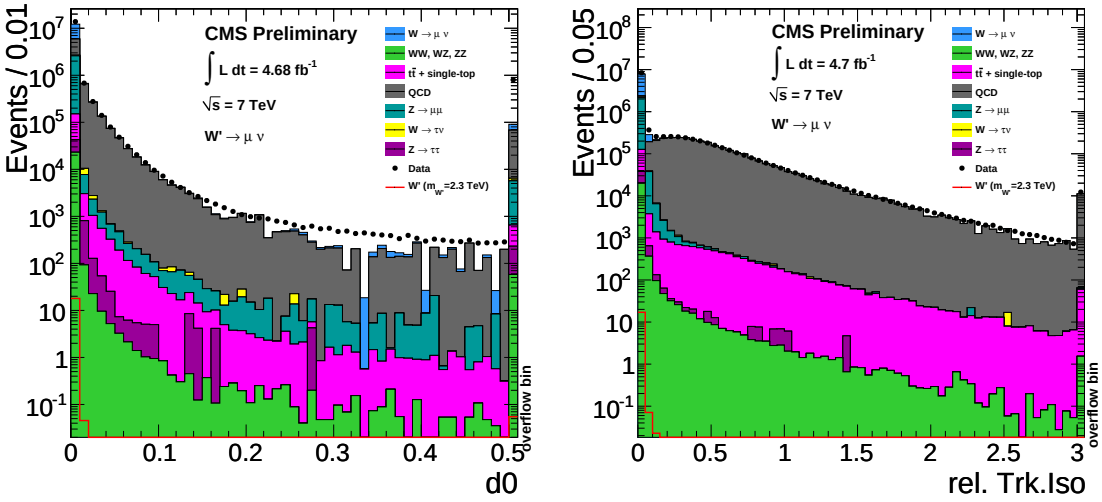

Figure 5.5.: Left: Distribution of the reconstructed transverse impact parameter d0. Most of the events are centered in the first bin and have values smaller than 0.02 cm. Right: Relative tracker isolation in a cone with radius $\Delta R < 0.3$. More than 99 % of the signal is located in the first two bins with values below 0.10.

5.2.2. Isolation

In contrast to a muon produced inside of jets the muon produced by a decaying W′ is isolated, there should be no energy deposits around the muon. So another possible selection criterion to reduce multi-jet background is to use the isolation of the muon. In the early data taking phases isolation criteria based on the calorimeters and the tracker were used and worked fine. Due to the rising instantaneous luminosity there are multiple interactions happening at each bunch crossing so that an originally isolated muon could be overlayed by additional events and become non-isolated. Additionally, due to the high momenta of the muons the probability of radiating bremsstrahlung is high, leading also to non-isolated muons. In order to avoid those effects only tracker-based isolation is used, which is less sensitive to multiple interactions than calorimeter-based isolation. The tracker isolation is defined as the sum of all track momenta in the tracker in a cone with radius $\Delta R = \sqrt{(\Delta\eta)^2 + (\Delta\phi)^2} < 0.3$ around the muon track. To take into account the high muon momentum relative tracker isolation was chosen as selection criterion, relative tracker isolation is defined as:

$$\text{rel.Iso.} = \frac{\sum_{\Delta R<0.3} p_T^{track}}{p_T^{\mu}}. \tag{5.3}$$

The resulting distribution is shown in Figure 5.5 on the right.
A threshold of 10 % is chosen following the recommendation of the $Z' \to \mu\mu$ analysis [74]. More than 99 % of the signal fulfill this threshold even with a high amount of pileup simulated, see Figure 5.5.

5.3. Two-body Decay Kinematics

After ensuring that the reconstructed muons are well reconstructed the next selection steps aim to select the special $W' \to \mu\nu$ kinematics. First of all, there is only one muon in the final state of the signal events. Events containing a second global muon with a p_T greater that 25 GeV besides the first muon with a p_T greater than 40 GeV are vetoed. This eliminates some cosmic muons, which can be reconstructed as two separate ones. As already stated before the W′ decay is a two-body decay, so the two-body decay kinematics are exploited, as it has been done in earlier searches, e.g [75] [76]. In the rest-frame of the W′ the two leptons, which get produced by the decaying W′, have to have the same momentum due to momentum conversation: $|p^{\mu}| = |p^{\nu}|$. The W′ can be produced with a longitudinal boost, so transversal components of the momentum are more interesting, in the W′ restframe the muon and neutrino transverse momentum have to be equal. Because of the vanishing transverse momentum of the colliding particles and the heavy mass of the W′, the W′ should have no transverse boost to lowest order in QCD. This means that in the lab frame the measured transverse momenta of the leptons should be equal: $|p_T^{\mu}| = |p_T^{\nu}|$.

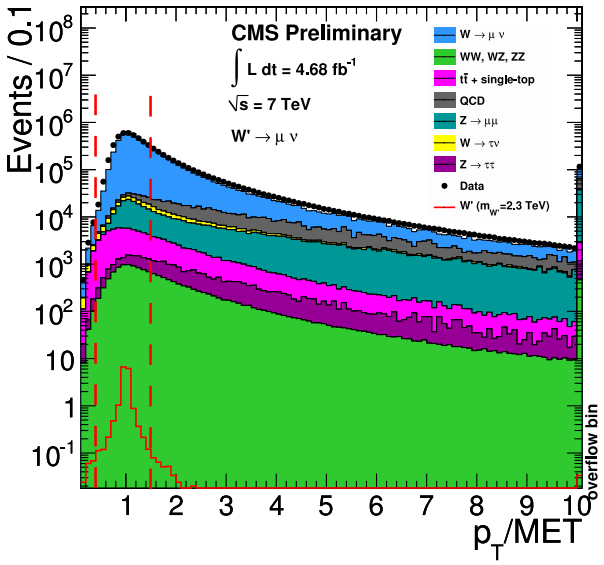

Figure 5.6.: Ratio of the reconstructed transverse momentum of the muon to the reconstructed missing transverse energy. Due to the two-body kinematics the signal peaks at a ratio of 1.

An absolute threshold is hard to define, therefore the previous relation is taken and the ratio of the muon and neutrino momenta is calculated. In Figure 5.6 the distribution of the ratio of the muon transverse momentum to the transverse missing energy representing the momentum of the neutrino is shown. From the consideration for the signal this ratio should be 1. In Figure 5.6 the peak of the signal is at 1 with a very narrow width, the width of the peak is a result of the limited detector resolution. The main background for this analysis, the Standard Model W boson peaks at a value of 1 as well, this is because it has the same two-body kinematics as the signal. Most of the other backgrounds have large tails up to values of 10 and even higher, because they do not

contain real missing energy (neutrinos), which results in a large ratio of muon transverse momentum to missing energy. This ratio allows to separate signal from background. The selection thresholds have been optimized for the best signal to background ratio in Monte-Carlo studies before and have not changed since then, see e.g. [77], so the used range is $0.4 < \frac{p_T}{MET} < 1.5$.

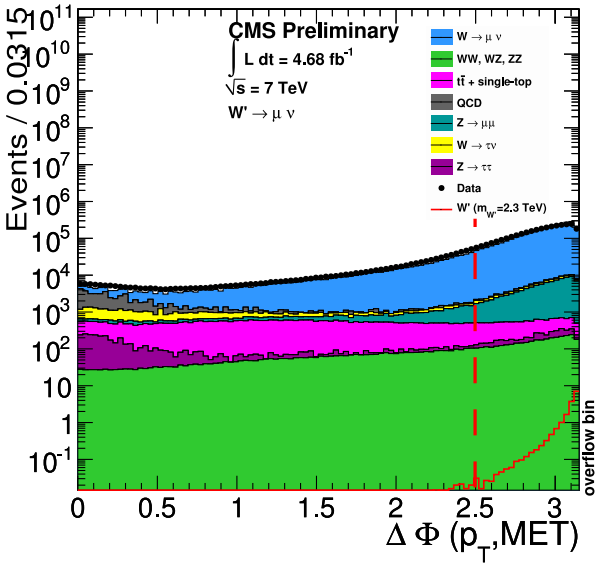

Figure 5.7.: Angle between the muon and the missing transverse energy in the transverse plane, the signal and the Standard Model W boson peak at π.

Due to momentum conversation the two leptons also have to traverse the detector in opposite directions (back-to-back). So the angle ϕ in the transverse plane between the muon and the missing transverse energy is expected to be π. In Figure 5.7 the distribution of the ϕ-angle is shown and as expected the signal peaks close to π with a rather small width. This distribution allows to separate between signal and background once again, and so the angle between the muon and the missing energy is required to be $\Delta\phi(\mathrm{p}_\mathrm{T}^\mu, \mathrm{MET}) > 2.5$. This threshold has been used before [77] and is very loose and does not lower the signal efficiency, but it allows to reduce the some of the backgrounds even further. A higher threshold may reduce the background even further, but this is not needed for this analysis, because in the signal region at high transverse masses the background expectation is already low, so this threshold is kept low to keep the signal efficiency as high as possible.
After applying all selection steps the background events have been suppressed while the signal stays at a very high signal efficiency. The final distribution of the muon transverse momentum and the missing transverse energy are shown in Figure 5.8. The total signal efficiency for on-shell W′ is between 70 % and 80 %, see Table 5.4.
All used quality and analysis selection steps are summarized in Table 5.2 and their impact on the various backgrounds can be seen in Table 5.3 and their impact on the different signal samples is shown in Table 5.4.
After selecting potential W′ candidate events the transverse mass of these events can be calculated following Formula 5.2, but there are some small corrections that should be made before. These corrections are discussed in the following section.

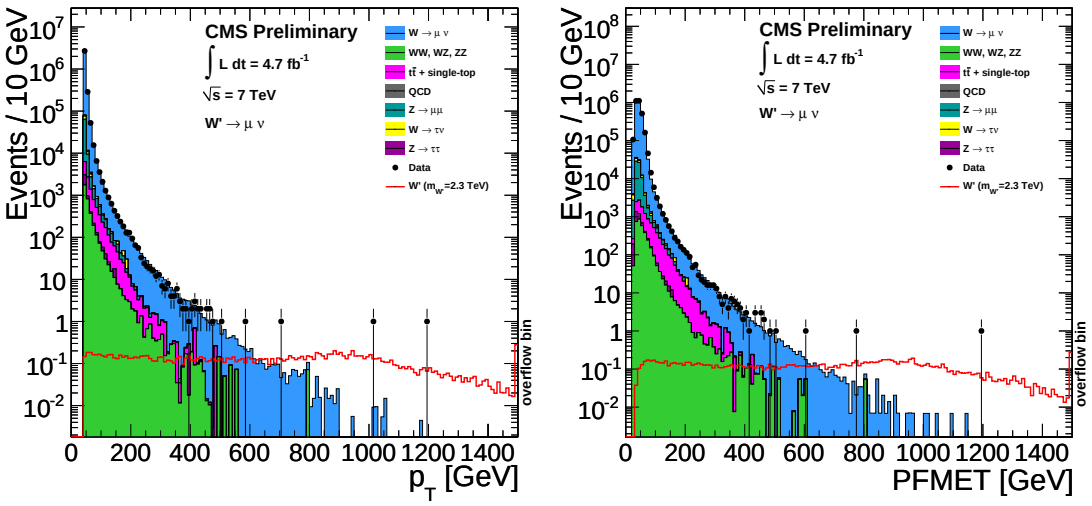

Figure 5.8.: Distributions of the reconstructed transverse momentum of the muon(left) and the Particle Flow missing energy(right) after applying all selection steps.

Discriminating Parameter	Value
Trigger	
Single Muon Trigger	24 - 40 GeV
Acceptance $\lvert\eta\rvert$	< 2.1
Minimum p_T	40 GeV (Cocktail)
Muon Quality Cuts	
Reconstruction	Tacker & Global Muon
Pixel Tracker Hits	≥ 1
Tracker Layers	> 8
Stations in Muon System	≥ 2
Muon Hits on the Global Track	≥ 1
Impact Parameter d0	< 0.02 cm
Relative Tracker Isolation	< 0.1
Good vertex	≥ 1
Analysis Cuts	
Exactly 1 Global Muon with $p_T > 25$ GeV	
$0.4 < \frac{p_T^\mu}{MET} < 1.5$	
$\Delta\phi_{p_T^\mu,MET} > 2.5$	

Table 5.2.: Different quality and analysis selection steps to separate the signal from the background.

Sample	No selection	Acceptance & p_T >40GeV& HLT	Quality Cuts & 1 Global μ	$0.4 < p_T^\mu/MET < 1.5$	$\Delta\phi_{\mu,MET} > 2.5$
$W \to \mu\nu$	$4.89 \cdot 10^7$	$6.33 \cdot 10^6$	$5.56 \cdot 10^6$	$3.59 \cdot 10^6$	$2.93 \cdot 10^6$
	100 %	(13.0 % 13.0 %)	(87.8 % 11.4 %)	(64.6 % 7.3 %)	(81.5 % 6.0 %)
$Z/\gamma^* \to \tau\tau, \mu\mu$	$1.56 \cdot 10^7$	$1.83 \cdot 10^6$	$3.75 \cdot 10^5$	$1.11 \cdot 10^5$	$8.78 \cdot 10^4$
	100 %	(11.7 % 11.7 %)	(20.6 % 2.4 %)	(29.5 % 0.71 %)	(79.4 % 0.56 %)
$W \to \tau + \nu$	$4.89 \cdot 10^7$	$8.77 \cdot 10^4$	$7.61 \cdot 10^4$	$3.50 \cdot 10^4$	$1.22 \cdot 10^4$
	100 %	(0.18 % 0.18 %)	(86.7 % 0.16 %)	(46.0 % 0.07 %)	(34.8 % 0.02 %)
$t\bar{t}$+single-top	$1.14 \cdot 10^6$	$1.07) \cdot 10^5$	$8.18 \cdot 10^4$	$4.20 \cdot 10^4$	7340
	100 %	(9.5 % 9.5 %)	(76.1 % 7.2 %)	(51.4 % 3.7 %)	(17.5 % 0.64 %)
QCD	$3.97 \cdot 10^8$	$4.51 \cdot 10^6$	$3.22 \cdot 10^5$	$(3.93 \pm 0.16) \cdot 10^4$	4230 ± 530
	100 %	(1.1 % 1.1 %)	(7.1 % 0.08 %)	(12.2 % <0.01 %)	(10.8 % <0.01 %)
WW,WZ,ZZ	$2.87 \cdot 10^5$	$2.04 \cdot 10^4$	$1.62 \cdot 10^4$	7540	3220
	100 %	(7.1 % 7.1 %)	(79.4 % 5.6 %)	(46.6 % 2.6 %)	(42.7 % 1.1 %)
All backgrounds	$5.12 \cdot 10^8$	$1.29 \cdot 10^7$	$6.43 \cdot 10^6$	$3.83 \cdot 10^6$	$3.04 \cdot 10^6$
	100 %	(2.5 % 2.5 %)	(49.8 % 1.3 %)	(59.6 % 0.74 %)	(79.4 % 0.59 %)
Data	-	$1.53 \cdot 10^7$	$6.75 \cdot 10^6$	$3.92 \cdot 10^6$	$3.06 \cdot 10^6$

Table 5.3.: The selection efficiencies and the total number of predicted events for the various backgrounds after the different selection steps. The number of expected events for each background is normalized to the integrated luminosity of the CMS experiment in 2011 of $4.68\,\mathrm{fb}^{-1}$. The statistical uncertainty on the QCD background is significant in the last selection steps, therefore it is given together with the expected number of events. The first percentage in each column denotes the efficiency of the corresponding selection step with respect to the previous step, the second one denotes the efficiency for this and the previous steps. In the last row the number of observed data events for the various stages is given.

Sample $M_{W'}$	No selection	Acceptance & p_T >40GeV& HLT	Quality Cuts & 1 Global μ	$0.4 < p_T^\mu/MET < 1.5$	$\Delta\phi_{\mu,MET} > 2.5$
m=0.5 TeV	83000	70400	66100	62600	60400
	100 %	(84.8 % 84.8 %)	(94.0 % 79.6 %)	(94.6 % 75.3 %)	(96.6 % 72.8 %)
m=0.6 TeV	40100	34700	32800	31100	30300
	100 %	(86.6 % 86.6 %)	(94.5 % 81.8 %)	(95.0 % 77.7 %)	(97.3 % 75.6 %)
m=0.7 TeV	21100	18200	17200	16500	16100
	100 %	(85.8 % 85.8 %)	(94.8 % 81.4 %)	(95.7 % 77.9 %)	(97.8 % 76.2 %)
m=0.8 TeV	11800	10300	9830	9400	9220
	100 %	(87.0 % 87.0 %)	(95.7 % 83.3 %)	(95.7 % 79.7 %)	(98.1 % 78.1 %)
m=0.9 TeV	6890	6010	5750	5520	5430
	100 %	(87.2 % 87.2 %)	(95.7 % 83.4 %)	(96.0 % 80.1 %)	(98.4 % 78.8 %)
m=1.0 TeV	4150	3610	3450	3340	3290
	100 %	(87.1 % 87.1 %)	(95.6 % 83.2 %)	(96.7 % 80.5 %)	(98.5 % 79.3 %)
m=1.3 TeV	1040	904	864	838	828
	100 %	(86.9 % 86.9 %)	(95.6 % 83.0 %)	(97.0 % 80.5 %)	(98.8 % 79.6 %)
m=1.4 TeV	675	589	566	547	542
	100 %	(87.3 % 87.3 %)	(96.0 % 83.8 %)	(96.7 % 81.1 %)	(99.0 % 80.3 %)
m=1.5 TeV	444	382	364	353	349
	100 %	(86.0 % 86.0 %)	(95.3 % 82.0 %)	(96.9 % 79.4 %)	(98.9 % 78.6 %)
m=1.6 TeV	297	255	244	237	235
	100 %	(85.9 % 85.9 %)	(95.9 % 82.4 %)	(97.0 % 79.9 %)	(98.9 % 79.1 %)
m=1.7 TeV	198	170	163	157	156
	100 %	(85.8 % 85.8 %)	(95.4 % 81.9 %)	(96.8 % 79.3 %)	(99.0 % 78.5 %)
m=1.8 TeV	134	114	109	105	104
	100 %	(85.2 % 85.2 %)	(95.5 % 81.4 %)	(96.6 % 78.6 %)	(98.9 % 77.8 %)
m=1.9 TeV	90.9	76.3	73.0	70.5	69.9
	100 %	(83.9 % 83.9 %)	(95.7 % 80.3 %)	(96.6 % 77.6 %)	(99.0 % 76.9 %)
m=2.0 TeV	63.0	52.7	50.4	48.7	48.2
	100 %	(83.6 % 83.6 %)	(95.6 % 80.0 %)	(96.5 % 77.2 %)	(99.0 % 76.4 %)
m=2.1 TeV	43.9	36.6	34.9	33.6	33.2
	100 %	(83.3 % 83.3 %)	(95.4 % 79.5 %)	(96.3 % 76.5 %)	(98.7 % 75.5 %)
m=2.3 TeV	22.1	18.0	17.1	16.4	16.1
	100 %	(81.5 % 81.5 %)	(94.9 % 77.4 %)	(95.7 % 74.0 %)	(98.4 % 72.8 %)
m=2.4 TeV	15.9	12.8	12.2	11.7	11.5
	100 %	(80.5 % 80.5 %)	(94.9 % 76.4 %)	(95.9 % 73.3 %)	(98.2 % 72.0 %)
m=2.7 TeV	6.69	5.19	4.91	4.67	4.58
	100 %	(77.7 % 77.7 %)	(94.5 % 73.4 %)	(95.2 % 69.9 %)	(98.1 % 68.5 %)
m=3.0 TeV	3.31	2.48	2.35	2.23	2.18
	100 %	(75.0 % 75.0 %)	(94.8 % 71.1 %)	(94.6 % 67.3 %)	(97.7 % 65.7 %)
m=3.5 TeV	1.38	1.00	0.95	0.89	0.87
	100 %	(72.7 % 72.7 %)	(94.5 % 68.7 %)	(94.1 % 64.6 %)	(96.9 % 62.6 %)
m=4.0 TeV	0.68	0.49	0.46	0.43	0.42
	100 %	(71.3 % 71.3 %)	(94.3 % 67.2 %)	(93.9 % 63.1 %)	(96.9 % 61.1 %)

Table 5.4.: Expected signal events and efficiencies after the different selection steps normalized to 4.68 fb^{-1} of data. The first percentage in each column denotes the efficiency of the corresponding selection step with respect to the previous step, the second one denotes the efficiency for this and the previous steps.

5.4. Corrections to the M_T Spectrum

5.4.1. Pileup Reweighting

During the data taking in 2011 the machine parameters were tuned and optimized to increase the instantaneous luminosity, there is nearly one order of magnitude difference between the beginning and the end of the data taking, see Figure 5.9. With an increase in instantaneous luminosity the probability of multiple interactions per bunch crossing, the so called pileup, increases as well. There are two kinds of pileup: The in-time pileup refers to additional pp collisions in the same bunchcrossing as the interesting primary hard interaction; the out-of-time pileup refers to the events before and after the considered bunchcrossing, which also influence the reconstruction of the event. These pileup events add a lot of additional particles to the event and make the reconstruction much more challenging. Some components of the detector, especially the hadronic calorimeter, have a timing resolution worse than the separation time of 25 ns between two bunches, therefore the reconstruction of an event can be influenced by the bunchcrossings before and after. Besides that these overlayed events change some properties of the reconstructed particles, e.g the isolation of these particles.

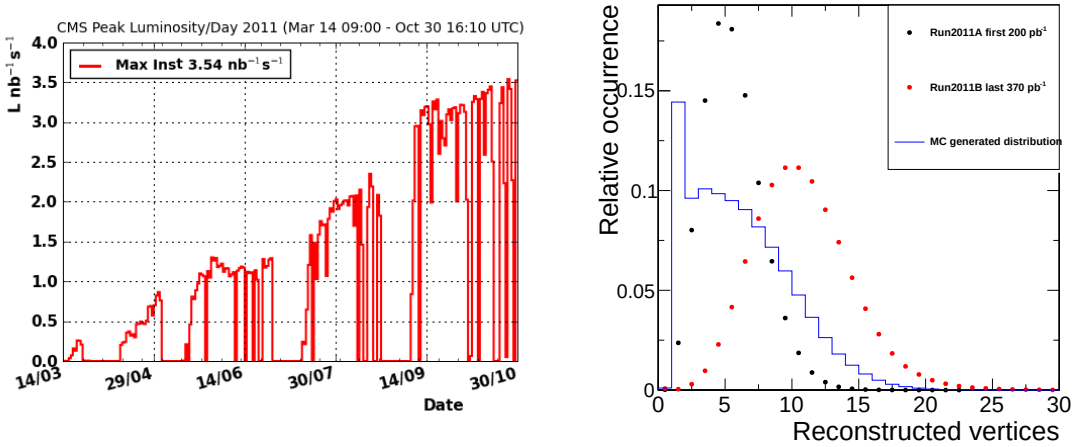

Figure 5.9.: Left: Instantaneous luminosity during 2011 data taking. From reference [58]. Right: Reconstructed number of vertices for the beginning and the end of the 2011 data taking compared to the distribution obtained from one simulated sample of the official Summer11 [60] production.

This pileup, both in-time and out-of-time, was also simulated in the Monte-Carlo samples, but the actual luminosity was unknown when the events were simulated, so the simulated events were generated with a more generic pileup distribution. The number of reconstructed vertices per event is a nice distribution to show the pileup effect, in Figure 5.9 the distribution is shown for very early and very late 2011 data as well as the distribution for the simulated Summer11 [60] Monte-Carlo events. In the early phase of 2011 there was only a low amount of pileup, for the first $200\,\mathrm{pb}^{-1}$ of data shown in Figure 5.9 the average number of reconstructed vertices was around 5. For the first part of this $200\,\mathrm{pb}^{-1}$ the number of pileup is even lower due to the steady increase of the instantaneous luminosity. For the end of the data taking the peak of the distribution of reconstructed vertices got broader and the mean was shifted to above 10 vertices.

Because the simulation of the Monte-Carlo events was done before the data taking was finished, the actual pileup distribution was unknown at the stage of the simulation. Therefore the simulation of the Summer11 production was done with an estimated distribution of pileup events. The events were generated with a flat distribution up to 10 pileup interactions and an exponentially decreasing function for higher values together with an additional part for very low pileup interactions, where only one vertex is reconstructed, see Figure 5.9.
The difference in the simulated and the true distribution could have a big impact on the analysis so in order to avoid this the simulated events are reweighted to match the true distribution. Therefore the so-called 3D-reweighting [78] is applied to reweight the simulated events on an event-by-event basis to match the true distribution. For each simulated event a weight is determined based on three quantities, hence the name 3D: The number of in-time pileup interactions in the considered bunchcrossing n_0 and the number of out-of-time pileup events in the bunchcrossings before and after n_{-1} and n_1. The distribution of these triplets is obtained in data and simulation and then the simulated events get reweighted so the distribution match afterwards. The number of reconstructed vertices for all data and simulated events before reweighting is shown in Figure 5.10 on the left and after the reweighting procedure on the right. After the

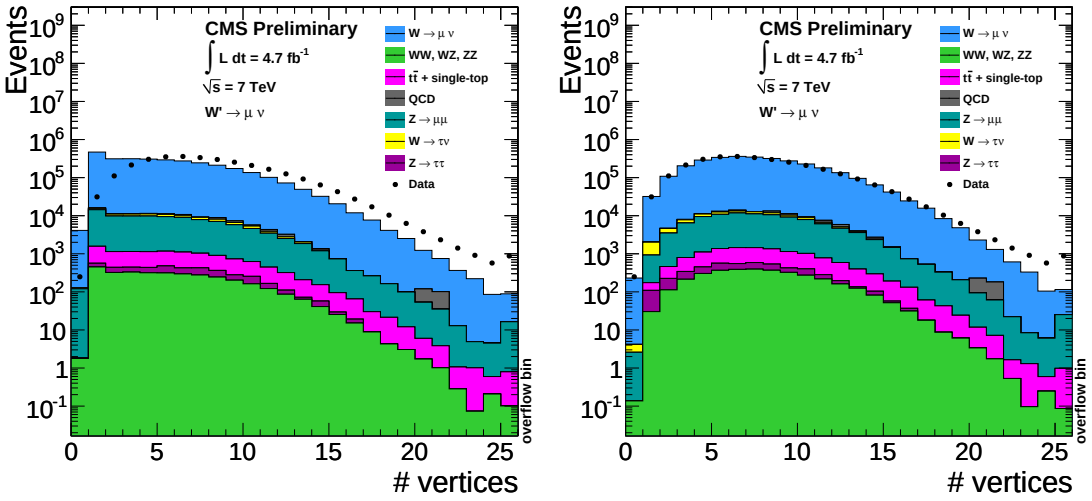

Figure 5.10.: Left: Number of reconstructed vertices without applying any reweighting. Right: Number of reconstructed vertices after applying the 3D-reweighting method, using both in-time and out-of-time pileup. For high numbers of reconstructed vertices there is a small discrepancy visible, this is caused by the low statistics of events with this high number of pileup interactions in the Monte-Carlo simulation.

reweighting the distributions fit nicely for the first part of the distribution but for a very high number of vertices there is a small mismatch due to the very low statistics of these events in the simulated Monte-Carlo events. This behavior is also seen in other analyses, for example in the search for Z' [74].

5.4.2. Hadronic Recoil

Another correction emerges from the hadronic recoil. In the production of vector bosons the bosons can recoil, recoil describes the hadronic activity that balances the transverse momentum of the vector boson. This recoil results in one or more jets together with the vector boson. The model described here is a summary of the method explained in more detail in reference [79]. This hadronic recoil balances the vector boson, so that the vectorial sum of their transverse momentum should be zero:

$$\vec{p}_T^{\,V} + \vec{U}_T = 0, \tag{5.4}$$

with the transverse momentum of the vector-boson $\vec{p}_T^{\,V}$ and the hadronic recoil $\vec{U}_T$. In a real detector the resolution is not perfect so that there is missing energy resulting in an additional part in the equation:

$$\vec{p}_T^{\,V} + \vec{U}_T + \vec{\not{E}}_{\mathrm{T}} = 0, \tag{5.5}$$

with $\vec{\not{E}}_{\mathrm{T}}$ representing the missing transverse energy as a vector, which does not include the neutrinos in the final state. From electroweak analyses it is known that the recoil modeling of the leading-order generator Pythia and the other generators is not in good agreement to the data.
Therefore the hadronic recoil is determined from $pp \to Z \to \mu\mu$ data events, which are comparable from their topology to $pp \to W \to \mu\nu$ events, and then compared to the simulation. The hadronic recoil is split into two components: U_1 parallel to the vector boson and U_2 perpendicular to the vector boson. Binned in vector boson $\mathrm{p_T}$ for each of the two components a mean and a width is determined with the whole 2011 dataset [80]. The pileup reweighting has a big impact on the missing energy in the few GeV region, therefore the hadronic recoil correction is obtained after the reweighting procedure.
The parallel component U_1 shows a stronger dependence on the vector boson $\mathrm{p_T}$ than the perpendicular component U_2, the distributions of the mean and the width for U_1 are shown in Figure 5.11.

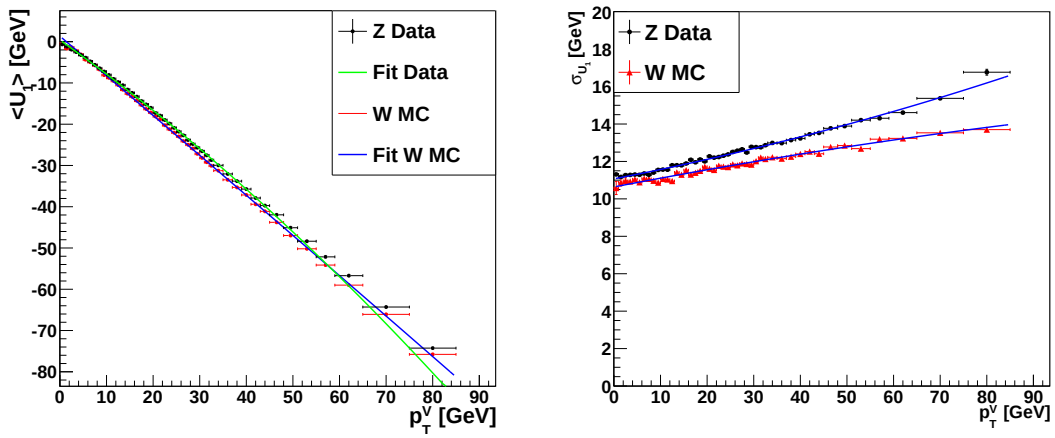

Figure 5.11.: Left: Mean of the parallel component U_1 of the hadronic recoil as a function of the vector boson $\mathrm{p_T}$. From reference [80]. Right: Width of the parallel component U_1 of the hadronic recoil. From reference: [80].

For the $W \to \mu\nu$ sample the missing energy is then recomputed on an event-by-event basis to take the correct mean and width of the hadronic recoil into account.
The impact of the corrections can be nicely seen in the distribution of the ratio of the muon p_T over the missing energy in Figure 5.12. The impact is strongest around the peak at 1 and with the corrections the agreement is much better, however at higher values there is still some disagreement due to the normalization of the QCD events.

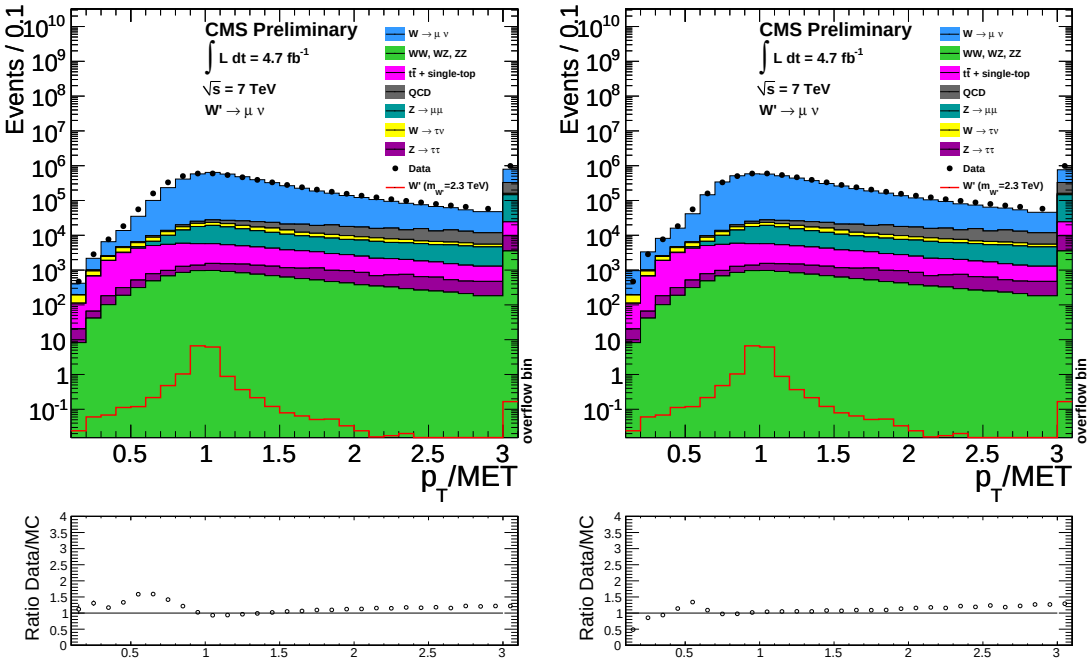

Figure 5.12.: Left: p_T over MET ratio without hadronic recoil correction, a clear discrepancy is visible around values of 1. Right: p_T over MET ratio after applying the hadronic recoil correction yields much better agreement.

However the impact on the analysis is rather negligible. This can be seen in the Figures 5.13 and 5.14 where the transverse mass, see Formula 5.2, has been calculated with and without the hadronic recoil correction.
The hadronic recoil correction only affects the lower part of the distribution, especially around the Standard Model W peak, but leaves the tail of the distribution unaffected.

5.5. Cosmic contribution

As already mentioned at the signal selection steps, the selection threshold on the transverse impact parameter d0 can be used to get an estimate of a possible cosmic contribution. A cosmic muon penetrating the detector close to the beamspot can be reconstructed as two muons emerging from one vertex, one moving upwards, the other one moving downwards. The timing for one of the muons is reversed because it moves from the top of the detector to the center instead of both muons coming from the center, so sometimes only one of the muons gets reconstructed. These events are similar to the $W' \to \mu\nu$ signature, because the not reconstructed leg of the cosmic muon would result into missing energy.

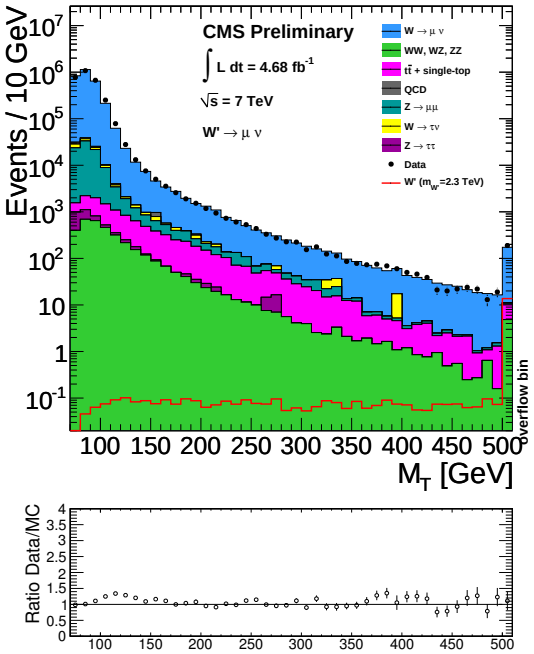

Figure 5.13.: Zoom on the transverse mass distribution in the range of 70 to 500 without applying the hadronic recoil corrections.

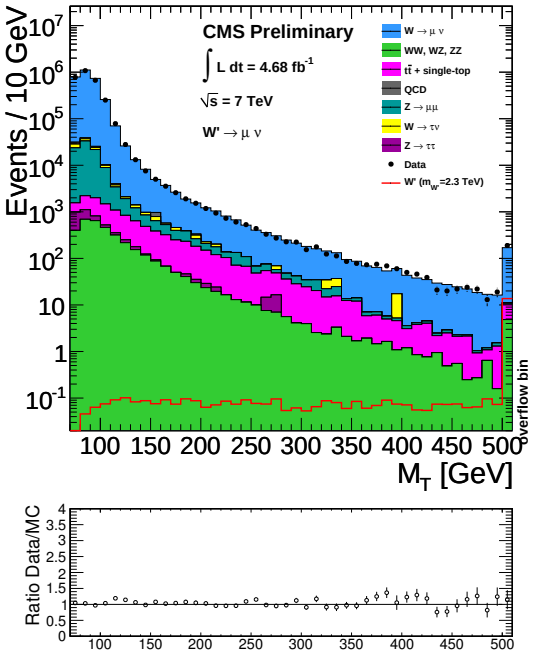

Figure 5.14.: Zoom on the transverse mass distribution in the range of 70 to 500 GeV with applying the hadronic recoil correction.

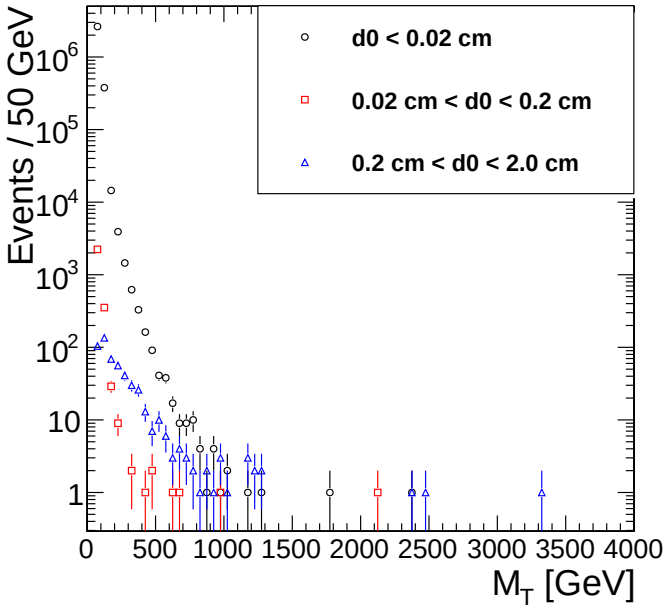

Figure 5.15.: Transverse mass distribution for various ranges of the transverse impact parameter d0. Events with d0 $< 0.02\,\text{cm}$ fulfill the selection criteria, the events with $0.2\,\text{cm} <$ d0 $< 2.0\,\text{cm}$ are likely produced by cosmic muons.

The d0 threshold used in this analysis is $|d0| < 0.02\,\text{cm}$, which is a very tight value compared to the threshold of 0.20 cm used in other analyses. The distribution of cosmic muons would be flat in d0, because they are independent of the collisions. The transverse mass distribution for various ranges of d0 can be seen in Figure 5.15. The black points represent the collision events which are used in this analysis and fulfill $|d0| < 0.02\,\text{cm}$, the red points represent the events from an intermediate range of $0.02\,\text{cm} < |d0| < 0.20\,\text{cm}$, which could be from collisions but also from cosmics and the blue points represent events with $0.2\,\text{cm} < |d0| < 2.0\,\text{cm}$, which are considered to stem from cosmic muons. The M_T distribution of the events with a very large transverse impact parameter is flatter than the other two distributions and the peak at lower masses is not as pronounced as for the other two ranges.
Assuming that cosmic muons are distributed equally over the whole d0 range, a possible contribution of cosmic muons in the signal region $|d0| < 0.02\,\text{cm}$ can be estimated from the events in the largest range $0.2\,\text{cm} < |d0| < 2.0\,\text{cm}$ by taking the ratio of the covered ranges in d0 into account. The possible cosmic events cover a range of $2 \cdot (2.0\,\text{cm} - 0.2\,\text{cm}) = 3.6\,\text{cm}$ while the events considered in this analysis cover $2 \cdot 0.02\,\text{cm} = 0.04\,\text{cm}$ which is 90 times smaller. The contamination of cosmic muon contribution can then be calculated by taking the number of the observed events in the largest d0 range and dividing it by this ratio of the ranges.
The result can be seen in Table 5.5 as a function of the transverse mass. The expected cosmic contribution is quite small, e.g. only a small fraction of an event in the interesting region, and will be neglected in the further analysis.

M_T Range	Number of data events after all selection steps	Estimated number of cosmic events
300 - 600 GeV	6670 ± 80	2.13 ± 0.15
> 400 GeV	393 ± 20	0.73 ± 0.09
> 600 GeV	62.0 ± 7.9	0.33 ± 0.06
> 800 GeV	16.0 ± 4.0	0.20 ± 0.05
> 1000 GeV	6.0 ± 2.5	0.12 ± 0.04
> 1200 GeV	3.0 ± 1.7	0.08 ± 0.03
> 1400 GeV	2.0 ± 1.4	0.03 ± 0.02
> 1600 GeV	2.0 ± 1.4	0.03 ± 0.02
> 1800 GeV	1.0 ± 1.0	0.03 ± 0.02
> 2000 GeV	1.0 ± 1.0	0.03 ± 0.02

Table 5.5.: Cosmic contribution estimate from a variation of the threshold on the transverse impact parameter d0.

5.6. The Final M_T -distribution

As already pointed out in the beginning of this chapter the most interesting distribution is the transverse mass distribution. In the two years of data taking at $\sqrt{s} = 7\,\text{TeV}$ there were different phases of the analysis when it went public. A brief summary of the analysis in these phases is presented here in order to show these important milestones. The evolution of the transverse mass distribution with the amount of recorded data shows

some nice features in these various steps and especially the amount of events at high transverse masses is interesting for this analysis.

5.6.1. CMS 2010 Data

At the end of 2010 the first CMS publications of the W′ searches were published in PLB with the whole 2010 dataset of 36 pb^{-1} in the electron channel [81] and the muon channel [82]. The results of the muon channel are based on this analysis, the selection criteria are basically the same as presented before with just slight variations regarding the isolation and quality selection of the muon. The missing energy performance worked extremely well despite the very early stage of data taking, so the kinematic selection steps remained the same from there.
The final transverse mass distribution after all selection steps for the 2010 data together with the Monte-Carlo simulations for the backgrounds and two potential W′ signals with masses of 1 TeV and 1.4 TeV is shown in Figure 5.16. There is a good agreement between data and Monte-Carlo and the event with the highest transverse mass has M_T = 500 GeV.

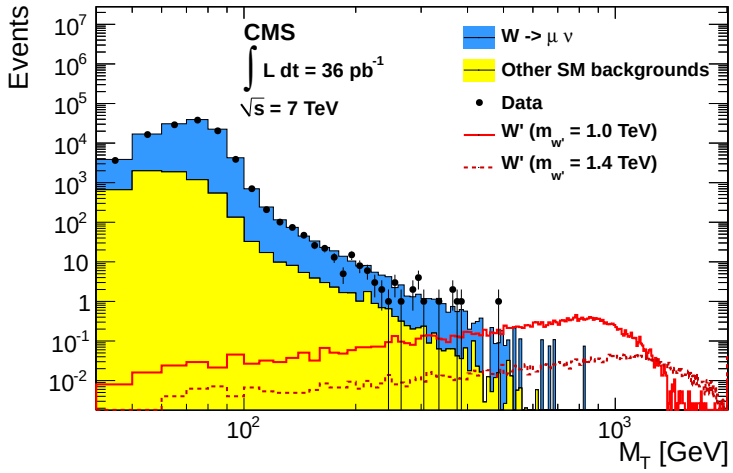

Figure 5.16.: Transverse mass distribution with the whole data recorded in 2010, published in PLB [82].

5.6.2. Dataset for the EPS Conference

In Figure 5.17 on the left the transverse mass distribution of the first 1.1 fb^{-1} of 2011 data together with a W′ with a mass of 1.5 TeV is shown. The analysis was made public [83] with this dataset for the EPS conference. The data corresponds to about 30 times more than the whole 2010 dataset and the highest events have transverse masses of slightly below 800 GeV. In Figure 5.17 on the right the cumulative distribution is shown, where the good data to simulation agreement is visible for the first part of the distribution up to 700 GeV. After that the data drops and at transverse masses above 800 GeV there are no more data events with about 4.5 events expected from the Monte-Carlo simulation. This slight deficit can occur in about 1 % by statistical fluctuation

and is therefore statistically not significant.

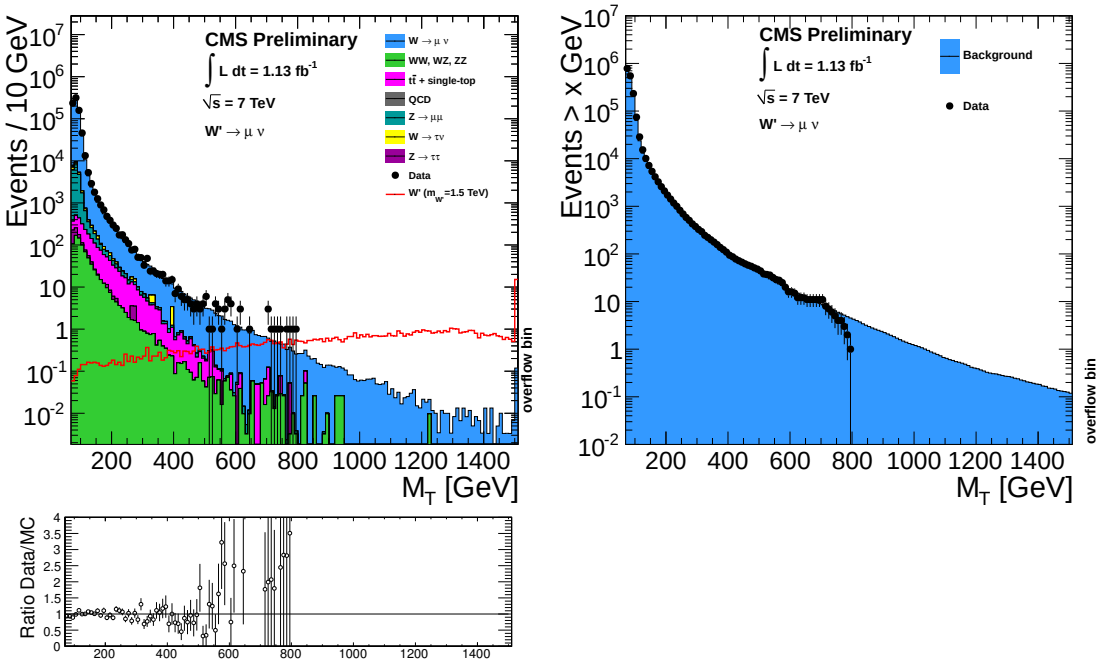

Figure 5.17.: Left: Transverse mass distribution with the first 1.1 fb^{-1} of 2011 data. Right: Cumulative transverse mass distribution with the first 1.1 fb^{-1} of 2011 data.

5.6.3. Full 2011 Dataset

The whole 2011 dataset of 2011 corresponds to an integrated luminosity of 4.68 fb^{-1}, this is about 4 times more integrated luminosity compared to the results shown at the EPS conference. The results based on this dataset will be published soon in the journal JHEP. The transverse mass distribution with the whole 2011 dataset is shown in Figure 5.18 on the left together with a signal sample with a mass of 2.3 TeV, the cumulative distribution is shown on the right. In the cumulative distribution the good consistency between the Monte-Carlo expectation and the CMS data is visible with now several events exceeding the 1 TeV transverse mass region, even one in the very end of the distribution with a transverse mass of 2.4 TeV. The event displays of the four events with the highest transverse mass are shown in Appendix B.1. Above 1 TeV there is a slight excess in the data mostly caused by this one event.

In the plots for the different stages of the analysis different signal samples are plotted showing the worsening of the resolution with higher muon momenta. In the left plot on Figure 5.18 the signal of a W′ with a mass of 2.3 TeV is nearly flat and no Jacobian Peak is visible.

The data of 2011 is consistent with the Standard-Model-only expectation over the whole transverse mass distribution and no excess in the high M_T region, where a potential signal would be most visible, was observed, therefore a statistical analysis can be performed in order to set an exclusion limit on a possible W′ contribution.

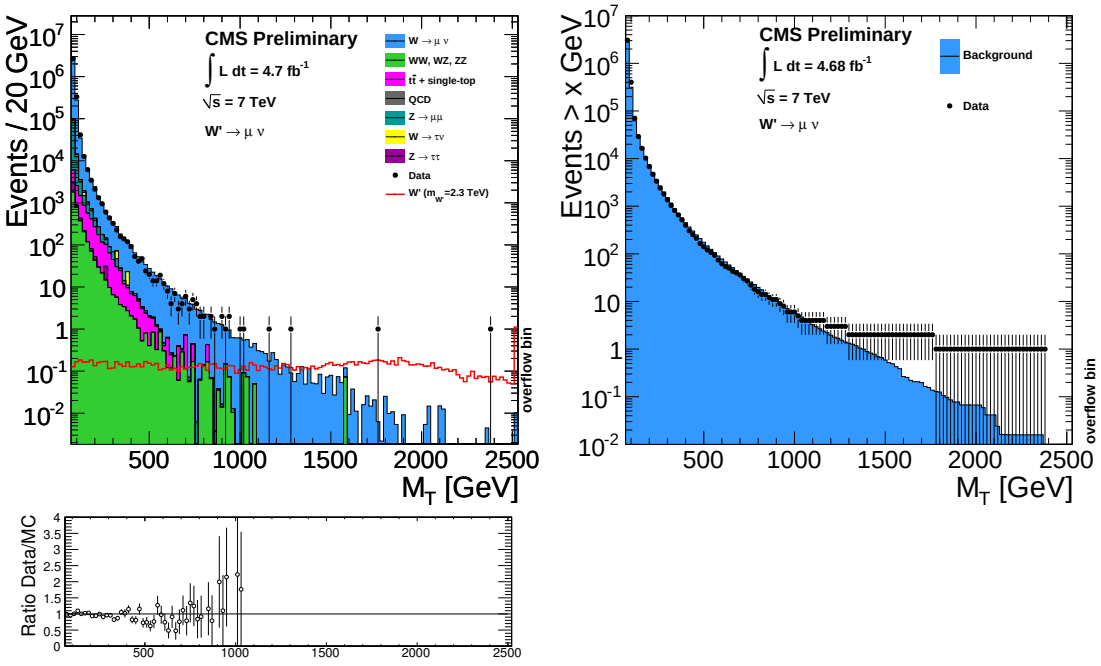

Figure 5.18.: Left: Transverse mass distribution with the full 2011 dataset corresponding to 4.68 fb^{-1}. Right: Cumulative transverse mass distribution of the full 2011 dataset.

5.7. Efficiencies

In the analysis there are several requirements, which may have different efficiencies in data and Monte-Carlo simulation. To account for this discrepancy correction factors have to be determined and then applied to the simulation to get the correct number of expected events. For this analysis four efficiencies are important:

- ϵ_{Reco}: The reconstruction efficiency for muons.
- ϵ_{ID}: The muon identification efficiency. The efficiency of a muon fulfilling the quality criteria with exception of the isolation criterion. This is often called the offline selection.
- $\epsilon_{Isolation}$: The efficiency of a muon fulfilling the isolation criterion.
- $\epsilon_{Trigger}$: The efficiency that the muon has triggered one of the considered single-muon triggers.

The final muon analysis efficiency is then the product of all the four partial efficiencies $\epsilon_{muon} = \epsilon_{Reco} \cdot \epsilon_{ID} \cdot \epsilon_{Isolation} \cdot \epsilon_{trigger}$. The last three are calculated by the "Tag & Probe method", which is described in more detail in the references [84, 85], and will only be briefly explained here.
The Tag & Probe method uses the decay $Z \to \mu\mu$, where two "good" muons are produced with an invariant mass around 90 GeV. At this invariant mass there is very little background. For the method events with two muon candidates with an invariant mass around the Z-mass in a window between 60 and 120 GeV are selected. One of the muons,

the so called "Tag"-muon has to be triggered and fulfill the criteria described in Section 5.2, the second muon, the so-called "Probe", is then checked for one of the criteria under study, and can either pass this criterion or fail it. The efficiency of the criterion under study is then obtained by the ratio of the passing events to the total number of events.

The tag muon definition is the same for all efficiencies, the tag muon has to been triggered by one of the single muon High-Level-Triggers (HLTs), it has to be isolated and fulfill the muon quality criteria described in Section 5.2. The muon criteria for qualifying a muon to be a probe muon are different in the several steps, for the muon ID efficiency every tracker & global muon with a p_T greater than 40 GeV is sufficient, for the isolation efficiency the probe muons have to fulfill the ID requirements in addition to the previous criteria and for the trigger efficiency the probe muon has to be also isolated.

For each di-muon event the invariant mass of the two muons is calculated. Afterwards several invariant mass distributions are produced depending on the properties of the events: The events are filled into different invariant mass distributions depending on the p_T and η of the probe muon, also there are different distributions for events in which the probe muon passes the criterion under study and for events in which the probe muon fails it.
Each of these invariant mass distributions is then fitted by a combination of a Breit-Wigner, a Crystal-Ball and an exponential function [85]. The Breit-Wigner represents the actual invariant mass shape of the $Z \rightarrow \mu\mu$ events, the Crystal-Ball functions is needed to account for radiative corrections and the exponential function describes the potential background. The potential background represented by the exponential function has to be subtracted in order to get the efficiency.
For each range of the muon p_T and η the number of passing $N_{\text{probes,passing}}$ and failing $N_{\text{probes,failing}}$ events can be obtained by integrating the fitted Breit-Wigner and Crystal-Ball function. The efficiency is then calculated by

$$\epsilon = \frac{N_{\text{probes,passing}}}{N_{\text{probes,passing}} + N_{\text{probes,failing}}}. \tag{5.6}$$

It is derived separately in the barrel and the endcap region as well as for various ranges of the muon transverse momentum. The efficiencies are rather independent on the muon p_T, therefore a fit above the required p_T threshold of 40 GeV is performed to get the final efficiencies. Afterwards for each criterion a scaling factor f can be defined as the ratio of the efficiency in the data to the efficiency in the Monte-Carlo simulation:

$$f = \frac{\epsilon_{\text{data}}}{\epsilon_{\text{MC}}}. \tag{5.7}$$

Then this scaling factor has to be applied to the number of expected events in the simulation to account for different efficiencies in data and simulation.
The results for both simulation and data are provided by [86]. The results can be seen in Table 5.6 for all used triggers as well as for the offline selection and the isolation criterion, the shown uncertainties correspond to the statistical uncertainty. Two example plots are shown in Figure 5.19. The numbers in the names of the High-Level-Triggers indicate the minimal p_T threshold, e.g. the HLT Mu24 trigger has a minimal p_T threshold of 24 GeV, the last trigger (HLT Mu-40-eta2p1) also has a restriction on the range of the

pseudorapidity of $|\eta|$ 2.1. In the Monte-Carlo events only two triggers are simulated, which have the same efficiency of about 93 %, therefore this value is also used for the calculation of the scaling factors for the other two triggers in data.

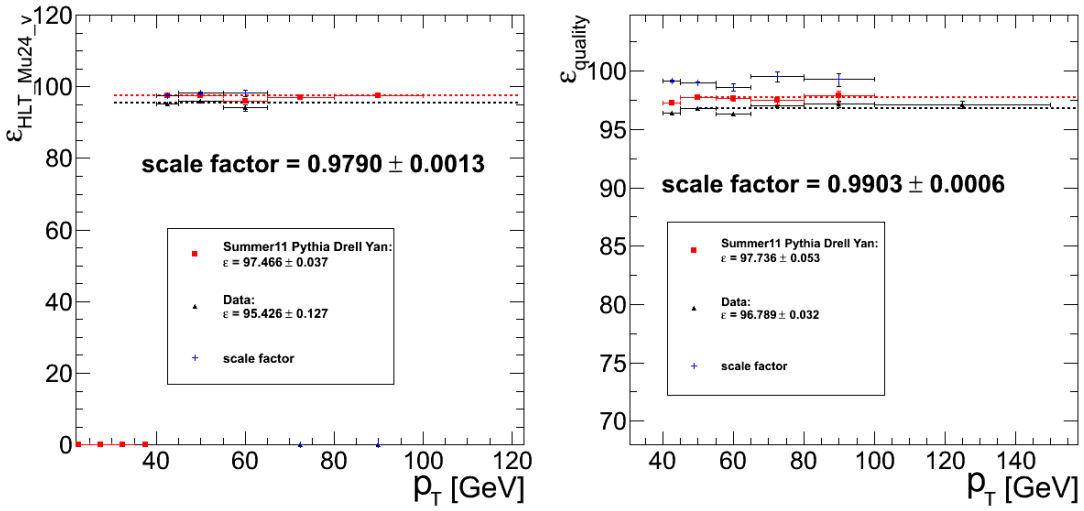

Figure 5.19.: Left: Trigger efficiency of the single muon High-Level-Trigger HLT_Mu-24, which has a minimal muon p_T threshold of 24 GeV, in the barrel as a function of the muon p_T, the scale factor is defined as the ratio of the efficiency in data to the efficiency in simulation. Right: Efficiency of the muon quality criterion in the barrel as a function of the muon p_T, from reference [86].

	Barrel		Scaling factor	Endcap		Scaling factor
	Data [%]	Simulation [%]	$\epsilon_{Data}/\epsilon_{MC}$	Data [%]	Simulation [%]	$\epsilon_{Data}/\epsilon_{MC}$
Muon offline sel.	96.79 ± 0.03	97.74 ± 0.05	0.990 ± 0.001	91.87 ± 0.04	92.69 ± 0.08	0.991 ± 0.001
Rel. Tracker Iso.	99.37 ± 0.01	99.57 ± 0.02	0.9979 ± 0.0001	99.54 ± 0.01	99.63 ± 0.02	0.9991 ± 0.0002
Trigger						
HLT Mu-24	95.43 ± 0.13	97.47 ± 0.04	0.979 ± 0.001	91.75 ± 0.23	93.09 ± 0.09	0.986 ± 0.003
HLT Mu-30	95.83 ± 0.04	97.46 ± 0.04	0.983 ± 0.001	94.19 ± 0.06	93.08 ± 0.08	1.012 ± 0.001
HLT Mu-40	95.21 ± 0.06	not in MC	0.993 ± 0.001	92.35 ± 0.10	not in MC	0.977 ± 0.001
HLT Mu-40-eta2p1	97.00 ± 0.04	not in MC	0.995 ± 0.001	94.47 ± 0.07	not in MC	1.018 ± 0.001

Table 5.6.: Trigger and offline selection efficiencies in percent separately for data and simulation in both the barrel and the endcaps, the shown uncertainties are the statistical uncertainties only. The numbers in the trigger names indicate the minimal p_T thresholds of the triggers. Provided by [86].

There is a good agreement between the simulated efficiencies and the efficiencies obtained from data, nevertheless a small correction factor can be derived and then applied to data. The reconstruction efficiency was not calculated in this analysis, but for Run 2011A it was in good agreement between simulation and data. For Run 2011B however, a efficiency drop of 4% in the endcaps was reported [87]. Taking this drop into account an overall correction factor can be derived, which is independent of the muon p_T or the pseudorapidity η. This overall factor is calculated by weighting the efficiency over the

whole η range according to η distribution of the data and by weighting the different trigger efficiencies according to the fraction of data in which the according trigger was active. This overall correction factor is about 0.974 ± 0.001 [86] and has to be applied to the simulated samples in order to get the right number of expected events.
The CMS muon trigger system is only instrumented up to a pseudorapidity of $|\eta| < 2.1$. Therefore all the efficiencies so far are only evaluated in this acceptance region of $|\eta| < 2.1$. However, it is nice to see the geometrical acceptance, which is defined as the fraction of events inside the pseudorapidity range of $|\eta| < 2.1$ with respect the total number of events N_{total}:

$$A = \frac{N(|\eta| < 2.1)}{N_{total}}. \tag{5.8}$$

For the various signal samples this acceptance is shown in Figure 5.20 together with the efficiency after requiring the trigger and the minimal p_T of 40 GeV, this is called "precut" in the plot. For comparison also the efficiency of the $W \to \mu\nu$ samples is shown after all these requirements.

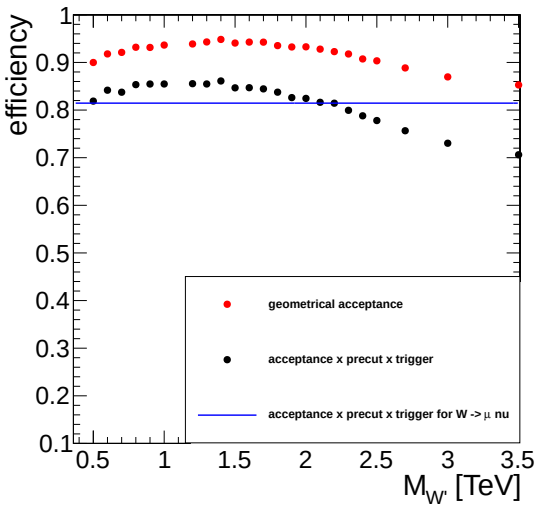

Figure 5.20.: The red circles show the geometrical acceptance as a function of the W′ mass. The geometrical acceptance is defined as the fraction of the events with a pseudorapidity $|\eta| < 2.1$ with respect to all events. The blue circles show the efficiency after applying the acceptance, the $p_T > 40$ GeV and the trigger requirement and the blue line shows the corresponding efficiency for the SM W sample.

The acceptance for intermediate masses of the W′ is between 92 % and 95 %, for very light W′ it is slightly lower because the W′ can be produced with a boost and therefore the decaying particles have a higher probability to be produced in the forward direction and leave the acceptance. For very heavy W′ the acceptance drops even further down to 85 % because the rate of off-shell produced W′ increases with the mass and hence most of the W′ are produced far below their on-shell mass and can again be boosted in the forward direction.
The overall efficiency for the different W′ samples can be seen in Table 5.4.

5.8. Systematic Uncertainties

The different properties of the event that are used in this analysis are only known with a limited precision. Systematic shifts in these quantities result in slightly different transverse mass distributions. The systematic uncertainties can result in a shift of the normalization of the whole distribution, e.g. if the luminosity estimate differs from the true value, as well as in a smearing of the distribution, e.g. if the assumed muon p_T resolution is worse than simulated. Before a statistical analysis can be performed the influence of these systematic uncertainties has to be estimated.
The muon selection and identification are basically unchanged since 2010 and the muon performance follows the publication of the CMS paper MUO-10-004 [41]. The uncertainty of the other important physics object in this analysis, the Particle Flow missing energy, is computed following the MET group recommendations as described in [88]. In the following the considered systematic uncertainties are described in more detail:

- The luminosity measurement [89] has been improved several times after the data taking. The currently recommended uncertainty on the measurement is 4.5 % [49], a systematic shift of the luminosity results in a shift of the normalization of the expected backgrounds.

- The most important physics object in this analysis is the high-p_T muon. For this analysis the Cocktail muon reconstruction algorithm optimized for high-p_T muons is used. Nevertheless there could be systematic differences between simulation and data in the muon momentum scale and the muon momentum resolution. From detailed studies of $Z \to \mu\mu$ a scale shift in the reconstruction of the muon momentum of more than 0.4 % can be excluded at the level of one standard deviation [41]. Alignment studies using muons with around 1 TeV momentum show that this upper limit on the scale shift is also valid in the high momentum region. This value is also used for this study.
  Besides the absolute scale of the muon momentum the momentum resolution could be different in the simulation. Due to the very straight track of the high-p_T muons an uncertainty of 10 % on the transverse momentum resolution is assumed over the whole range of transverse momenta. This is motivated by the muon momentum resolution of the Cocktail algorithm, which is about 10 % for 1 TeV muons, see Figure 3.1.
  In order to estimate the effect of these uncertainties an additional smearing of the reconstructed muon momentum is performed and the differences in the transverse mass distribution are taken as systematic uncertainty. This is done by scaling the muon momentum by 0.4 % and by smearing the x and y component of the muon momentum by 10 %. The missing energy then has to be recomputed taking into account the difference to the original muon momentum. With these new values a new transverse mass can be calculated. The obtained transverse mass distribution is slightly smeared in comparison to the original transverse mass distribution. These uncertainties have no big impact on the selection steps, because the muon p_T and missing energy are affected in the same way and only relative selection criteria are applied.

- For the missing energy the recommendation [88] by the JETMet group is followed. To all physics objects entering the missing energy calculation, their specific uncertainties should be applied. Besides the muons, which are already considered, the

other uncertainties seem to have a negligible effect. In addition there is a 10 % uncertainty on the scale and the resolution of the unclustered energy. Unclustered energy describes jets with a transverse momentum below 10 GeV together with all the tracks that are not associated to jets or other objects. The x and y component of this unclustered energy are getting scaled and smeared and a smeared transverse mass distribution is obtained.

- As described in Section 5.7 there are some differences in the trigger, reconstruction and isolation efficiencies between simulation and data, see Table 5.6. The uncertainty of the scaling factors are taken as a systematic uncertainty, but due to the small error on the scale factors the impact is negligible.

- The simulated events get reweighted by using the 3D reweighting prescription [78]. This method is based on the estimated number of interactions, which is calculated using the total proton-proton cross section [90]. The uncertainty on this cross section has to be taken into account resulting in a shift of the pileup interactions by 8 % [91] which results in different weights for each of the events.

- Later on the smeared transverse mass distributions are used for fitting purposes, see Section 6.3, the uncertainty on the fits are also taken as systematic uncertainty.

- Another uncertainty arises due to the uncertainty of the parton distribution functions, therefore the PDF4LHC recommendations, see Section 4.4.2, are followed, which produce a different weight for each event.

The smeared transverse mass distributions resulting from these uncertainties for the sum of all the considered SM background process are shown in Figure 5.21. Because the difference to the original distribution is hardly visible on a logarithmic scale, also the ratio of the smeared distribution to the original distribution can be seen in Figure 5.21. The muon momentum scale shifts have a negligible impact on the transverse mass distribution due to the low systematic uncertainty on the scale. For the uncertainty on the momentum resolution a much higher value of 10 % is assumed and the impact on the transverse mass distribution is higher. There are mostly bin-to-bin migrations, where some of the events in the peak around 100 GeV are pushed into the high transverse mass tail of the distribution and a slight increase in the tail can be observed.
For the uncertainties on the MET resolution and MET scale the effect is reversed. The uncertainty on the MET resolution has a smaller impact on the transverse mass distribution than the uncertainty of scale shifts. A shift of 10 % produces large deviations from the original distribution, mostly because due to the change in the missing energy less events pass the kinematic selection. In the second ratio plot in Figure 5.21 it is visible, that these MET shifts result in an offset of the transverse mass distribution. Later on the MC expectation is scaled to the data, so that these offsets will not have a big impact on the analysis.
The smearing due to the uncertainty on the number of pileup events is negligible compared to the other sources of systematic uncertainties.
Taking this uncertainties the next step is to get a better description of the background in the very high region of the transverse mass, where a potential W' would produce most of its events.

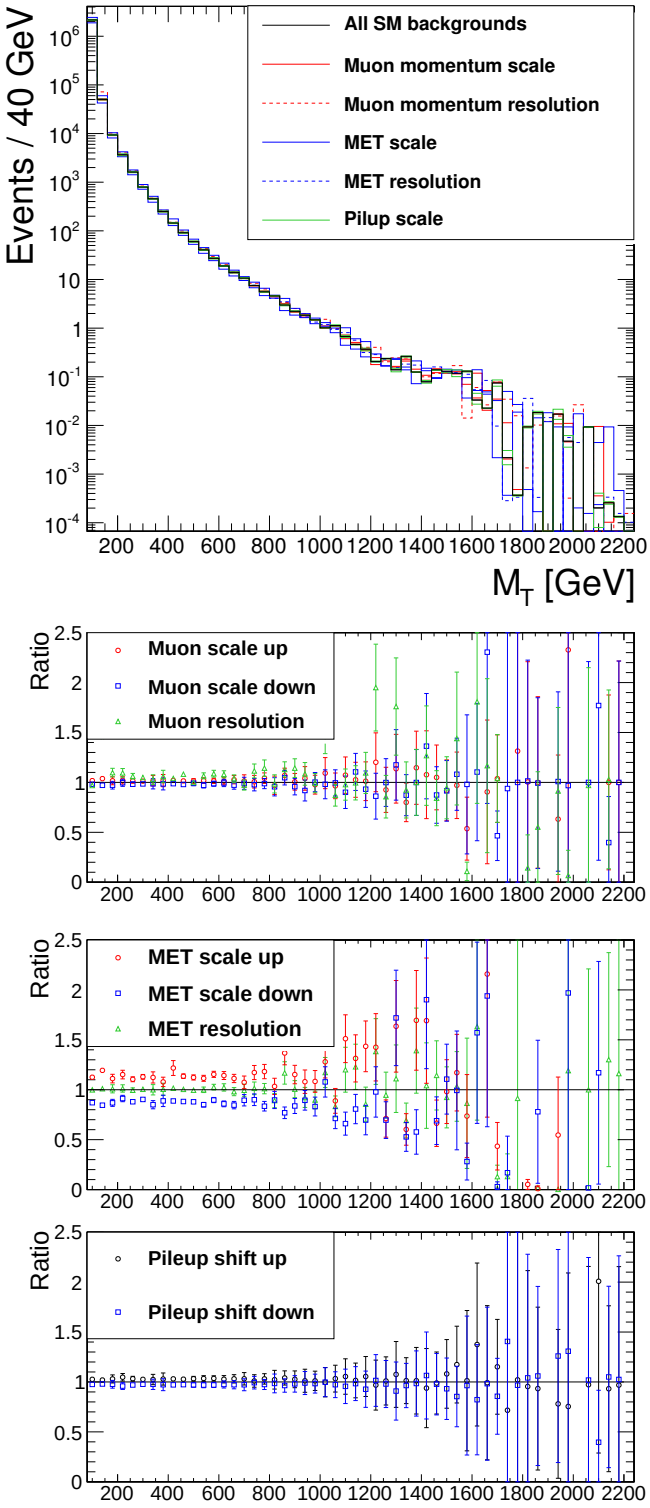

Figure 5.21.: Smeared transverse mass distributions for the sum of all simulated SM background samples obtained by scaling and smearing of the object properties according to their systematic uncertainties. The lower plots give the ratio to the original transverse mass distribution.

6. Background Determination

In the previous section the good agreement between the Monte-Carlo expectation of the Standard Model and the observed data was shown. A potential W′ signal would be most visible in the very end of the transverse mass distribution on top of the steeply falling spectrum of the Standard Model W boson, see Figure 5.2. Searching for this excess at very high transverse masses requires an accurate background determination, for this analysis this is in particular the background from the SM W boson.
Two different methods have been developed: A fully data driven method using no Monte-Carlo information, the so-called Sideband fit, and a Monte-Carlo based method using the whole transverse mass spectrum. These two methods will now be discussed with their advantages and disadvantages.

6.1. Data Driven Sideband Fit

This method is used in several other analyses, which deal with a steeply falling spectrum, e.g. the Exotica black hole analysis EXO-11-021 [92], and it was adapted for this analysis. The underlying principle is a fit to the low M_T sideband region in data and a subsequent extrapolation to higher transverse masses. The reason behind this is to be less dependent on the different Monte-Carlo generators, which produce only LO samples. Also in the early data taking such a good agreement between the simulation and the data was not granted, therefore a more data-driven approach was needed.
In 2010 with an integrated luminosity of 36 pb^{-1} the event with the highest transverse mass had $M_T = 500\,GeV$. The sideband region was defined as $M_T = 180\text{-}350\,GeV$ and the expected background was then defined by fitting a relativistic Breit-Wigner in this sideband region and extrapolating it into the signal region $> 500\,GeV$. The expectation from the extrapolation was in agreement with the Monte-Carlo expectation.
The relativistic Breit-Wigner was motivated from the shape of the SM W boson, but with more statistics it showed, that it is not capable of modeling the background in the high mass region any longer. The Breit-Wigner was not in agreement with the Standard Model expectation, it was overestimating the number of events in the tail of the distribution, which can be seen later in Figure 6.1. Therefore another approach was needed for the dataset of the EPS conference, where events up to 800 GeV were observed. As in the black hole analysis [92] three empirical motivated functions are chosen to model the steeply falling spectrum:

Function 1:

$$\frac{a}{(M_T + b)^c} \tag{6.1}$$

Function 2:

$$\frac{a}{(M_T^2 + b \cdot M_T + c)^d} \tag{6.2}$$

Function 3:

$$\frac{a(1+M_T)^b}{(M_T^{c+d\cdot\log x})} \tag{6.3}$$

When applied to the simulation all three functions show a very good performance in modeling the shape. However, to obtain a more data-driven estimate the three functions are fitted to the sideband of the transverse mass spectrum obtained from data and extrapolated into the signal region to get an estimate of the expected background in this region.
There are some important things missing in order to model the shape of the background on a theoretical basis, for example a parameterization of the muon momentum resolution or higher order corrections, which influence the shape. So these non-theoretical motivated functions, which are capable of dealing with the steeply falling spectrum, are chosen.
For 2011 the sideband is extended to 200-600 GeV, this extension is possible, because with the 2010 data a W′ with masses below 1.4 TeV could be excluded [82], hence no significant signal contribution is expected below 600 GeV.
For each of the three functions the lower bound of the sideband was varied between 190-210 GeV and the upper end between 550 and 650 GeV. The variation of the lower bound has a stronger influence on the fit result than the variation of the upper bound, this can be explained by the steeply falling spectrum. Beside the different fit ranges for the functions also the binning of the transverse mass distribution was varied between 10 and 20 GeV, but this different binning has a negligible impact on the result.
The spread of the extrapolations of the different functions as well as their variations due to the change in the sideband range are taken as systematic uncertainties.

In Figure 6.1 the fit functions for various sideband ranges are shown with the whole 2011 dataset of 4.68 fb^{-1}, the functions are indicated by different colors. The fits are performed on the data spectrum, the MC is just shown for visual comparison of the fit and the expectation. A good agreement between the different fits and the expectation from simulation is visible. Nevertheless a small discrepancy between the fits is existing, so the mean of all functions is taken as the expected background and the difference between the highest and the lowest function, the so-called spread, is used as a systematic uncertainty, see Figure 6.2. Also the relativistic Breit-Wigner is shown for comparison; it overestimates the Standard Model background by around one order of magnitude, which was not visible with the lower statistics in 2010.

The results for the mean values and the spread for various extrapolation ranges is shown in Table 6.1, the statistical uncertainty results from the uncertainties on the fit parameters.

Overall there is a good agreement between the Monte-Carlo expectations, the fit expectation and the actual observed events. For very high ranges the spread makes the biggest contribution to the uncertainty, it goes up to 70 %, which is expected because of the steeply falling spectrum. The fit and the extrapolation cover several orders of magnitude, in the beginning each bin of the distribution contains about $10^3 - 10^4$ events and in the extrapolation only 10^{-2} events are expected.

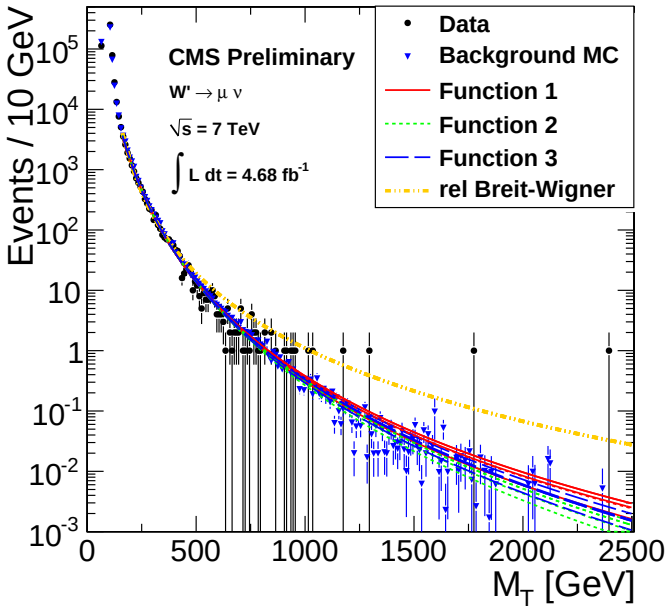

Figure 6.1.: Fit to data of the three functions for various sideband variations as well as the relativistic Breit-Wigner, which was used in earlier stages of the analysis. The blue triangles represent the expected Monte-Carlo background.

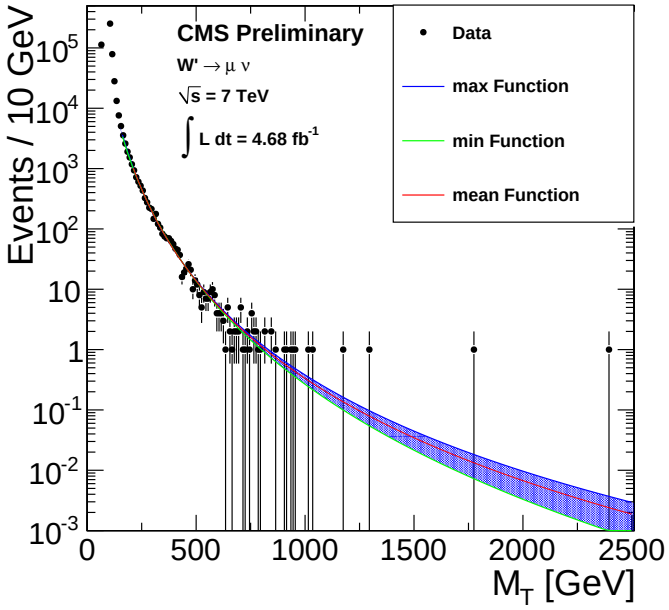

Figure 6.2.: Mean of all the various fits with the spread taken from the minimum and maximum of the various functions.

Extrapolation range in M_T	Number of events					Ratio Data/Mean Fit
	Mean Fit	Spread	Stat. Uncertainty	All MC Backgrounds	Data	
190−600	8260	160	110	8870	8270	1.00
>600	72.3	11.2	4.1	74.9	62	0.86
>700	36.4	8.0	2.3	37.1	36	0.99
>800	19.9	5.7	1.4	18.7	16	0.81
>900	11.6	4.1	0.8	10.0	11	0.95
>1000	7.07	2.93	0.54	5.73	6	0.85
>1100	4.50	2.16	0.35	3.18	4	0.89
>1200	2.96	1.61	0.24	1.90	3	1.01
>1300	2.00	1.21	0.16	1.31	2	1.00
>1400	1.38	0.92	0.12	0.91	2	1.45
>1500	0.97	0.70	0.08	0.63	2	2.06

Table 6.1.: Results of the sideband fit in the sideband and various extrapolation ranges. Also shown are the number of observed data events of the CMS detector in 2011 after applying all selection steps and the expected number of events from the simulation of all background samples.

6.2. Fitting The Full M_T Distribution

Another option is to use the whole M_T distribution obtained from the data and model it with a function. Later on interference effects between the SM W and the W′ will be included into the analysis, this interference effects can lead to a different transverse mass distribution, see Section 8. Fitting the whole distribution of the observed data events with one of these functions is not feasible in the presence of a signal, because non of the functions is capable of describing the interference effects. In the presence of a signal the fit would lead to a wrongly estimated number of SM background events, therefore this option is not used. However, this is one of the options that will be investigated in the future, but it needs a lot of work to get a theoretical description of the W boson shape up to very high masses as well as a parameterization of the interference effects.

6.3. Monte-Carlo based Background Expectation

Later on interference effects will be discussed and for the case of interference the sideband fit is not practicable. A non-interfering signal would have negligible impact in the sideband, in case of a signal which interferes with the SM W boson the shape of the SM W would change due to the interference. This distortion would manifest itself even in the sideband region and hence influence the outcome of the fits resulting in a background expectation, which differs from the "SM-only" expectation, therefore relying on the simulation is a more viable option.
One option would be using the Monte-Carlo expectation directly, but even with the dedicated high p_T muon W sample, which was generated with Pythia, not all bins in the distribution are filled due to the lack of statistics, so in order to get a smooth description of the background the MC distribution is fit with one of the previous functions over the whole M_T distribution and afterwards it is normalized to the data in the sideband. All of the functions agree reasonably well, so the simplest function was chosen:

Fit function to MC:

$$\frac{a}{(M_T + b)^c}. \tag{6.4}$$

This function is fit to the whole spectrum of the simulation and in a second step the number of expected events from this fit in the range 200 to 500 GeV is compared to the actual observed data in that range and a scale factor of about 0.97 is obtained. The fit function is then scaled by this factor and used as the background expectation.
The results can be seen in Figure 6.3, the grey histogram represents the Monte-Carlo simulation, the black dots represent the data points, the black dashed line is the fit to the Monte-Carlo simulation and the red line is the same fit scaled to the number of observed events in the sideband.

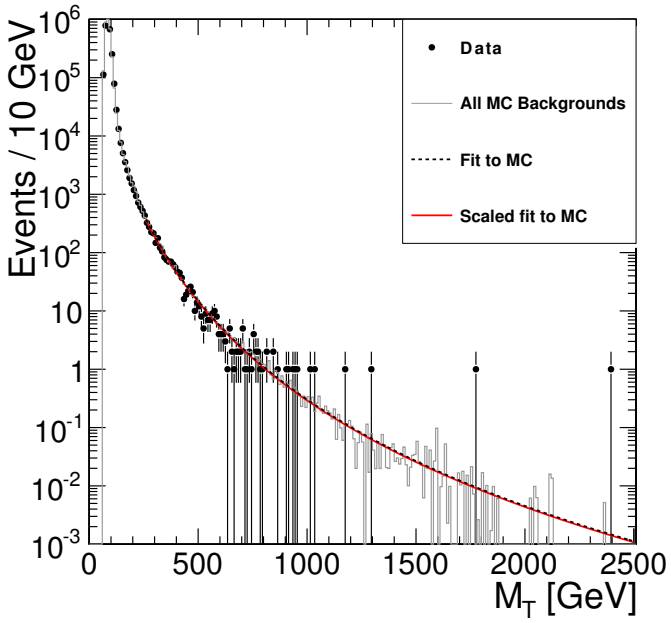

Figure 6.3.: The fit (black dashed line) is performed to the whole Monte-Carlo M_T spectrum (grey histogram). Afterwards the fit is scaled to the number of data events in the sideband from 200-500 GeV and the "scaled fit" (red line) is obtained.

There is an uncertainty on the fit which arises due to the uncertainty of the fit parameters. Besides that there is also a set of possible systematic uncertainties that influence the shape of the simulated transverse mass spectrum, see Section 5.8. In order to determine the influence by these systematics the smeared transverse mass distributions are fit with the same parameterization and the deviations are taken as the uncertainty of the background expectation.

The numerical results can be found in Table 6.2. The scaled fit, the Monte-Carlo expectation and the observed data are in good agreement. The statistical uncertainty of the fit is around 5-10 % in the relevant high M_T search ranges. The systematic uncertainties are smaller than the statistical ones for very early starting values of the integration, but for very high starting values they are the main source of uncertainty with up to 40 % for

Extrapolation range in M_T	Number of events					Ratio Data/Fit
	Data	All MC Backgrounds	Fit to MC	Stat. Uncertainty	Syst. Uncertainty	
>500	141	169.0	157.6	8.2	5.1	0.89
>600	62	74.9	67.9	4.2	3.4	0.91
>700	36	37.1	32.6	2.3	2.7	1.11
>800	16	18.7	17.0	1.3	2.0	0.94
>900	11	10.0	9.48	0.78	1.49	1.16
>1000	6	5.73	5.58	0.49	1.08	1.08
>1100	4	3.18	3.44	0.32	0.79	1.16
>1200	3	1.90	2.20	0.21	0.58	1.36
>1300	2	1.31	1.45	0.14	0.43	1.38
>1400	2	0.91	0.98	0.10	0.33	2.04
>1500	2	0.63	0.68	0.07	0.25	3.17

Table 6.2.: Results of the fit to all simulated samples, the fit is then scaled to the data in the sideband 200-500 GeV. The first column shows the lower bound of the extrapolation, the second the observed data, the third the event yield from the MC expectation, the fourth the event yield from the fit on MC scaled to the data in the sideband, the fifth the statistical uncertainty, the sixth the systematic uncertainty on this event yield and the last one the ratio of observed data to the event yield of the MC fit.

transverse masses above 1.4 TeV. For for very high windows in the transverse mass the ratio of observed data events to expected background events is getting very high and suggests a significant excess, which is not the case. This high ratio is caused by the low amount of expected background of only about 0.7 events, while two events are observed in the data. This excess is not significant and the ratio is misleading.

6.4. Possible QCD Background

The multi-jet (QCD) background is the background component with the largest uncertainty on the cross section, because only leading order calculations are available, and the simulated number of events is too low for high transverse masses. The multi-jet MC simulation predicts only events up to transverse masses of 250 GeV that fulfill all the selection criteria, therefore a data-driven crosscheck is performed to verify that multi-jet events can be neglected in the high-M_T regions.
At first the normalization of the QCD background is obtained based on the distribution of the ratio of muon p_T to transverse missing energy (see Figure 5.6), this distribution obtained before the kinematic selection steps. Taking advantage of the fact, that the W background peaks at $p_T/MET \sim 1$, the multi-jet background can be separated by its behavior of being flat up to values of p_T/MET around 10. This flat behavior is caused by the property of multi-jet events to have no physical contribution to the MET, therefore the ratio of muon p_T and MET is large.
The goal of a getting QCD normalization is achieved in two steps, first in the p_T/MET distribution the contributions of all SM processes besides QCD and $W \to \mu\nu$ based on the MC simulation are subtracted from the observed data on a statistical basis. Afterwards a fit to the remaining data in the p_T/MET distribution containing the contributions from W and QCD events is performed to obtain the number of QCD events. The shape for the W background is taken from the MC prediction and can be described

very well by a Crystal Ball function. For the QCD shape a template is obtained from the MC simulation. The left plot in Figure 6.4 displays the fit of the different shapes for W and multi-jet backgrounds to the remaining data to obtain the total number multi-jet events. This yields a total number of 452300 ± 24200 events including systematics in the distribution, this is about 40 % more than the simulation predicts. This scaling factor of 1.4 is used to scale the final transverse mass distribution of QCD. Afterwards events within $0.4 < p_T/MET < 1.5$ are selected because of the two-body kinematics, only about 12 % of multi-jet events pass this selection, see Table 5.3. In the second kinematic selection using the angle between the muon and the missing transverse energy the number of multi-jet events is reduced further to about 10 % with respect to the first kinematic step.

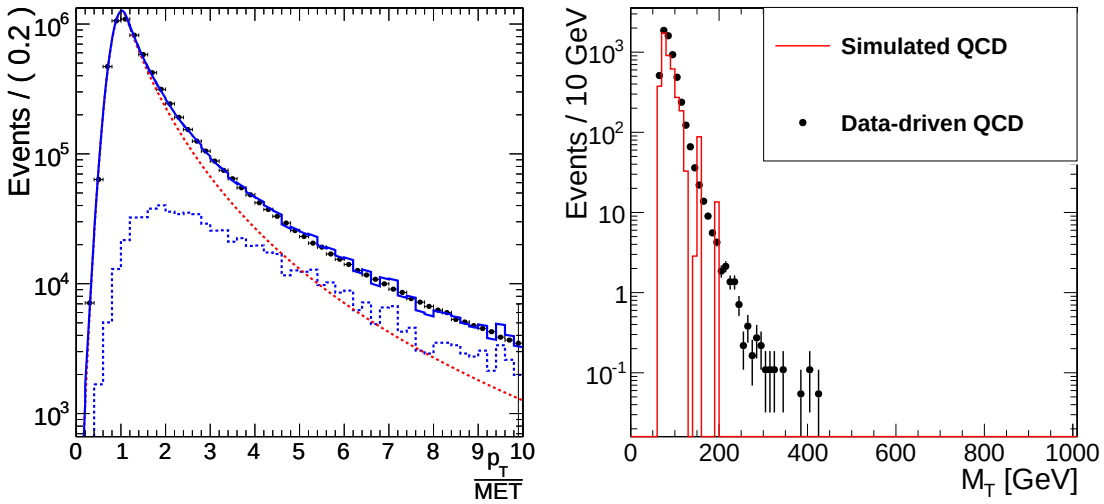

Figure 6.4.: Left: Fit of the W plus multi-jet shape to the p_T/MET distribution resulting in a scaling factor of 1.4 for the multi-jet sample. Right: Transverse mass distribution obtained by non-isolated data events compared to the multi-jet simulation.

The simulated multi-jet sample is lacking statistics, therefore in a second step the shape of the transverse mass distribution for multi-jet events is obtained from data by taking only non-isolated data events. For relative tracker isolations above 0.25 the dominant contribution is due to multi-jet events, see Figure 5.5 on the right. The default analysis selection on the relative tracker isolation is adjusted to only select events with a relative tracker isolation above 0.25, while the other selection steps are kept the same. Thus a multi-jet dominated transverse mass distribution can be obtained. This transverse mass distribution contains about $1.1 \cdot 10^5$ events and is then scaled to the 5800 from the simulation expected events including the previously obtained scaling factor of 1.4. The result can be seen in Figure 6.4 on the right. Even though the data-driven transverse mass distribution has much higher statistics than the simulation, there are still no events with transverse masses above 450 GeV, therefore the multi-jet contribution is negligible for this analysis.

7. Limit Setting

The event with the highest transverse mass has a transverse mass of about 2.4 TeV, which is very rare in Standard Model processes. The Standard Model MC simulation predicts 0.015 ± 0.007 events above 2.4 TeV, while the fit to the MC distribution yields a higher prediction of 0.06 ± 0.05 events. The probability of getting such an high event by SM processes according to a Poisson distribution is rather low with about 1.5 % for the MC prediction and 6 % for the prediction of the fit. This is still in agreement with the SM expectation, therefore an exclusion limit on the W′ signal production cross section and the W′ mass can be calculated.

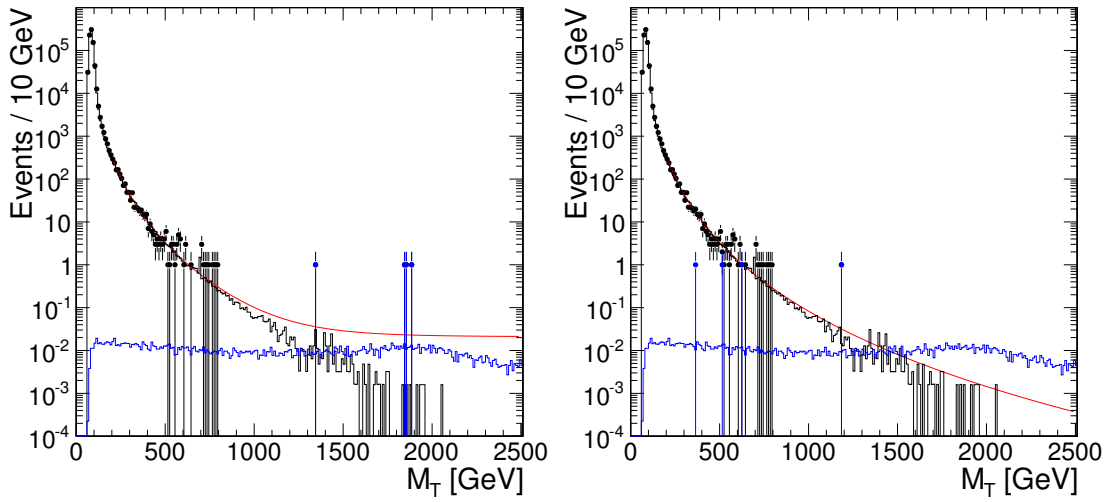

Figure 7.1.: Two scenarios how a potential signal would show up, "lucky case"(left) and "unlucky case"(right). The black dots represent the first 1.1 fb^{-1} of the 2011 data, the black lined histogram is the MC expectation, the blue lined histogram is the signal histogram of a W′ with mass 2.3 TeV and the blue points are diced signal events according to the luminosity of 1.1 fb^{-1}. The red line shows a fit to the whole spectrum.

In this early stage a potential signal would show up as an excess of a few events with high transverse mass. In Figure 7.1 two simulated scenarios of an existing W′ with a mass of 2.3 TeV are shown together with the first 1.1fb^{-1} of the CMS data in 2011. These scenarios show, that a potential W′ would show up as a slight excess and that due to the bad momentum resolution these additional events could appear anywhere in the distribution. Therefore a shape based analysis is not needed and a simpler approach is used.
The diced signal events in the two scenarios correspond to an integrated luminosity of 1.1fb^{-1}. Due to the bad momentum resolution the shape of the signal is nearly flat and signal events may appear anywhere in the spectrum. In the "unlucky case"(on the

right of Figure 7.1) the signal would not be visible. The five diced signal events are accumulated in the low transverse mass region and they are in good agreement with the Standard-Model-only hypothesis. In the second case, the "lucky case", the distribution of the signal events is more advantageous and the signal could be easily found due to an excess in the high transverse mass region. The red lines in the two plots in Figure 7.1 indicate fits to the data events including the diced signal events. The fits are based on the same parameterization as in the previous Section 6.3 with an additional constant, which should account for a possible flat signal contribution. If this constant is different from 0, it indicates a potential signal. In the "lucky case" it is non-zero and would show the signal contribution, but in the "unlucky case" the fit does not show any signal contribution and it would be difficult to find such a signal.
However, since there is no sign of a possible signal contribution in the observed CMS data of 2011, an exclusion limit on the mass of the W′ can be derived. Due to the low statistics in the tail of the distribution a shape sensitive analysis is very difficult and not really needed for setting an exclusion limit. Therefore a simpler approach is used, the single bin counting experiment.

7.1. Single Bin Counting Experiment

In the single bin counting experiment the number of expected and observed events in a so-called "search window" are compared and then an exclusion limit on a potential signal cross section can be computed. In Figure 7.2 the principle of the search window is shown, the observed events are obtained by counting the data events above the starting point of the search window M_T^{lower} and the expected events are calculated by integrating the fit function above M_T^{lower}, see Section 6.3.

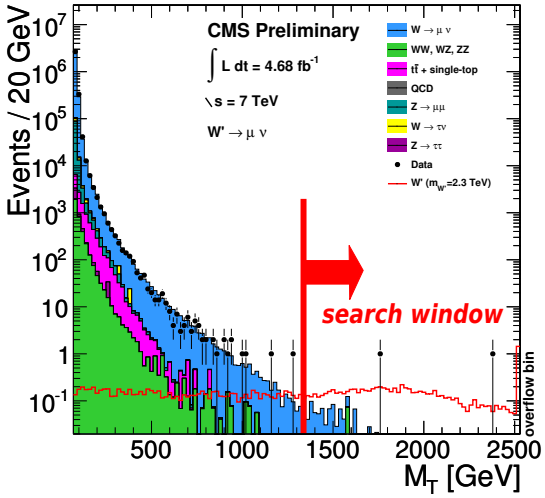

Figure 7.2.: Transverse mass distribution, the red line indicates the begin of the search window.

In case of a signal the expected total number of events in the search window is given by:

$$N_{exp} = \mathcal{L} \cdot \epsilon \cdot \sigma + N_{bkg}, \tag{7.1}$$

with the total integrated luminosity $\mathcal{L}$, the signal efficiency ϵ, the signal cross section σ and the number of expected background events N_{bkg} obtained by the fit. The signal efficiency ϵ depends on the fraction of signal in the search window, it therefore depends on the starting point of the search window $\mathrm{M_T^{lower}}$ and on the W′ mass, because the shape of the signal is different for each mass. The lower end of the search window is optimized for the best expected limit, that means it is optimized by pseudo-experiments without taking the data into account. The parameter of interest is the signal cross section and as a next step an upper limit on it will be derived using a Bayesian approach.

7.2. Bayesian Limit Calculation

In statistics the Bayesian approach is particular interesting in case of determining specific model parameters or setting limits on these parameters. Here only a very brief introduction based on the summary in the PDG book [11] is given.
Assuming the predicted outcome of an experiment x depends on an unknown parameter θ. In Bayesian statistics the posterior probability density function (p.d.f.) $p(\theta|x)$ describes all the knowledge of the parameter θ. It gives the probability for each possible value of θ by taking the observed data x; it can be obtained using Bayes' theorem:

$$p(\theta|x) = \frac{L(x|\theta)\pi(\theta)}{\int L(x|\theta')\pi(\theta')d\theta'}, \tag{7.2}$$

where $L(x|\theta)$ is the Likelihood function describing the outcome of the experiment as a function of the parameter θ. This Likelihood is evaluated with the observed data x. $\pi(\theta)$ is the prior p.d.f. describing the probability for each possible value of θ based on the knowledge about the parameter before the experiment is performed. The denominator in Formula 7.2 normalizes the posterior p.d.f. to unity.
Besides the parameter of interest, θ, the outcome of the experiment can also depend on other parameters, the nuisance parameters ν, that are only known to a limited accuracy. These nuisance parameters are particular useful for implementing uncertainties of measured values into the posterior distribution. Since the actual values of the nuisance parameters are unknown, a prior function is assigned to each of them and in order to get the posterior p.d.f. the Likelihood is integrated over the nuisance parameters:

$$p(\theta|x) = \int p(\theta, \nu|x)d\nu. \tag{7.3}$$

By integrating over the posterior p.d.f. an interval for the parameter of interest θ can be computed, in which the parameter of interest lies with a certain probability. This can be written as

$$\int_{\theta_{low}}^{\theta_{high}} p(\theta|x)d\theta = \alpha, \tag{7.4}$$

so that with a probability of α the parameter of interest is between θ_{low} and θ_{high}. In this analysis only upper limits are interesting. This can be done by setting the lower bound of the integral to 0. The most common choice for setting exclusion limits is done by stating the 95 % confidence intervals, this can be calculated by setting $\alpha = 0.95$. So in this case only the upper bound in the integral has to be computed.

For the calculation the RoostatsCL95 tool [93] is used, which is officially recommended by the CMS Statistics Committee. The model given in Formula 7.1 is built in RooStats [55], the Likelihood used is a Poisson Likelihood:

$$L = \frac{(L \cdot \epsilon \cdot \sigma + N_{bkg})^{N_{obs}}}{N_{obs}!} \cdot e^{-(L \cdot \epsilon \cdot \sigma + N_{bkg})}. \tag{7.5}$$

The parameter of interest is the signal cross section σ, while the other parameters (L, ϵ and N_{bkg}) are modeled as nuisance parameters and N_{obs} being the actual number of observed data events in the search window. Log-normal prior shapes are used for the nuisance parameters, but also also other prior shapes (Gaussian or Gamma) were tested, but there was no observable difference in the result compared the log-normal prior shapes. The parameter of interest, the signal cross section, is modeled with a uniform prior.
The calculation of the posterior probability function is done by the BayesianCalculator by using Markov Chain Monte Carlo methods [94]. The posterior distribution is calculated by integrating the Poisson Likelihood over all of the nuisance parameters and taking their prior shapes into account:

$$\Pi(\sigma|N_{obs}) = \int dL\, d\epsilon\, dN_{bkg}\, \frac{(L \cdot \epsilon \cdot \sigma + N_{bkg})^{N_{obs}}}{N_{obs}!} \cdot e^{-(L \cdot \epsilon \cdot \sigma + N_{bkg})} \cdot \pi(L) \cdot \pi(\epsilon) \cdot \pi(N_{bkg}) \cdot \pi_{poi}(\sigma), \tag{7.6}$$

where the π represent the different priors. The upper limit on the signal cross section is then taken as the 95 % confidence interval of the posterior probability distribution.
Another important limit is the expected limit, which is purely simulation based and does not use the observed data. In this analysis it is used for the optimization of the search windows. Besides this optimization it gives an estimate where the limit is expected to be. It also allows to compare the observed limit to the expected limit and to see if both are in agreement or not.
To calculate the expected limit the observed limit is calculated for 1000 pseudo experiments, where the number of observed events is diced based on the expected number of background events. Also in each of these pseudo experiments the nuisance parameters are diced according to their uncertainty and their prior functions, the median of these 1000 pseudo experiments is then taken as the expected limit. Besides the expected limit also the 1- and 2-σ bands can be computed by these pseudo-experiments, they correspond to the 68 % and 95 % intervals.
In case that the observed number of events N_{obs} is smaller than the expected number of events, then the observed limit can exclude a smaller signal cross section, because less events than the Standard Model predicts are observed in the data and a smaller additional cross section can be excluded. In case the observed number of events N_{obs} is bigger than the expected number of events, then the observed limit can only exclude a bigger cross section than the expected limit. In order to get an estimate if the observed and expected limit are in agreement, the 1- and 2-σ bands are used to give an estimate of how far the observed limit can spread.
The analysis will be combined with the analysis for $W' \to e\nu$ later on, therefore the single bin counting experiment gets extended by a second channel with the same model. This is done by multiplying the Likelihoods of both the single channels in the posterior p.d.f. and integrating over all the nuisance parameters of both channels.
For the calculation of the combination again a RooStats [55] tool is used. An adapted version of the ADD di-lepton [95] tool can be used, because in that analysis also two

channels using single bin counting experiments are combined as well. For the calculation the BATCalculator is used, which is part of the Bayesian Analysis Toolkit [56].

7.3. CL_s Limit Calculation

Another method to calculate exclusion limits is the CL_s method, which uses a frequentist interpretation of statistics. CL_s limits are only used for comparison, therefore the method is only explained briefly, based on [96].
The central part of the CL_s method is the test statistic X, which depends on the possible signal s and the expected background b. It allows to test the outcome of the experiment under possible signal assumptions. For the exclusion limits in this analysis the profile likelihood ratio test statistic is used.
In order to set an exclusion limit two hypotheses have to be tested: The signal and background (s+b) hypothesis assumes there is signal and SM background, while the background-only (b) hypothesis assumes that there is only SM background. Starting with the s+b hypothesis, the test statistic is evaluated with the observed data X_{obs} and compared with pseudo-experiments, where the observed data is diced according to an assumed signal and background. Afterwards the test statistic is evaluated for each of the pseudo-experiments resulting in a distribution of possible outcomes under the assumptions of a signal s and background b. The CL_{s+b} value is then defined as the probability of having a smaller test statistic then the one observed in data:

$$CL_{s+b} = P_{s+b}(X \leq X_{obs}). \tag{7.7}$$

The same can be done for the background-only hypothesis with the assumption that there is no signal contribution and the outcome of the experiment is only depending on the background b, this is equivalent with setting the signal contribution to 0. Again pseudo-experiments are performed and the corresponding CL_b is defined as the probability of getting a lower test statistic than the one evaluated with the observed data:

$$CL_b = P_b(X \leq X_{obs}). \tag{7.8}$$

For the exclusion the quantity CL_s is used, it is defined as the ratio of CL_{s+b} and CL_b:

$$CL_s = \frac{CL_{s+b}}{CL_b}. \tag{7.9}$$

In case of no signal contribution in the observed data the CL_{s+b} value is small, while the CL_b is close to 1, therefore CL_s is small as well. A common threshold for excluding a signal contribution in the observed data is to choose $CL_s < 0.05$. For this analysis an exclusion limit on the signal cross section is needed, therefore the CL_s is computed for a range of possible signal cross sections. The cross sectionswhich fulfill $CL_s < 0.05$ are excluded.
CMS and ATLAS agreed to use CL_s limits in their analyses, where both experiments publish limits, so that the result can be easier compared. An exception is allowed, when both experiments used Bayesian limit calculation in earlier publications. CMS used Bayesian statistics from the beginning in their W' limit calculation and in ATLAS' last W' paper [97] also Bayesian limits were used, so the CL_s limits are only used as a cross-check.
The computation of the limits is performed using the RooStatsCL95 tool [93] with the

profile likelihood ratio test statistic. For each tested signal cross section 10000 pseudo-experiments are performed for the signal and background and the background-only hypothesis. In comparison between CL_s and Bayesian limits can be seen in Figure 7.3. The limit is computed with an older set of background evaluation and therefore differs slightly from the most recent result, but the plot is just shown to illustrate the differences of the two methods. Both methods agree reasonable well, the computed cross section limits for each masspoint agree within 5 % and also the variation with the W′ mass is observed with both methods. The Bayesian limit is slightly more conservative than the CL_s limit.

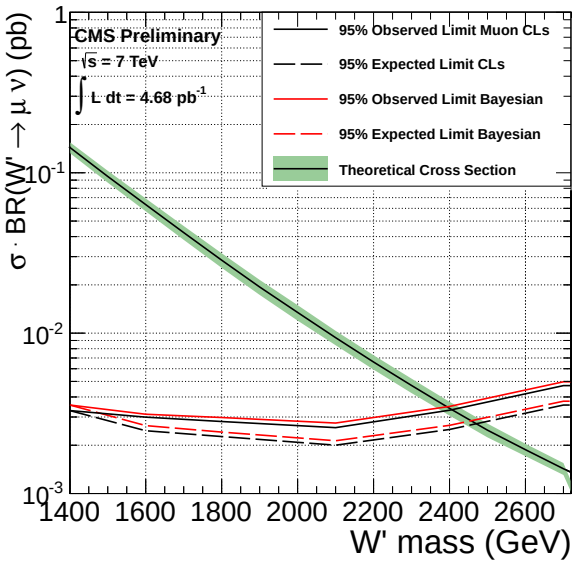

Figure 7.3.: Difference between Bayesian and CL_s Limit results. The black solid line with the green error band shows the theoretical cross section according to the Pythia model. The dashed lines show the expected limit for Bayesian(red) and CL_s(black) limit setting and the solid lines show the observed limits. The limit differs slightly from the other limits shown later, because it is computed with an earlier evaluation of the background.

7.4. The Muon Limit

Now everything needed for the limit calculation has been obtained and the limit as a function of the W′ mass can be seen in Figure 7.4 and Table 7.1.

Together with the observed and expected limit also the $\pm 1, 2 - \sigma$ bands are shown, the observed limit is slightly worse than the expected limit, because a slight excess over the background expectation is observed at very high transverse masses. For the highest chosen search window of 1450 GeV the expectation is 0.8 ± 0.4 events and 2 events are observed, which is in good agreement.
Besides the cross section limits also the theoretical expected cross section is shown in Figure 7.4 and Table 7.1, the corresponding uncertainty results from the parton density function uncertainties described in Section 4.4.2. To translate the cross section limits

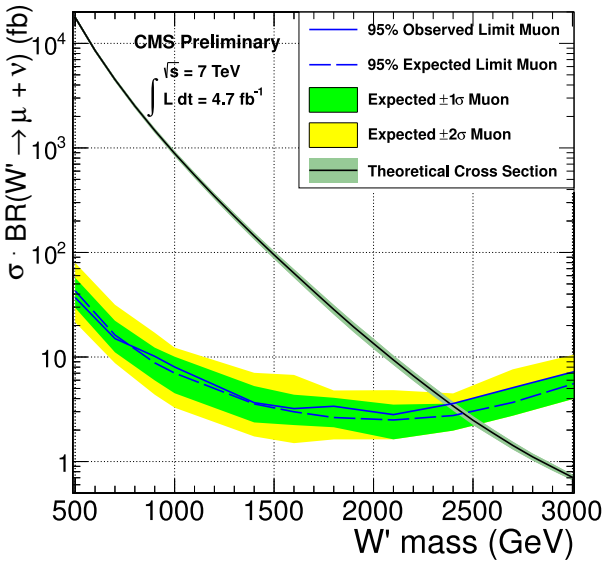

Figure 7.4.: Observed and expected limit computed with the Bayesian approach in the decay channel $W' \to \mu\nu$. The black solid line with the green error band shows the theoretical cross section according to the Pythia model with it's uncertainty due to the PDF uncertainty. The blue dashed line shows the expected limit with the 1- and 2-σ band and the blue solid line shows the observed limit.

into a limit on the W′ mass the intersection of the observed limit and the theoretical prediction is extrapolated to the x-axis, this is the observed limit. For the theoretical prediction the central value of the uncertainty band is taken following the CMS recommendation. The central value corresponds to the best fit of the PDF set, which is used for the signal generation. The PDF uncertainties are neglected when the central value is taken, but because the signal cross section falls steeply with the W′ mass, these uncertainties would only have a small impact on the W′ mass limit.
The limit computation yields a lower bound for the mass of a W′ with Standard-Model-like couplings of

$$\boxed{m_{W'} \geq 2.4\,\text{TeV} \qquad @\ 95\,\%\ \text{CL.}} \tag{7.10}$$

The expected limit is slightly higher with 2.45 TeV due to the slight excess in the observed data. In Table 7.1 the input of the limit calculation together with the numerical values of the cross section limit can be seen for some interesting mass points.
Also the chosen lower bound of the search window is shown in the table, it is optimized to get the best expected limit. Basically the lower bound of the search window increases with the W′ mass until the off-shell part gets too big and a lower value yields a better expected limit.
For very low W′ masses the lower bound of the search window has to be low in order to keep a sufficient high signal efficiency, but in this lower M_T region the Standard Model background is higher. This higher background yields a worse exclusion limit on the signal cross section than for higher masses, see Figure 7.4. A similar effect is seen for very high W′ masses for which the off-shell production starts to dominate. For very high masses a large fraction of the signal events is accumulated in the low transverse mass

region and therefore the search window is optimized with a lower starting value. The higher background and the lower signal efficiency due to the off-shell production yield the lower exclusion limit in terms of signal cross section for high W′ masses.

W′ mass (GeV)	M_T^{lower} (GeV)	N_{sig} (Events)	N_{bkg} (Events)	N_{data} (Events)	σ_{theor} (pb)	Exp. Limit (pb)	Obs. Limit (pb)
500	350	38800 ± 3000	749 ± 39	732	17700	42.9	37.0
700	550	8160 ± 970	102 ± 10	100	4510	16.3	15.0
900	700	2740 ± 340	32.6 ± 5.0	36	1470	8.79	10.2
1000	750	1730 ± 140	23.3 ± 4.1	26	886	7.02	8.03
1400	1000	294 ± 24	5.58 ± 1.57	6	144	3.56	3.66
1600	1100	128.1 ± 8.6	3.44 ± 1.11	4	63.3	2.99	3.21
1800	1250	53.1 ± 3.4	1.78 ± 0.68	3	28.5	2.64	3.38
2100	1300	17.4 ± 0.9	1.45 ± 0.58	2	9.37	2.50	2.81
2400	1400	5.20 ± 0.25	0.98 ± 0.43	2	3.40	2.76	3.59
2700	1450	1.57 ± 0.07	0.81 ± 0.37	2	1.43	3.68	5.09
3000	1400	0.54 ± 0.02	0.98 ± 0.43	2	0.71	5.51	7.17
3500	1100	0.15 ± 0.01	3.44 ± 1.10	4	0.30	11.83	12.69

Table 7.1.: Muon Limit: Expected numbers of signal and background events, the number of observed events, the corresponding theoretical signal cross section, and expected and observed limits for different W′ masses and search windows.

7.5. The Electron Limit

As already stated previously an analogue analysis is performed in the electron channel $W' \to e\nu$. Basically the analysis strategy is the same, there are some quality cuts to ensure the electron is well reconstructed and after that the same kinematic cuts as for the muon channel are applied. The analysis is performed by Jan-Frederik Schulte, the documentation can be found in the references [98, 99]. Here only the result is taken in order to combine it with the muon channel. The used statistics in the electron channel corresponds to $4.74\,\mathrm{fb}^{-1}$, which is slightly higher than for the muons. The overall signal efficiency is comparable in both channels.
As before for the muon channel a fit to the transverse mass spectrum is used to get the expected number of events in the search window. The search window can start at different values, it is optimized separately for each channel. The exclusion limit on the W′ mass is with 2.4 TeV at 95 % confidence level the same as in the muon channel. The two events with the highest transverse mass have $M_T = 1.5\,\mathrm{TeV}$ and $M_T = 1.7\,\mathrm{TeV}$.

7.6. Combination of the Leptonic channels

Both channels $W' \to \mu\nu$ and $W' \to e\nu$ yield the same exclusion limit of 2.4 TeV. To increase the statistical power and extend the exclusion range both channels are combined. This is done by a straight-forward extension of the Bayesian exclusion limit used in the single channels: The single channel Likelihoods are getting combined and in order to get the posterior probability distribution on the parameter of interest, the W′ signal cross section, the combined Likelihood has to be integrated over all the nuisance parameters

of both channels. The numerical computation is slightly different to the single channels, because for the combination the Bayesian Analysis Toolkit [56] is used. For the single channel it was checked, that the outcome of both numerical implementations is the same. For the combination some underlying assumptions have been made:

- The branching ratio for the decays $W' \to \mu\nu$ and $W' \to e\nu$ are the same. The used model has Standard-Model-like couplings, therefore the couplings to muons and electrons is the same and the phase space difference is negligible, hence the branching ratio is the same. However, there are models with different branching ratios for muons and electrons, therefore besides the combined results also the single channel results are important to probe these models.

- There is also the possible decay $W' \to \tau\nu$, where the τ can decay into a muon or electron with about 17 % branching ratio for each of them. However, the resulting transverse mass spectrum is much softer than for the direct decay, see Figure 7.5 for a 2 TeV W′. The resulting additional events would contribute with about 1 % to the expected signal events in the relevant search windows. Since these decays would contribute to the expected signal, it is conservative to neglect it for this analysis.

- The data considered in the electron and the muon channel correspond to the same datasets, therefore the uncertainty on the luminosity measurement in both channels has to be treated as fully correlated.

- The other uncertainties on the signal efficiency and the number of expected background events are taken as fully uncorrelated. Since this is only partially true, especially because the same background sources are considered, the limit was also computed with correlated uncertainties which showed to have a negligible impact on the limit. The plots are done for the 2010 dataset and can be found in AN-10-315 [100].

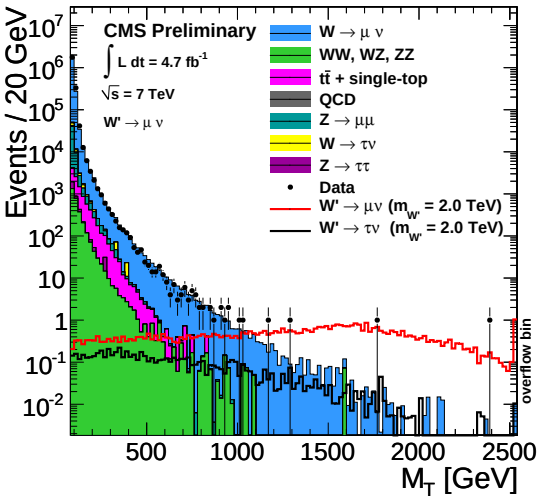

Figure 7.5.: Transverse mass distribution including the $W' \to \tau\nu$ process with the subsequent decay into a muon and missing energy.

With these assumptions the combined limit was computed and it is shown in Figure 7.6, where also the limits of the single channels are shown. By the combination the exclusion limit in terms of W′ mass is extended by roughly 100 GeV, this yields a new lower bound for the mass of the W′ with Standard-Model-like couplings of:

$$\boxed{m_{W'} \geq 2.5\,\text{TeV} \qquad @\ 95\,\%\ \text{CL.}} \tag{7.11}$$

As both single channels show an insignificant excess in the observed data and hence have a slightly worse observed limit than expected, this trend is even more pronounced in the combined limit. The observed limit is slightly outside of the $1\,\sigma$ band, but still inside of the $2\,\sigma$ band. The expected limit is about 2.6 TeV.

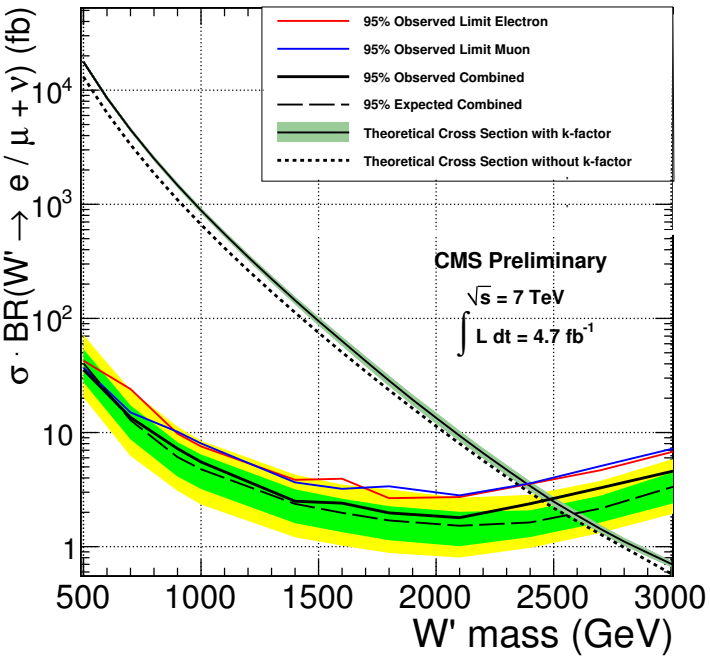

Figure 7.6.: Observed and expected limit by the combination of the $W' \to \mu\nu$ and W′ $\to$ $e\nu$ channels. The black solid line with the green error band shows the NNLO cross section according to the Pythia model with it's uncertainty due to the PDF uncertainty, the blue dashed lines shows the LO cross section. The black dashed line shows the expected limit with the 1- and 2-σ band and the black solid line shows the observed limit. The blue and red solid lines show the single channel observed limits for the muon and the electron channel respectively.

The numerical results of the cross section limit as a function of the W′ mass can be seen in Table 7.2 together with the theoretical cross section.

W′ mass (GeV)	σ_{theor} (pb)	Exp. Limit (pb)	Obs. Limit (pb)
500	17700	37.2	35.5
700	4510	11.6	13.6
900	1470	5.62	7.22
1000	886	4.75	5.52
1400	144	2.21	2.45
1600	63.3	1.86	2.41
1800	28.5	1.56	1.98
2100	9.37	1.51	1.80
2400	3.40	1.58	2.38
2700	1.43	2.06	3.28
3000	0.71	3.35	4.55
3500	0.30	7.28	7.87

Table 7.2.: Cross section limit by combining the electron and muon channels, shown are the observed and expected limits and the theoretical cross section for different W′ masses.

8. Interference of W and W′ contributions

All the previously computed limits were based on the assumption of no interference between the W′ and the Standard Model W. As a recent addition interference effects are included into the analysis.
As described in Section 1.4.4 the W′ can have left- and right-handed couplings. If there is a left-handed coupling to fermions, then there is interference between the Standard Model W boson and the heavier W′. How this interference affects the analysis depends on the magnitude and the sign of the couplings.

8.1. Model Implementation and Event Generation

In the considered models there is no difference between the three generations, therefore the W′ has four important couplings, the right-handed couplings to leptons (C_l^R) and quarks (C_q^R) and the corresponding left-handed couplings (C_l^L) and (C_q^L).
For now three different models where implemented in the matrix element generator Madgraph 4 [61] by Scott Thomas and Can Kilic. In the three different models there are the following couplings for the W′:

- No-interference ($C_l^R = C_q^R = g$, $C_l^L = C_q^L = 0$). The W′ has right-handed couplings with the same strength as the Standard Model W left-handed couplings, therefore there is no interference between the W and the W′. This model agrees with the implementation in Pythia.

- Destructive interference ($C_l^L = C_q^L = g$, $C_l^R = C_q^R = 0$). The W′ has left-handed couplings with the same strength as the Standard Model W couplings. Due to the structure of the interference term in Equation 1.54 the interference depends on the momentum transfers q in the collision. In the s-channel production of the W′ this momentum transfer q corresponds to the center-of-mass energy of the colliding partons $\sqrt{\hat{s}}$, which is the energy that is available in the collision. For the same sign of the W and W′ couplings this leads to a negative interference term for $\sqrt{\hat{s}}$ values between the masses of the two bosons. Therefore this model is referred to as destructive interference. However, for $\sqrt{\hat{s}}$ smaller than the SM W mass or greater than the W′ mass this leads to a positive sign of the interference term.

- Constructive interference ($C_q^L \cdot C_l^L = -g^2$, $C_l^R = C_q^R = 0$). The product of the left-handed couplings to quarks and to leptons for the W′ has the same magnitude but the opposite sign as the product of these couplings for the SM W. This causes an opposite sign for the quark and lepton vertices, which results in a positive sign of the interference term between the masses of the two bosons, therefore it is called constructive interference from now on. As for the destructive interference case the sign of the interference term changes its sign for $\sqrt{\hat{s}} < m_W$ and $\sqrt{\hat{s}} > m_{W'}$.

The strength of the couplings can be arbitrary, so for this first look the strength was chosen to be identical to the coupling strength of the SM W, as a result of this the width of the W′ is identical to the Pythia case.
A technical consequence of the interference of the SM W and the W′ is that in the simulation both have to be produced together. There is a very big cross section difference of $W \to \mu\nu$ of about $10\,\mathrm{nb}^{-1}$ to $W' \to \mu\nu$ with only several fb^{-1} for very high masses. There is about a factor of $10^5 - 10^6$ between both processes, so for every million of events generated only a few would be in the signal region. To produce this amount of events privately is not feasible at all, therefore a simple cut on the minimum momentum of the muons is applied on generator level to reduce the SM W peak and only produce events with high transverse mass. This minimum cut on the muon transverse momentum is set to 250 GeV and for the very high masses to 350 GeV.
For each of these three models described above Les Houches Event(LHE) files are produced privately for W′ masses of 1.0, 1.5, 2.0, 2.3, 2.5, 2.7 and 3.0 TeV. For each mass point and model 100-200 k events are simulated in Madgraph and then run through the full detector simulation in the CMSSW framework using the LHEInterface [101]. Pythia [21] is used for the showering.
For comparison also a Standard Model W was generated with Madgraph in the same way. This is needed, because the distortion of this expected spectrum has to be analyzed. The cross section of the different samples can be found in Table 8.2 and Table 8.1 and can be seen in Figure 8.1; this cross sections includes the SM W and the minimum p_T cut on the muon of 250(350) GeV. The SM W cross section for muons with a momentum greater than 250 GeV is about 0.029 pb, this value is indicated by the straight line in the left plot in Figure 8.1.

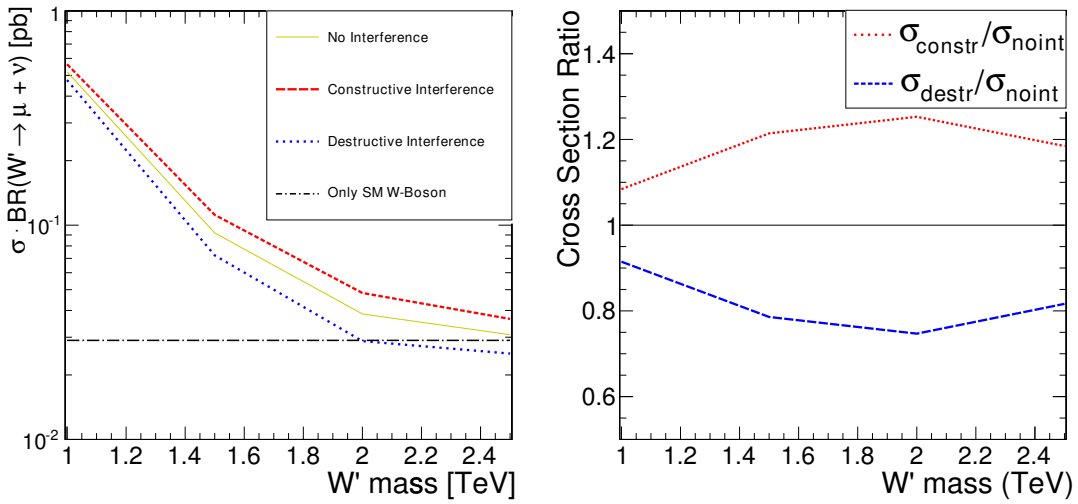

Figure 8.1.: Predicted cross section and cross section ratio as a function of the W′ mass. The blue line in the left figure indicates the cross section of the Standard Model W.

As expected, the cross section for the constructive interference case is bigger and the cross section for the destructive interference case is smaller than the cross section for the case of no-interference.

Generator	$m_{W'}$ (in GeV)	$\Gamma_{W'}$ (in GeV)	σ_{LO} (in pb) W + W′	k-factor AN-11-273	min. pT at generation	# of events
Madgraph	1000	33.3	0.520	1.33	pT>250 GeV	100K
Madgraph	1500	50.2	0.0920	1.27	pT>250 GeV	100K
Madgraph	2000	67.1	0.0385	1.18	pT>250 GeV	100K
Madgraph	2300	77.2	0.0324	1.16	pT>250 GeV	200K
Madgraph	2500	83.1	0.0308	1.14	pT>250 GeV	150K
Madgraph	2700	90.6	0.00693	1.17	pT>350 GeV	200K
Madgraph	3000	101	0.00651	1.22	pT>350 GeV	200K

Table 8.1.: Signal Monte Carlo samples with interference of left-handed W′ and W-boson. The cross sections from Madgraph are for the case without interference, combined for W + W′ for the given p_T-cut. The mass-dependent k-factors are taken from AN-11-273 [68].

W′ mass	1.5 TeV	2 TeV	2.5 TeV	3 TeV (p_T > 350 Gev)
Constructive (pb)	0.112	0.0483	0.0365	0.0080
No-Interference (pb)	0.092	0.0385	0.0308	0.0065
Destructive (pb)	0.072	0.0288	0.0252	0.0050

Table 8.2.: Cross section for several mass points for different interference scenarios. The minimal p_T cut on the muon is set to 250(350) GeV. A visualization of these cross sections can be seen in Figure 8.1.

8.2. Generator Studies

As a first step the no-interference case is compared to the Pythia produced sample that has been used previously in the analysis. The result can be seen in Figure 8.2 for a W′ mass of 1.5 TeV. There are slight deviations between the samples, but the shapes agree reasonably well and the difference in the normalization is of the order of a few percent.
A second comparison is made with the CompHep [102] generator, which is also able to produce interference effects for W′ and is used for the $W' \to tb$ analysis [103]. CompHep is also a matrix element generator and produces LHE files and the implemented model corresponds to the destructive case in Madgraph. Madgraph has the advantage that these three different models are implemented, but so far only for the leptonic channels. Both analyses are working on using the same generator in the future. For now it was checked that the resulting transverse mass spectra are compatible, see Figure 8.2 on the right for the case of destructive interference and a W′ mass of 1 TeV. Both distributions agree perfectly and only statistical deviations are visible, therefore the choice of the generator has no impact on the analysis.
The right plot in Figure 8.2 also shows nicely the comparison between the constructive and the destructive case. Below the mass of the W′ the constructive case has a much larger differential cross section, for masses above the W′ mass this effect is inversed due to the structure of the interference term in Equation 1.54.
For the privately produced Madgraph samples the transverse mass distribution for some of the produced masspoints is shown in the Figures 8.3 and 8.4.

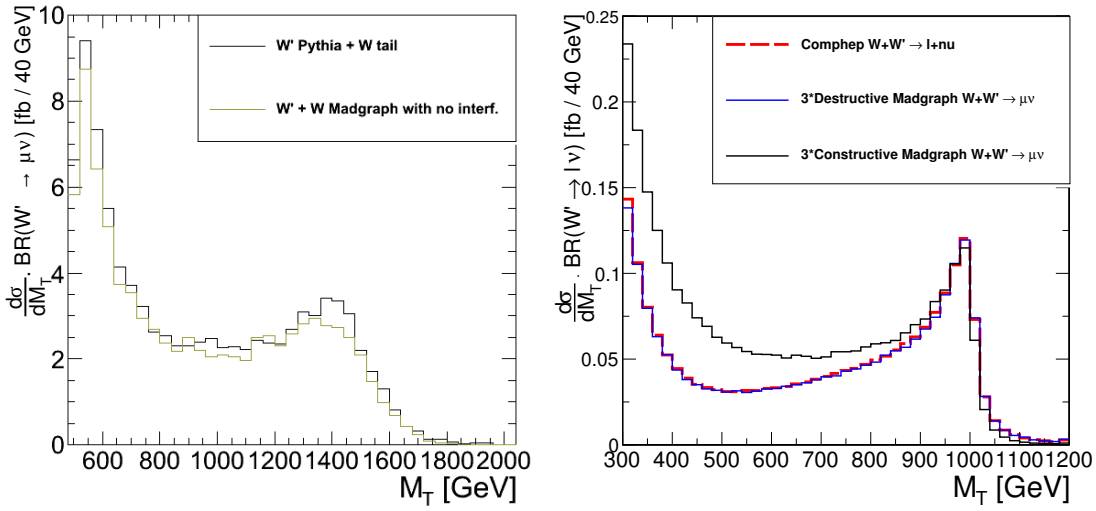

Figure 8.2.: Left: Comparison on generator level between the differential cross section of a W′ with mass 1.5 TeV generated with Pythia and Madgraph. There are slight deviations, but overall the shapes and cross sections agree well. Right: Comparison on generator level between the differential cross section of the Comphep generated sample and the Madgraph sample with destructive and constructive interference for a W′ mass of 1.0 TeV. The lines for both generators lie on top of each other, hence both generators agree perfectly.

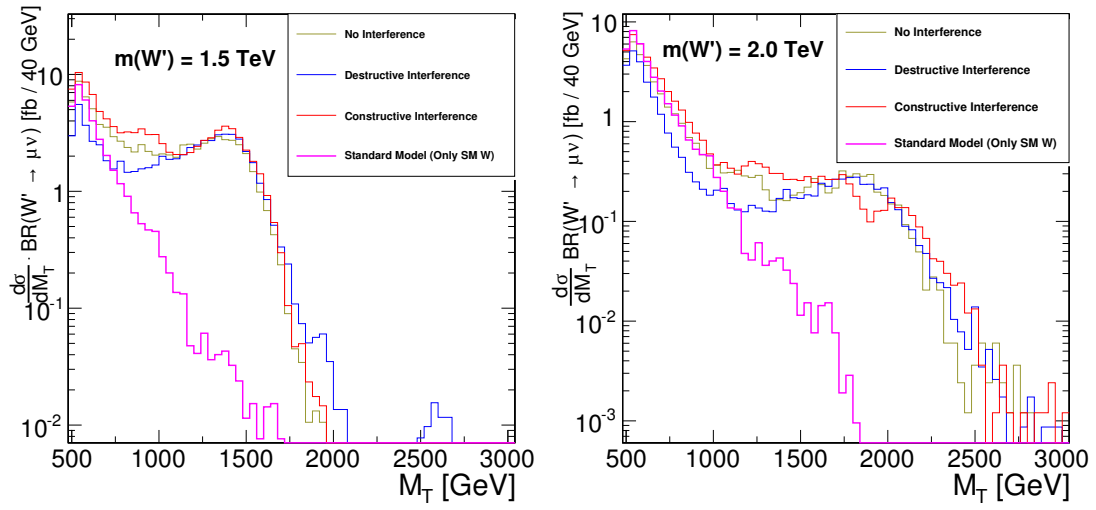

Figure 8.3.: Generated differential cross section for W′ masses of 1.5 TeV(left) and 2.0 TeV(right). The three different signal scenarios correspond to destructive interference (blue), no-interference(yellow) and constructive interference(red). Also the Standard Model W distribution is shown in magenta.

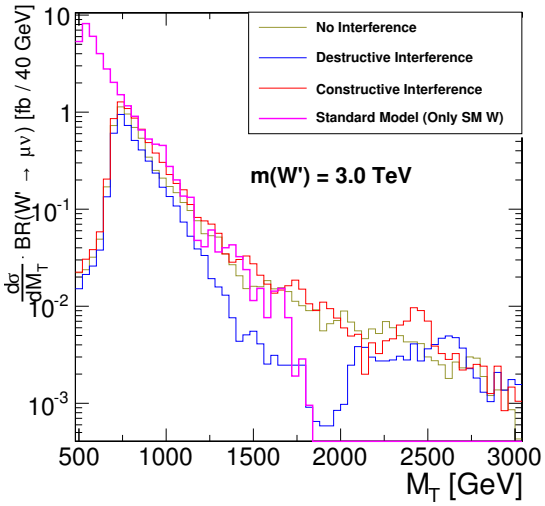

Figure 8.4.: Generated differential cross section for a W′ with a mass of 3.0 TeV. The three different signal scenarios correspond to destructive interference (blue), no-interference(yellow) and constructive interference(red). Also the Standard Model W distribution is shown in magenta.

8.3. Impact of the Interference to the Analysis

As seen in the Figures 8.3 and 8.4 is the position of the Standard Model W and the W′ Jacobian Peak unaffected by the different couplings, but the intermediate region is strongly modulated. Also the number of events in the W′ peak is unaffected by the interference. The modulation region for relatively light W′ with masses below 2 TeV is small, but for very heavy W′ this modulation is much more severe, see Figure 8.4. Especially the destructive interference case is quite interesting, the cross section for some part of the intermediate region drops below the expectation of the Standard Model alone. Hence in some cases, where the peak of the W′ is very small because of the small cross section, it could be possible, that a W′ would manifest itself in a deficit of events in this intermediate region before the peak is visible.

M_T Range	500-750 GeV	750-1000 GeV	1000-1250 GeV	1250-1500 GeV
SM	112	16.7	3.4	0.7
Constructive	179	39.0	14.4	12.7
No-Interference	115	23.8	9.5	7.0
Destructive	92	12.5	5.4	5.5

Table 8.3.: Expected number of events (W+W′) in various bins of the transverse mass for the different signal coupling scenarios for a W′ with a mass of 2 TeV compared to the Standard-Model-only expectation. The number of events correspond to a luminosity of 4.7 fb^{-1} .

In Table 8.3 the expected number of events for a potential W′ with a mass of 2 TeV with a statistics of 4.7 fb^{-1} are shown. For comparison also the expected events from the Standard Model are given in the table. In the case of destructive interference about 20

events less are expected in the bin 500-750 GeV bin compared to the Standard-Model-only expectation, while only an excess of 5 events in the bin 1250-1500 GeV is expected. So this deficit in the first bin could be found before the excess in the end of the distribution could be observed.

The strong modulation of the W-tail in the transverse mass distribution due to interference effects is the reason why no longer a data-driven approach is used to estimate the contribution from $W \to \mu\nu$. A fit to a sideband in the transverse mass would have to be limited to a region, where a potential interference has no effect. As seen before, the interference effect already starts to modify the shape at a few hundred GeV. Therefore the fit has to be limited to this region and the extrapolation to the signal region would result in bigger uncertainties and limit the sensitivity of the analysis drastically. By using the fit based on Monte-Carlo (see Section 6.3) it is assured that a potential interference in the observed data does not influence the background expectation. The normalization to data in the very narrow sideband is not affected by interference, because the dominant contribution here is due to the SM W peak.
Because the W′ peak is not affected by the interference the impact of the interference in earlier published limits is small, because the optimized search windows started at transverse masses where interference effects could be neglected.
As a next step exclusion limits will be computed that take the interference effect into account.

8.4. Limit Setting

The exclusion limit will be again computed using a single bin counting experiment with an Bayesian approach, see Section 7.2, while the possibilities of a shape-based fit are investigated for future analyses. This time the exclusion limit will be divided in two separate steps. In the first step an exclusion limit on the signal cross section in the search window is calculated as a function of the lower bound of the search window M_T^{lower}. This has the advantage, that it is model independent and the results can be easier used by theorists to compare their model to the already excluded areas. In a second step this excluded cross section in the search window will be translated to a W′ mass for each of the models implemented in Madgraph.

8.4.1. Limit as a Function of the Search Window

Again the expected number of events in the search is given by $N_{exp} = \mathcal{L} \cdot \epsilon \cdot \sigma + N_{bkg}$. Contrary to the previous limit calculations the signal efficiency ϵ does not include the *fraction* of the signal in the search window. In this way only an additional cross section in the search window is excluded, in a second step this excluded cross section is compared to the predictions of the different models to set an exclusion limit on the W′ mass.
The exclusion limit is calculated as a function of the starting point of the search window M_T^{lower} between 500 and 1500 GeV in 50 GeV steps.
For the single channel computation the RooStatsCL95 [93] tool is used again and for the combination the implementation done by Stefan Schmitz for the ADD [95] analysis with the Bayesian Analysis Toolkit [56] is used. The results for the muon channel can be seen

in Figure 8.5 and for the combination in Figure 8.6. The input of the muon channel as well as the results of the limit computation for the muon channel and the combination can be found in the Table 8.4. The corresponding input of the electron channel is taken from the analysis note AN-11-227 [98].

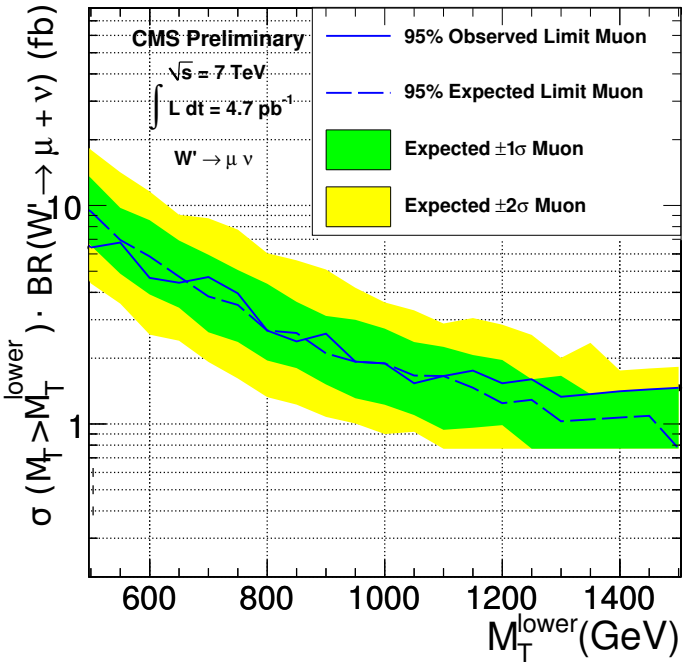

Figure 8.5.: Cross section limit as a function of the lower end of the search window M_T^{lower} in the muon channel.

These exclusion limits are very sensitive to the low statistics in the end of the transverse mass distribution, as a result there are a lot of kinks in the observed curve. Also the different points are not independent of each other, because for the lower start values of the search window the higher transverse masses are always included.
Overall the exclusion limits show the same behavior as the limits derived previously, the agreement between the expected and the observed limit is very good, only for the combination at high transverse masses the agreement leaves the 1-σ band. This is caused by the slightly higher number of observed events compared to the number of expected events.

8.4.2. Limit on the W′ Mass

The exclusion in terms of signal cross section is the most interesting part for theorists to compare their own model to the exclusion. Nevertheless, the exclusion limits on the W′ mass are interesting as well, because they were used before and they are easier to compare than cross section limits. The next step is to compare the three models that are used here and translate the excluded signal cross section into a limit on the W′ mass in the corresponding model.
In order to do this, the additional cross section due to a potential signal as a function of

	Muon channel				Combination	
M_T^{lower} (GeV)	N_{bkg} (Events)	N_{data} (Events)	Exp. Limit (fb)	Obs. Limit (fb)	Exp. Limit (fb)	Obs. Limit (fb)
450	253 ± 18	234	11.3	8.68	11.45	9.46
500	158 ± 13	141	9.38	6.42	8.63	6.41
550	102 ± 9.0	100	6.95	6.77	6.66	6.44
600	67.9 ± 7.6	62	5.84	4.66	5.40	4.20
650	46.5 ± 6.1	45	4.72	4.43	4.20	3.91
700	32.6 ± 5.0	36	3.83	4.70	3.61	3.54
750	23.3 ± 4.1	26	3.51	3.96	2.96	3.10
800	17.0 ± 3.3	16	2.68	2.68	2.68	2.10
850	12.6 ± 2.7	12	2.61	2.39	2.18	1.69
900	9.48 ± 2.27	11	2.10	2.59	1.98	1.76
950	7.23 ± 1.88	7	1.93	1.93	1.72	1.35
1000	5.58 ± 1.57	6	1.89	1.89	1.57	1.40
1050	4.36 ± 1.32	4	1.67	1.54	1.46	1.11
1100	3.44 ± 1.11	4	1.66	1.66	1.29	1.27
1150	2.73 ± 0.93	4	1.46	1.75	1.25	1.29
1200	2.19 ± 0.79	3	1.24	1.54	1.11	0.98
1250	1.78 ± 0.68	3	1.29	1.60	1.02	0.93
1300	1.45 ± 0.58	2	1.03	1.33	0.94	0.84
1350	1.19 ± 0.50	2	1.05	1.37	0.92	0.88
1400	0.98 ± 0.43	2	1.07	1.41	0.91	0.92
1450	0.81 ± 0.37	2	1.09	1.44	0.90	0.96
1500	0.68 ± 0.32	2	0.77	1.46	0.86	0.83

Table 8.4.: Excluded cross sections inside the search window by the muon channel and by the combination. The number of expected background events in the muon channel is taken from the MC based fit, the corresponding numbers for the electron channel can be found in [98]. The expected and observed cross section limits are given for each search window.

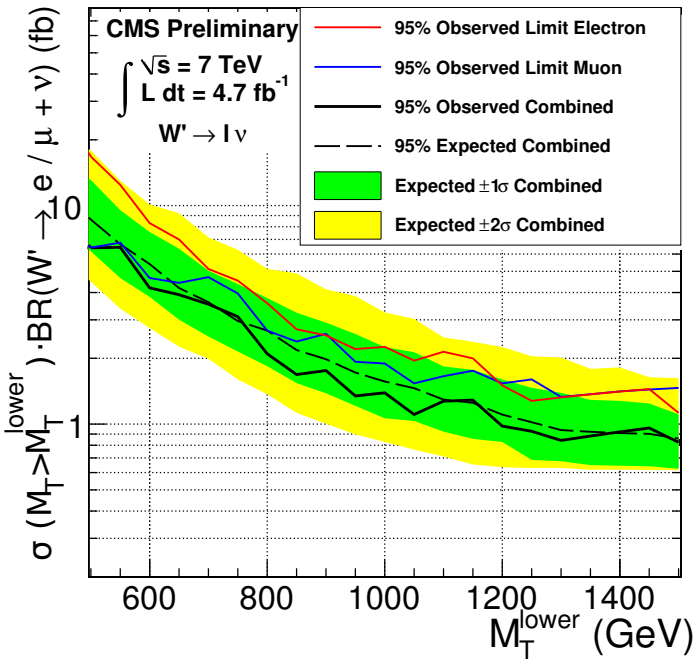

Figure 8.6.: Cross section limit as a function of the lower end of the search window M_T^{lower} by combining both leptonic channels.

the starting value of search window M_T^{lower} has to be derived. This is done by calculating the cross section differences between the various interference samples and the Standard Model W sample. These differences depend on the W′ mass and the starting point of the search window. The exclusion limit is then determined by interpolating between the different W′ masses to get to the value of the excluded signal cross section.
For the interference samples the mass depending k-factors taken from AN-11-273 [68] are used. The resulting exclusion limits on the W′ mass as a function of the search window starting point can bee seen for the muon channel in Figure 8.7 and for the combination of muon and electron channel in Figure 8.8.
The observed mass limits depend strongly on the chosen starting value of the search window and the statistical fluctuation of the observed data. In order to not be biased by the observed data one has to take the observed mass limit from that search window, that yields the best expected limit. For the Pythia case this was done individually for each mass point, in the limit plots in Figures 8.7 and 8.8 the best expected limit can be seen and the corresponding search window has to be taken for the observed exclusion limit.

The case of no-interference corresponds to the Pythia model used in Section 7, hence the limits should be the same taking the same starting value for the search window as before. However the mass limit is slightly worse in the Madgraph case due to two effects: As seen before in Figure 8.2 the LO cross section for Madgraph is slightly below the one from Pythia. The second point is the k-factor that is applied to the signal samples. For deriving the mass limit with the Madgraph samples the cross section difference between the interference samples and the SM W is calculated. For the interference sample, which also includes the SM W, the signal k-factor is used, which is W′ mass dependent, see

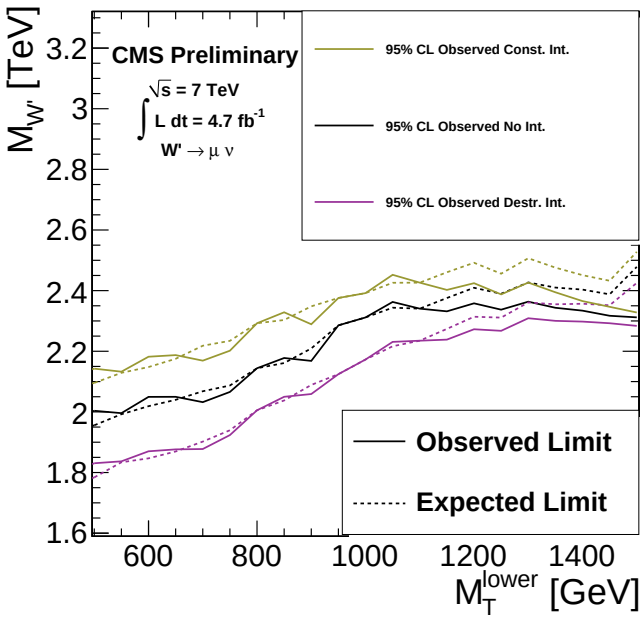

Figure 8.7.: Lower mass limit as a function of the lower end of the search window M_T^{lower} in the muon channel.

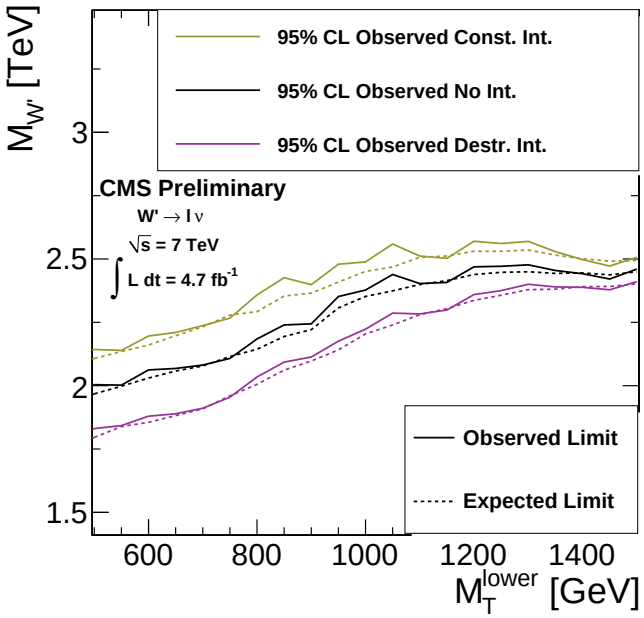

Figure 8.8.: Lower mass limit as a function of the starting value of the search window M_T^{lower} for the combination of both channels

Section 4.4, and slightly smaller than the flat k-factor of 1.32, which is applied to the SM W sample. Therefore slightly different k-factors are applied to the SM W part of the interference sample and the SM W sample that is subtracted. These two effect causes the mass limit of the no-interference case to be about 50 GeV smaller than for the Pythia case. However, since the k-factors for the signal are calculated for the Pythia model, the limits obtained with the Pythia samples are used as final results.
In the Figures 8.7 and 8.8 it is evident that for very low starting values of the search window the difference for constructive, no and destructive interference are bigger than for very high values. This can be explained by the interference effect in the intermediate region. If this region is included in the limit calculation the differentiation power between the models is bigger. At very high masses the limit can not distinguish between the different models, this is due to the fact that the W' peak is unaffected by the interference, see Figures 8.3 and 8.4. On the other hand, the exclusion limits in terms of the W' mass are worse when these intermediate region is included. That is the reason why the optimized search windows in the previous section where set at very high values.
For even higher values of the starting point M_T^{lower} of the search window the mass limit would start to drop, because the background expectation is getting close to 0 for these high values. So by increasing the starting point only the signal efficiency would drop, while the background expectation stays the same.
Even though only a single bin counting experiment was used the method can set limits for these different interference scenarios.

9. Conclusion

In this analysis the search for a new heavy charged gauge boson, the W′, in the decay channel $W' \to \mu\nu$ has been performed. Using the data of the CMS experiment, which corresponds to an integrated luminosity of $4.7\,\mathrm{fb}^{-1}$ at a center-of-mass energy of 7 TeV. The observed data agrees well with the simulated Standard Model background in many different kinematic distributions leading to a good overall agreement between the expectation and the observed data. The main source of background for the search is the Standard Model W boson, which has identical kinematics to the W′ and therefore it is an irreducible background. This background has been studied in detail and a description of it has been developed to get the expected background expectation even for highly off-shell W bosons.
There is no sign of a potential W′ in the decay channel $W' \to \mu\nu$. In the most interesting kinematic distribution, the transverse mass $\mathrm{M_T}$, the event with the highest transverse mass reaches 2.4 TeV, which is a very rare value for Standard Model processes, but it is still in agreement with the Standard Model prediction. Therefore an exclusion limit with a 95 % confidence level was set on the production of a W′ with Standard-Model-like couplings and the subsequent decay to a muon and neutrino using a Bayesian approach. Two kinds of limits are produced. First of all a limit on the mass of a potential W′ with Standard-Model-like couplings is produced, which was the standard procedure for previous searches for W′. The limit reaches an exclusion of $\mathrm{m_{W'}} < 2.4\,\mathrm{TeV}$.
This limit can get even further improved by combining the $W' \to \mu\nu$ analysis with the analogous analysis in the electron channel $W' \to e\nu$ by nearly doubling the statistics. With the combination the exclusion limit can be extended to up to $\mathrm{m_{W'}} < 2.5\,\mathrm{TeV}$, which is the best limit in collider experiments so far. An overview of the CMS exclusion limits based on this analysis as a function of the integrated luminosity can be found in Figure 9.1. Also the corresponding limits of the ATLAS experiment [97, 104] and the latest limits of the Tevatron experiments CDF [28] and DØ [27] obtained with a center-of-mass energy of about 1.96 TeV are shown in the figure.
Besides the electron and muon channel there is also there $W' \to \tau\nu$ channel. There are already studies of the decay $W' \to \tau\nu$ and the subsequently decay of the tau into lighter leptons [105]. Due to the softer spectrum of the transverse mass this leptonic tau channel does not add much for the search of the W′ with Standard-Model-like couplings. There is also a study ongoing in the hadronic tau search and as soon as this is finished it will be combined with the other two searches.
As a second part of the analysis the impact of interference between the Standard Model W boson and the W′ was studied with the help of two model implementations in Madgraph [61]. The impact can be quite severe for high masses of W′ and alter some of the kinematic distributions. In the future the study of the interference will be expanded and the possibility of generalized couplings investigated.
In a last step also model-independent exclusion limits on the W′ production cross section as a function of a lower cut-value on the transverse mass have been produced. These exclusion limits allow to probe various models without the need of a dedicated analysis.

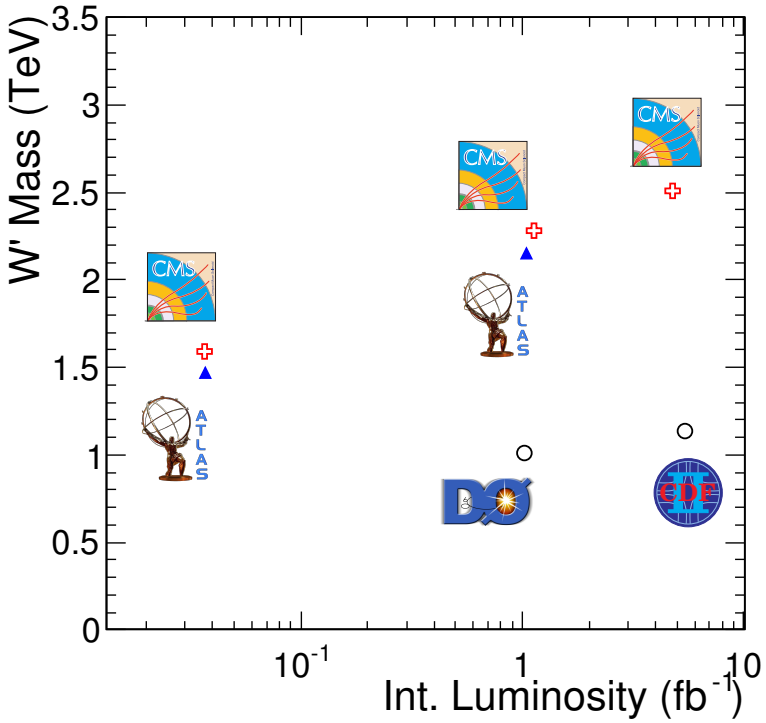

Figure 9.1.: Exclusion limit on the mass of a W′ with Standard-Model-like couplings as a function of the integrated luminosity for the LHC and Tevatron experiments.

A. Dataset Information

Generator	Process	Kinematic cuts (in GeV, $c = 1$)	σ_{LO} (pb)	σ_{NNLO} (pb)	# of events	PDF set
Background samples						
PYTHIA	W $\rightarrow\mu\nu$	$p_T < 100$ GeV	7900	10400	∼5M	CTEQ6L
PYTHIA	W $\rightarrow\mu\nu$	$p_T > 100$ GeV	1.19	1.57	∼1M	CTEQ6L
PYTHIA	W $\rightarrow\tau\nu$	no cuts	7900	10400	∼5M	CTEQ6L
PYTHIA	Z $\rightarrow\mu\mu$	$m_{\ell\ell} > 20$	1300	1670	∼1M	CTEQ6L
PYTHIA	Z $\rightarrow\mu\mu$	$m_{\ell\ell} > 200$	0.97	1.22	∼ 55K	CTEQ6L
PYTHIA	Z $\rightarrow\mu\mu$	$m_{\ell\ell} > 500$	0.027	0.034	∼55K	CTEQ6L
PYTHIA	Z $\rightarrow\mu\mu$	$m_{\ell\ell} > 800$	0.0031	0.0038	∼55K	CTEQ6L
PYTHIA	Z $\rightarrow\mu\mu$	$m_{\ell\ell} > 1000$	$9.74 \cdot 10^{-4}$	0.0012	∼55K	CTEQ6L
Madgraph	$t\bar{t}$	no cuts	94	158 (NLO)	∼4M	CTEQ6L
Powheg	$t \rightarrow bl\nu$ (s-Channel)	no cuts	-	3.19	∼0.3M	CTEQ6L
Powheg	$t \rightarrow bl\nu$ (t-Channel)	no cuts	-	41.9	∼4M	CTEQ6L
Powheg	$t \rightarrow bl\nu$ (tW-Channel DR)	no cuts	-	7.87	∼0.8M	CTEQ6L
Powheg	$\bar{t} \rightarrow bl\nu$ (s-Channel)	no cuts	-	1.44	∼0.1M	CTEQ6L
Powheg	$\bar{t} \rightarrow bl\nu$ (t-Channel)	no cuts	-	22.7	∼2M	CTEQ6L
Powheg	$\bar{t} \rightarrow bl\nu$ (tW-Channel DR)	no cuts	-	7.87	∼0.8M	CTEQ6L
PYTHIA	WW	no cuts	28.0	42.6 (NLO)	∼4M	CTEQ6L
PYTHIA	WZ	no cuts	10.4	18.2 (NLO)	∼4M	CTEQ6L
PYTHIA	ZZ	no cuts	4.3	5.9 (NLO)	∼4M	CTEQ6L
PYTHIA	Inclusive μ QCD	$\hat{p}_T > 20$ $p_T^{\mu} > 15$, $\lvert\eta_{\mu}\rvert < 2.5$	84700	-	∼30M	CTEQ6L

Table A.1.: Analysed Monte Carlo samples for the different background samples and their corresponding cross sections.

Sample	Dataset Name
W $\rightarrow\mu\nu_\mu$	/WToMuNu_TuneZ2_7TeV-pythia6/Summer11-PU_S3_START42_V11-v2/AODSIM
	/WToMuNu_ptmin-100_TuneZ2_7TeV-pythia6/Summer11-PU_S4_START42_V11-v1/AODSIM
W $\rightarrow\tau\nu_\tau$	/WToTauNu_TuneZ2_7TeV-pythia6-tauola/Summer11-PU_S3_START42_V11-v2/AODSIM
Z $\rightarrow\mu\mu$	/DYToMuMu_M-20_TuneZ2_7TeV-pythia6/Summer11-PU_S3_START42_V11-v2/AODSIM
Z $\rightarrow\tau\tau$	/DYToTauTau_M-20_TuneZ2_7TeV-pythia6-tauola/Summer11-PU_S3_START42_V11-v2/AODSIM
Z $\rightarrow\mu\mu, m_{\mu\mu} > 200$	/DYToMuMu_M-200_TuneZ2_7TeV-pythia6-tauola/Summer11-PU_S3_START42_V11-v2/AODSIM
Z $\rightarrow\mu\mu, m_{\mu\mu} > 500$	/DYToMuMu_M-500_TuneZ2_7TeV-pythia6-tauola/Summer11-PU_S3_START42_V11-v2/AODSIM
Z $\rightarrow\mu\mu, m_{\mu\mu} > 800$	/DYToMuMu_M-800_TuneZ2_7TeV-pythia6-tauola/Summer11-PU_S3_START42_V11-v2/AODSIM
Z $\rightarrow\mu\mu, m_{\mu\mu} > 1000$	/DYToMuMu_M-1000_TuneZ2_7TeV-pythia6-tauola/Summer11-PU_S3_START42_V11-v2/AODSIM
$t\bar{t}$	/TTJets_TuneZ2_7TeV-madgraph-tauola/Summer11-PU_S4_START42_V11-v1/AODSIM
$t \rightarrow bl\nu$ (s-Channel)	/T_TuneZ2_s-channel_7TeV-powheg-tauola/Summer11-PU_S4_START42_V11-v1/AODSIM
$t \rightarrow bl\nu$ (t-Channel)	/T_TuneZ2_t-channel_7TeV-powheg-tauola/Summer11-PU_S4_START42_V11-v1/AODSIM
$t \rightarrow bl\nu$ (tW-Channel DR)	/T_TuneZ2_tW-channel-DR_7TeV-powheg-tauola/Summer11-PU_S4_START42_V11-v1/AODSIM
$\bar{t} \rightarrow bl\nu$ (s-Channel)	/Tbar_TuneZ2_s-channel_7TeV-powheg-tauola/Summer11-PU_S4_START42_V11-v1/AODSIM
$\bar{t} \rightarrow bl\nu$ (t-Channel)	/Tbar_TuneZ2_t-channel_7TeV-powheg-tauola/Summer11-PU_S4_START42_V11-v1/AODSIM
$\bar{t} \rightarrow bl\nu$ (tW-Channel DR)	/Tbar_TuneZ2_tW-channel-DR_7TeV-powheg-tauola/Summer11-PU_S4_START42_V11-v1/AODSIM
WW	/WW_TuneZ2_7TeV_pythia6_tauola/Summer11-PU_S4_START42_V11-v1/AODSIM
WZ	/WZ_TuneZ2_7TeV_pythia6_tauola/Summer11-PU_S4_START42_V11-v1/AODSIM
ZZ	/ZZ_TuneZ2_7TeV_pythia6_tauola/Summer11-PU_S4_START42_V11-v1/AODSIM
Inclusive μ QCD	/QCD_Pt-20_MuEnrichedPt-15_TuneZ2_7TeV-pythia6/Summer11-PU_S4_START42_V11-v1/AODSIM

Table A.2.: Corresponding datasets of the used background Monte Carlo samples.

Generator	$m_{W'}$ (in GeV)	σ_{LO} (fb)	k-factor AN-11-273	σ_{NNLO} (fb)	# of events	PDF set
PYTHIA	500	13100	1.36	17700	10K	CTEQ6L1
PYTHIA	600	6330	1.35	8560	10K	CTEQ6L1
PYTHIA	700	3340	1.35	4510	10K	CTEQ6L1
PYTHIA	800	1870	1.35	2520	10K	CTEQ6L1
PYTHIA	900	1100	1.34	1470	10K	CTEQ6L1
PYTHIA	1000	665	1.33	886	16.5K	CTEQ6L1
PYTHIA	1200	264	1.31	346	16.5K	CTEQ6L1
PYTHIA	1300	171	1.30	222	16.5K	CTEQ6L1
PYTHIA	1400	113	1.28	144	16.5K	CTEQ6L1
PYTHIA	1500	75.0	1.27	94.9	16.5K	CTEQ6L1
PYTHIA	1600	50.6	1.26	63.3	16.5K	CTEQ6L1
PYTHIA	1700	34.3	1.23	42.4	16.5K	CTEQ6L1
PYTHIA	1800	23.5	1.21	28.5	16.5K	CTEQ6L1
PYTHIA	1900	16.3	1.19	19.4	16.5K	CTEQ6L1
PYTHIA	2000	11.4	1.18	13.5	16.5K	CTEQ6L1
PYTHIA	2100	8.00	1.17	9.37	16.5K	CTEQ6L1
PYTHIA	2200	5.69	1.16	6.61	16.5K	CTEQ6L1
PYTHIA	2300	4.08	1.16	4.72	16.5K	CTEQ6L1
PYTHIA	2400	2.96	1.15	3.40	16.5K	CTEQ6L1
PYTHIA	2500	2.18	1.14	2.48	16.5K	CTEQ6L1
PYTHIA	2700	1.22	1.17	1.43	12.4K	CTEQ6L1
PYTHIA	3000	0.579	1.22	0.707	16.5K	CTEQ6L1
PYTHIA	3500	0.210	1.34	0.280	16.5K	CTEQ6L1
PYTHIA	4000	0.106	1.38	0.146	16.5K	CTEQ6L1

Table A.3.: Signal Monte Carlo samples according to the benchmark model generated in Pythia. The k-factors are taken from the analysis note AN-11-273 [68].

B. Event Displays

In this section the event information of the four events with the highest transverse mass will be presented together with the corresponding event displays produced with the program FireWorks [106].
For the muons the p_T measurements with their uncertainties of the "Tracker-Track" and the "Global-Track" are given together with the results of the three TeV algorithms "Cocktail", "Tracker-Plus-First-Muon-Station" and "Picky". The uncertainty on the missing transverse energy is dominated by the uncertainty of the Cocktail p_T measurement, therefor also the uncertainty of the transverse mass is dominated by the p_T uncertainty.

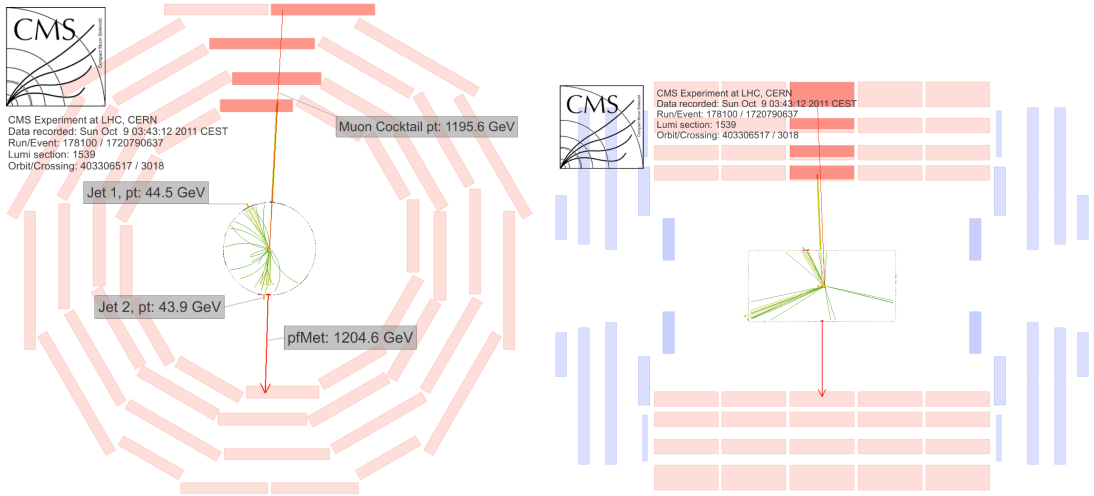

Figure B.1.: Event with the highest transverse mass of 2.4 TeV in the muon channel: ρ-ϕ view (left) and ρ-z view (right).

M_T	(2390 ± 130) GeV
Missing Energy	(1210 ± 60) GeV
Delta ϕ	3.12
Reconstructed Vertices	2

p_T Reconstructor	p_T [GeV]
Cocktail	1200 ± 60
Global Track	1210 ± 80
Tracker Track	980 ± 140
TPFMS	1200 ± 60
Picky	1210 ± 80

Table B.1.: Event information for the event with 2.4 TeV transverse mass. Run: 178100 Lumi Section: 1539 Event: 1720790637.

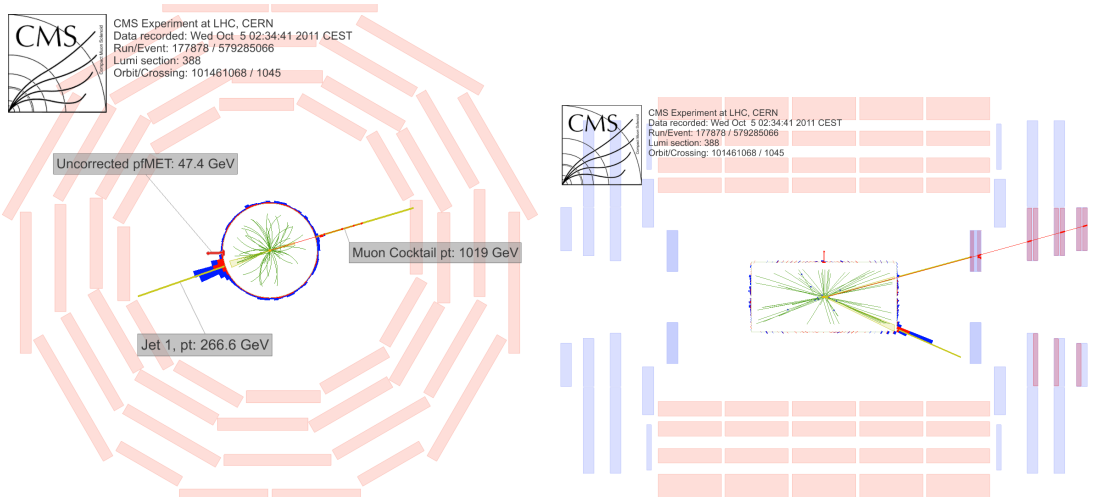

Figure B.2.: Event with the second highest transverse mass of 1.8 TeV in the muon channel: ρ-ϕ view (left) and ρ-z view (right).

M_T	(1780 ± 600) GeV
Missing Energy	(780 ± 300) GeV
Delta ϕ	3.12
Reconstructed Vertices	11
p_T Reconstructor	p_T [GeV]
Cocktail	1020 ± 300
Global Track	290 ± 40
Tracker Track	260 ± 30
TPFMS	1020 ± 300
Picky	280 ± 40

Table B.2.: Event information for the event with 1.8 TeV transverse mass. Run: 177878 Lumi Section: 388 Event: 579285066.

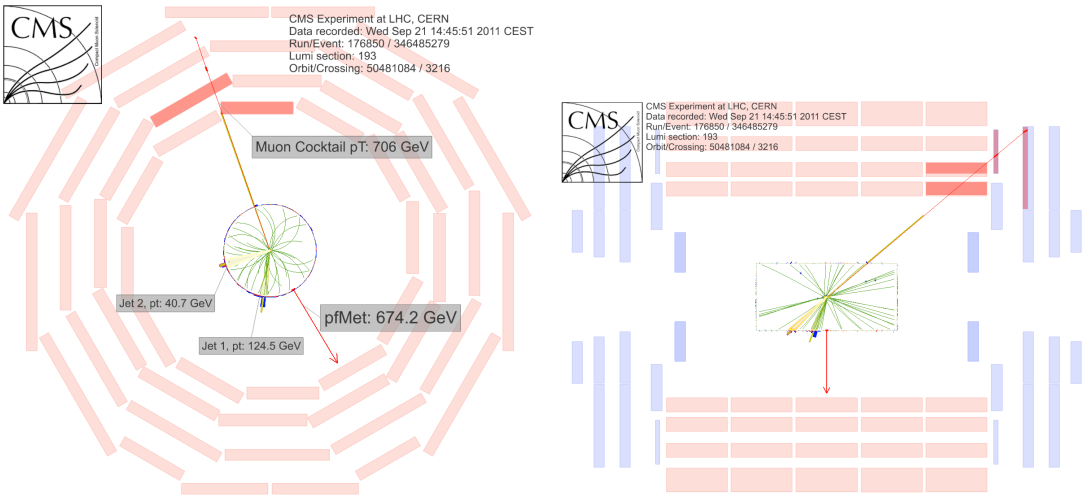

Figure B.3.: Event with the third highest transverse mass of 1.3 TeV in the muon channel: ρ-ϕ view (left) and ρ-z view (right).

M_T	(1300 ± 80) GeV
Missing Energy	(670 ± 40) GeV
Delta ϕ	2.91
Reconstructed Vertices	10
p_T Reconstructor	p_T [GeV]
Cocktail	710 ± 40
Global Track	780 ± 20
Tracker Track	690 ± 90
TPFMS	710 ± 40
Picky	780 ± 40

Table B.3.: Event information for the event with 1.3 TeV transverse mass. Run: 176850 Lumi Section: 193 Event: 346485279.

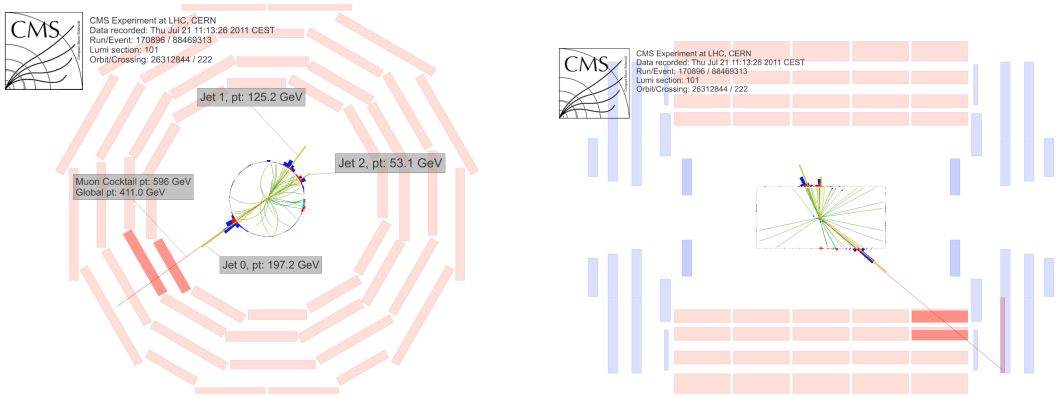

Figure B.4.: Event with the fourth highest transverse mass of 1.2 TeV in the muon channel: ρ-ϕ view (left) and ρ-z view (right).

M_T	(1170 ± 360) GeV
Missing Energy	(570 ± 180) GeV
Delta ϕ	3.13
Reconstructed Vertices	2
p_T Reconstructor	p_T [GeV]
Cocktail	600 ± 180
Global Track	410 ± 40
Tracker Track	600 ± 180
TPFMS	380 ± 20
Picky	410 ± 30

Table B.4.: Event information for the event with 1.2 TeV transverse mass. Run: 170896 Lumi Section: 101 Event: 88469313.

Bibliography

[1] S. L. Glashow, J. Iliopoulos und L. Maiani, *Weak Interactions with Lepton-Hadron Symmetry*, Physical Review D2 1285-1292, 1970.

[2] S. Weinberg, A Model of Leptons, Phys. Rev. Lett. 19 1264–1266, 1967.

[3] A. Salam, J. C. Ward, *Gauge theory of elementary interactions*, Phys. Rev. 136 B, 763-768, 1964.

[4] D. J. Gross, F. Wilczek, *Asymptotically Free Gauge Theories I*, Phys. Rev. D 8, 3633-3652, 1973.

[5] Wikipedia, The Free Encyclopedia, The Standard Model of Elementary Particles, 01/2012, http://en.wikipedia.org/wiki/File:Standard_Model_of_Elementary_Particles.svg.

[6] M. Beneke, *Lecture Notes Quantum Field Theory I*, 2009/2010.

[7] L. Reina, *The Standard Model of Particle Physics*, Herbstschule Maria-Laach, 2011.

[8] L. Feld, *Lecture Notes Elementarteilchen I*, 2009/2010.

[9] G.'t Hooft, M. J. G. Veltman, *Regularization and renormalization of gauge fields*, Nucl. Phys. B44, No. 1, 189-213, 1972.

[10] High Energy Group Imperial College, Website, 2011, http://www.hep.ph.ic.ac.uk/cms/physics/higgs.html.

[11] Particle Data Group, *Review of particle physics*, 2010.

[12] R. N. Mohapatra, J. C. Pati, *Left-right gauge symmetry and an isoconjugate model of CP violation*, Phys. Rev. D 11, 566, 1975.

[13] R. N. Mohapatra, G. Senjanovic, *Neutrino mass and Spontaneous Parity Nonconservations*, Phys. Rev. Lett. 44, 912, 1980.

[14] M. Lindner, T. Ohlson, G. Seidl, *See-saw Mechanism for Dirac and Majorana Neutrino Masses*, Phys. Rev. D 65, 053014, 2002.

[15] M. Kirsanov et al., *Search for a heavy neutrino and right-handed W of the left-right symmetric model in the muon channel using pp collisions at* $\sqrt{s} = 7$ *TeV*, CMS Analysis Note AN-11-425, 2012.

[16] T. Han, H. E. Logan, B. McElrath, L.-T. Wang, *Phenomenology of the Little Higgs Model*, Phys. Rev. D67 095004, 2003.

[17] S. J. Huber, C.-A. Lee , Q. Shafi, *Kaluza-Klein excitations of W and Z at the LHC?*, Phys. Lett. B531, Number 1, pp. 112-118, 2002.

[18] G. Altarelli, B. Mele, M. Ruiz-Altaba, *Searching for New Heavy Vector Bosons in* $p\bar{p}$ *Colliders*, Z. Phys. C45, 109, 1989.

[19] The CMS Collaboration, *Search for* W′ *(or techni-rho) to WZ*, CMS PAS EXO-11-041, 2011.

[20] The CMS Collaboration, *Search for exotic VZ resonances in the hadronic and leptonic channels with CMS*, CMS PAS EXO-11-081, 2011.

[21] T. Sjöstrand, S. Mrenna, P. Skands, *PYTHIA 6.4 Physics and Manual*, JHEP, 605:26, 2006, arXiv:hep-ph/0603175v2.

[22] Private Communication with Can Kilic and Scott Thomas, 2011.

[23] D. Kim, Y. Oh, S. C. Park, W′ *in new physics models at the LHC*, arXiv:1109.1870.

[24] D. Kim et al., *UED driven* W′ *decay*, CMS Analysis Note AN-11-471, 2011.

[25] E. Accomando et al., *Interference effects in heavy* W′ *-boson searches at the LHC*, arXiv:1110.0713v1.

[26] T. G. Rizzo, *The Determination of the Helicity of* W′ *Boson Couplings at the LHC*, JHEP 0705, 037, 2007, arXiv:0704.0235v4.

[27] The DØ Collaboration, *Search for* W′ *Bosons Decaying to an Electron and a Neutrino with the D0 Detector*, Phys. Rev. Lett. 100, 031804, 2008.

[28] The CDF Collaboration, *Search for a New Heavy Gauge Boson* W′ *with Electron+*$\not\!\!E_T$ *Event Signature in* $p\bar{p}$ *collisions at* $\sqrt{s}$ *= 1.96 TeV*, Phys. Rev. D 83, 031102, 2011, arXiv:1012.5145.

[29] Y. Zhang et al., Phys. Rev. D76, 091301, 2007.

[30] L. Evans, P. Bryant (editors), *LHC Machine*, JINST, 3 S08001, 2008.

[31] CERN Website, 2011,
http://public.web.cern.ch/public/en/Research/AccelComplex-en.html.

[32] The CMS Collaboration, *The CMS experiment at the CERN LHC*, JINST, 3 S08004.

[33] ATLAS Collaboration, *The ATLAS Experiment at the CERN Large Hadron Collider*, JINST, 3 S08003, 2008.

[34] The ALICE Collaboration, *The ALICE Experiment at the CERN Large Hadron Collider*, JINST, 3 S08002, 2008.

[35] LHCb Collaboration, *The LHCb Detector at the LHC*, JINST, 3 S08005, 2008.

[36] The CMS Collaboration, *The CMS Tracker System Project, Technical Design Report*, CERN-LHCC-98-006, 1998

[37] The CMS Collaboration, *The Electromagnetic Calorimeter Project, Technical Design Report*, CERN-LHCC-97-033, 1997.

[38] The CMS Collaboration, *CMS Physics: Technical Design Report, Vol. I*, CERN/LHCC 2006-001., 2006.

[39] The CMS Collaboration, *The Hadron Calorimeter Project, Technical Design Report*, CERN-LHCC-97-031, 1997.

[40] The CMS Collaboration, *The CMS Muon Project, Technical Design Report*, CERN-LHCC-97-032, 1997.

[41] The CMS Collaboration, *Performance of muon reconstruction and identification in pp collisions at* $\sqrt{s} = 7$ *TeV*, CMS PAS MUO-10-004, 2010.

[42] The CMS Collaboration, *The TriDAS Project, Technical Design Report, Volume 1: The Trigger Systems*, CERN/LHCC 2000-38, 2000.

[43] The CMS Collaboration, *The TriDAS project, Technical Design Report, Volume 2: Data Acquisition and High-Level Trigger*, Technical Design Report, CERN-LHCC-2002-026, 2002.

[44] R. Fruhwirth, *Application of Kalman filtering to track and vertex fitting*, Nucl. Instrum. Meth. A262, 1987.

[45] Worldwide LHC Computing Grid, Website, 2011, http://lcg.web.cern.ch/lcg.

[46] S. Van der Meer, *Calibration of the effective beam height in the ISR*,CERN-ISR-PO/68-31, 1968.

[47] The CMS Collaboration, *Measurement of CMS luminosity*, CMS PAS EWK-2010-004, 2010.

[48] The CMS Collaboration, *Absolute Calibration of the Luminosity Measurement at CMS:Winter 2012 Update*, CMS PAS SMP-12-008, 2012.

[49] The CMS Collaboration, *Absolute Callibration of Luminosity Measurements at CMS: Summer 2011 Update*, CMS PAS EWK-11-001.

[50] G. Abbiendi et al., *Muon Reconstruction in the CMS Detector*, CMS Analyis Note AN-08-097, 2009.

[51] The CMS Collaboration, *Particle-Flow Event Reconstruction in CMS and Performance for Jets, Taus, and Missing* E_T, CMS PAS PFT-09-001, 2009.

[52] The CMS Collaboration, Twiki Website, 2011, https://twiki.cern.ch/twiki/bin/view/CMSPublic/WorkBookCMSSWFramework.

[53] C. Magass et al., Aachen 3A Susy Analysis, Twiki Website, 2011, https://twiki.cern.ch/twiki/bin/viewauth/CMS/Aachen3ASusy.

[54] The ROOT Team, *The ROOT User's Guide*, v5.26 edition, http://root.cern.ch/drupal/content/users-guide, 2007.

[55] L. Moneta et al., *The RooStats Project*, ACAT2010 Conference Proceedings, arXiv:1009.1003v1.

[56] A. Caldwell, D. Kollar, K. Kröninger, *BAT - The Bayesian Analysis Toolkit*, Computer Physics Communications (2009) 2197–2209. online version: arXiv:0808.2552v1.

[57] The CMS Collaboration, Twiki Website, 2011, https://twiki.cern.ch/twiki/bin/view/CMS/DataCertificationatDQMGroup.

[58] The CMS Collaboration, Twiki Website, 2011, https://twiki.cern.ch/twiki/bin/view/CMSPublic/LumiPublicResults.

[59] GEANT4 Collaboration, *GEANT4: A simulation toolkit*, Nucl. Instrum. Meth. A506 (2003) 250–303, doi:10.1016/S0168-9002(03)01368-8.

[60] The CMS Collaboration, Twiki Website, 2011, https://twiki.cern.ch/twiki/bin/view/CMS/ProductionSummer2011.

[61] J. Alwall et al., *MadGraph/MadEvent v4: the new web generation*, JHEP 09 (2007) 610 028. doi:10.1088/1126-6708/2007/09/028.

[62] S. Frixione, P. Nason, C. Oleari, *Matching NLO QCD computations with Parton Shower simulations: the POWHEG method*, JHEP 11 070, 2007.

[63] A. D. Martin et al., *Parton distributions for the LHC*, Eur.Phys.J.C63:189-285, 2009.

[64] J. Pumplin et al., *New Generation of Parton Distributions with Uncertainties from Global QCD Analysis*, JHEP07(2002)012 doi:10.1088/1126-6708/2002/07/012.

[65] The CMS Collaborations, Twiki Website, https://twiki.cern.ch/twiki/bin/viewauth/CMS/StandardModelCrossSections.

[66] The CMS Collaboration, Twiki Website, https://twiki.cern.ch/twiki/bin/view/CMS/SingleTopSigma.

[67] R. Gavin, Y. Li, F. Petriello, S. Quackenbush, *FEWZ 2.0: A code for hadronic Z production at next-to-next-to-leading order*, 2010, arXiv:1011.3540v1.

[68] K. Hoepfner, D. Kim, Y. Oh, Y. Yang, *PDF Uncertainties and K-factor for the* W′ *search*, CMS Analysis Note AN-11-273, 2011.

[69] The PDF4LHC working group, Website, 2011, http://www.hep.ucl.ac.uk/pdf4lhc/.

[70] The Les Houches Accord PDF Interface, Website, 2011, http://projects.hepforge.org/lhapdf/.

[71] Exotica Muon Recommendations, Twiki Website, 2011, https://twiki.cern.ch/twiki/bin/viewauth/CMS/ExoticaMuons.

[72] Muon POG Definition of muon ID, Twiki Website, 2011, https://twiki.cern.ch/twiki/bin/view/CMS/MuonRecoPerformance2010.

[73] C. Jarvis, Talk, *Optimization of quality cuts for high-pT muons*, http://indico.cern.ch/conferenceDisplay.py?confId=128976

[74] D. Acosta et al., *Search for High-Mass Resonances Decaying to Muon Pairs with Collisions Gathered at* $\sqrt{s}$ *= 7 TeV*, CMS Analysis Note AN-11-278, 2011.

[75] C. Magass, *Search for new heavy Charged Gauge Bosons*, Doctoral thesis, 11/2007.

[76] C. Hof, *Detection of New Heavy Charged Gauge Bosons with the Future CMS Detector*, Diploma thesis, 12/2005.

[77] W. Bender, *Studie zum Nachweis schwerer, geladener Eichbosonen in leptonischen Zerfallskanälen mit dem CMS-Detektor*, Diploma thesis, 10/2008.

[78] The CMS Collaboration, Twiki Website, https://twiki.cern.ch/twiki/bin/viewauth/CMS/PileupMCReweightingUtilities.

[79] A. Güth, *Analysis of W and Z Production at sqrt s = 7 TeV with the CMS Detector*, Diploma thesis, 05/2011.

[80] Private Communication with Andreas Güth, 2011.

[81] The CMS Collaboration, *Search for a heavy gauge boson* W′ *in the final state with an electron and large missing transverse energy in pp collisions at* $\sqrt{s}$ *= 7 TeV*, Phys. Lett. B 698 (2011) 21–39, arxiv:1012.5945.

[82] The CMS Collaboration, *Search for a* W′ *boson decaying to a muon and a neutrino in pp collisions at* $\sqrt{s}$ *= 7 TeV*, Phys. Lett. B701 (2011) 160–179, arXiv:1103.0030.

[83] The CMS Collaboration, *Search for* W′ *in the muon and electron channels in pp Collisions at sqrt(s) = 7 TeV*, CMS PAS EXO-11-024, 2011.

[84] N. Adam et al., *Generic Tag and Probe Tool for Measuring Efficiency at CMS with Early Data*, CMS Analysis Note AN-2009-111, 2009.

[85] J. Alcarez et al., *Updated Measurements of the Inclusive W and Z Cross Sections at 7 TeV*, CMS Analysis Note AN-2010-264, 2010.

[86] Private Communication with Jan-Frederik Schulte, 2011/2012.

[87] P. Traczyk, Talk, *Muon Object Review*, 2011, https://indico.cern.ch/conferenceDisplay.py?confId=172430.

[88] The CMS Collaboration, MET group, *Prescriptions for MET uncertainties*, Twiki Website, 2011, https://twiki.cern.ch/twiki/bin/viewauth/CMS/MissingETUncertaintyPrescription.

[89] The CMS Collaboration, Twiki Website, 2011, https://twiki.cern.ch/twiki/bin/view/CMS/LumiCalc.

[90] The CMS Collaboration, *Measurement of the inelastic pp cross section at* $\sqrt{s}$ *= 7 TeVwith the CMS detector*, CMS PAS FWD-11-001.

[91] The CMS Collaboration, Twiki Website, 2011, https://twiki.cern.ch/twiki/bin/viewauth/CMS/PileupSystematicErrors.

[92] The CMS Collaboration, *Search for Microscopic Black Hole Signatures at the Large Hadron Collider*, EXO-11-021, 2011.

[93] The CMS Collaboration, Twiki Website, 2011, https://twiki.cern.ch/twiki/bin/viewauth/CMS/StatisticsTools.

[94] B. Berg, *Markov Chain Monte Carlo Simulations and Their Statistical Analysis*, World Scientific, 2004.

[95] S. A. Schmitz et al., *Limit Combination of Searches for Large Extra Dimensions in Dielectron, Dimuon and Diphoton Events in pp Collisions at $\sqrt{s}$ = 7 TeV at Updated Integrated Luminosity*, CMS Analysis Note AN-11-420, 2011.

[96] T. Junk, *Confidence level computation for combining searches with small statistics*, Nucl. Instrum. Meth. A 434, 435, 1999.

[97] ATLAS Collaboration, *Search for a heavy gauge boson decaying to a charged lepton and a neutrino in 1 fb^{-1} of pp collisions at $\sqrt{s}$ = 7 TeV using the ATLAS detector*, Phys. Lett. B705 28–46, 2011, arXiv:1108.1316.

[98] T. Bose et al., *Search for W' in the muon and electron channels in pp Collisions at $\sqrt{s}$ = 7 TeV*, CMS Analysis Note AN-11-227, 2011.

[99] J.-F. Schulte, Master thesis in preparation, 2011/2012.

[100] T. Bose et al., *Search for W' in the muon channel in pp Collisions at $\sqrt{s}$ = 7 TeV*, CMS Analysis Note AN-10-315, 2010.

[101] The CMS Collaboration, Twiki Website, 2011, https://twiki.cern.ch/twiki/bin/view/CMSPublic/SWGuideLHEInterface.

[102] E. Boos et al., *CompHEP 4.4 -Automatic Computations from Lagrangians to Events*, 2004, arXiv:hep-ph/0403113.

[103] The CMS Collaboration, *Search for* $\mathrm{W}' \rightarrow \mathrm{t}\bar{\mathrm{b}}$, CMS PAS EXO-11-046, 2011.

[104] ATLAS Collaboration, *Search for high-mass states with one lepton plus missing transverse momentum in proton-proton collisions at $\sqrt{s}$ = 7 TeV with the ATLAS detector*, Phys. Lett. B701 50-69, 2011, arxiv:1103.1391.

[105] S. Erdweg, *Study for Sensitivity for W' to tau nu with CMS*, Bachelor thesis, 07/2011.

[106] The CMS Collaboration, Twiki Website, 2011, https://twiki.cern.ch/twiki/bin/view/CMS/WorkBookFireworks.

List of Figures

List of Tables

Danksagung

Nun ist ein wenig mehr als ein Jahr vergangen und die Arbeit ist zu einem Ende gekommen, daher möchte ich mich abschließend noch bei den Personen bedanken, die mich dabei unterstützt haben.
Zuallererst möchte ich meinen Eltern danken, die diese Arbeit sicherlich erst möglich gemacht haben und die mich während meiner gesamten Studienzeit finanziell, ganz besonders aber auch moralisch unterstützt haben.
Außerdem danke ich Prof. Dr. Hebbeker für die Möglichkeit an diesem interessanten Thema zu arbeiten und meine Arbeit im III. Physikalischen Institut anzufertigen. Vielen Dank auch an Prof. Dr. Wiebusch, der sich bereit erklärt hat, sich als Zweitgutachter zur Verfügung zu stellen.
Ich danke auch der gesamten Aachener CMS Gruppe für die Hilfestellungen bei verschiedensten Problemen und die vielen anregenden Diskussionen. Besonders möchte ich mich bei Tobias Pook, Jan-Frederik Schulte, Fabian Schneider und Klaas Padeken bedanken, die immer für eine gute Stimmung und Arbeitsatmosphäre im Büro gesorgt haben. Weiterhin danke ich Carsten Magass für das Bereitstellen seines Skimmers und seiner anderen hilfreichen Programme und Stefan Schmitz für seine Hilfestellungen im Bereich der statistischen Analyse.
Abschließend möchte ich mich im Besonderen noch bei Kerstin Hoepfner für die sehr intensive Betreuung und das Korrekturlesen dieser Arbeit bedanken.

Selbständigkeitserklärung

Mit der Abgabe der Masterarbeit versichere ich hiermit schriftlich, dass ich die Arbeit selbständig verfasst und keine anderen als die angegebenen Quellen und Hilfsmittel benutzt sowie Zitate kenntlich gemacht habe.

Sebastian Thüer

Aachen, den 12. April 2012